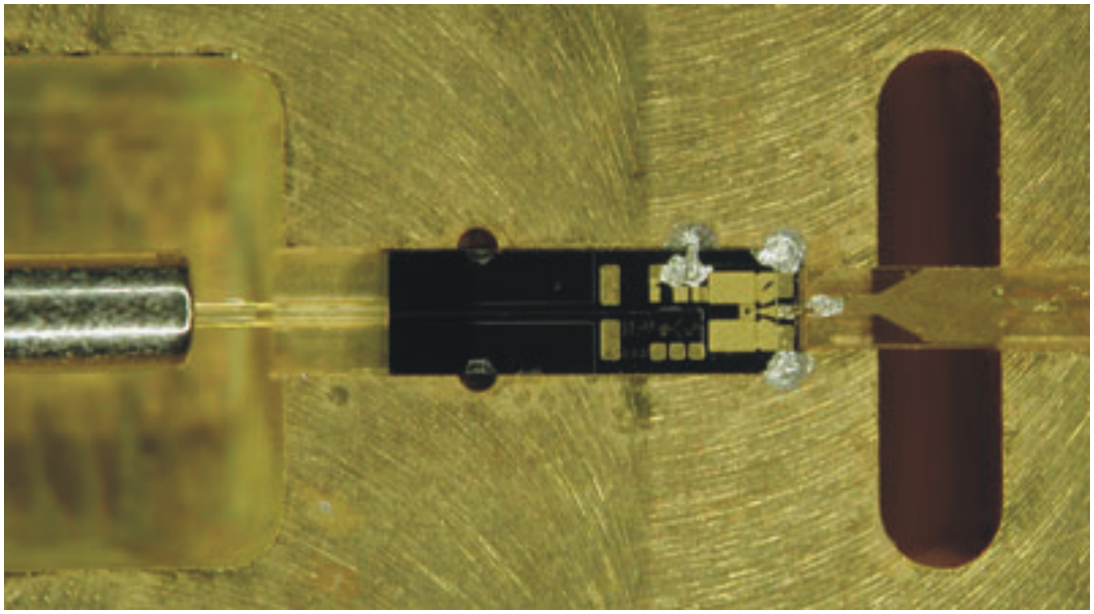

This thesis was typeset with LaTeX, using a modified version of the University of California Ph.D. dissertation class file, `ucthesis.cls`. Unless otherwise noted, all figures in this thesis were created by the author using IDL® or CorelDraw®.

Cover photograph A photodiode in WR-10 waveguide mount. The optical fiber and its ferrule are visible on the left of the picture (*Photo: MMT Group, STFC, Rutherford Appleton Laboratory*).

Performance Characterization of a Millimeter-Wave Photomixer

Gibion Makiwa

B.Sc. Hons in Physics, University of Zimbabwe, 1999
M.Sc. Applied Physics, University of Zimbabwe, 2006

A Thesis
Submitted to the School of Graduate Studies
of the University of Lethbridge
in Partial Fulfilment of the
Requirements of the Degree

Master of Science

Department of Physics & Astronomy
University of Lethbridge
Lethbridge, Alberta, Canada

Dedication

This thesis is dedicated to my late parents.

Abstract

Our group purchased a THz photomixer from the Millimeter Wave Technology Group at the Rutherford Appleton Laboratory in London, UK. A photomixer is based on optical heterodyne conversion where a photoconductor or photodiode is illuminated by two laser beams with a difference frequency in the THz region. The beat frequency of the two lasers will modulate the conductivity of the photomixer material. The variation of the conductivity is converted to electrical current and finally radiation by applying a bias voltage across the active region of the device. My thesis concerns the determination of the characteristics of the photomixer, which is an expensive and extremely sensitive piece of equipment, to optimize its performance in support of a number of research activities within the group.

Acknowledgements

I would like to thank my supervisor Dr David Naylor for affording me an opportunity to study at the Univeristy of Lethbridge. I have been blessed to have a supervisor who cares about my work and whose critical constructive criticism of my work has made me a better physicist. I would also like to thank David for getting me involved in a second project, the SPIRE project. My contribution in this second project has resulted in my name appearing as a co-author in more than a dozen research articles.

I would like to thank Brad Gom for helping me use the University of Lethbridge Fourier Transform Spectrometer (FTS). Brad has also been very helpful in many other ways.

The THz power from the photomixer was measured using a cooled detector operating at 300 mK. Cycling the ^{3}He is not an easy task. I would like to thank David Naylor, Brad Gom, Locke Spencer and Scott Jones for helping with this important part of the project.

When I joined the Astronomical Instrumentation Group at the University of Lethbridge, my knowledge of programming was limited to Matlab. I am grateful to Locke Spencer and Richard Querel for introducing me to IDL and for pointing me to where I could get information about this programming language.

I would like to thank Gregory Thompkins for designing and building a bias supply box for the photomixer. The bias box helped protect the photomixer from being damaged.

I would also like to thank my supervisory committee members, Dr David Naylor, Dr Adriana Predoi Cross and Dr Rene Boere for sparing time to have a meeting with me at the end of every semester for the past two years. I thank you all for the constructive suggestions and encouragement.

I would like to thank the rest of the AIG group members and the Department of Physics staff and fellow students for the support and encouragement. When I joined the Department of Physics at the University of Lethbridge, I felt welcomed, and will always cherish the nice working environment.

Lastly, I would like to thanks the administration staff for helping me in various ways during the last two years. I say thank you to Sheila Matson for being cheerful and for the encouragement. Thank you to Laurie Scott for the good job you are doing.

Contents

List of Tables

List of Figures

List of Abbreviations

AIG	Astronomical Instrumentation Group.
ALMA	Atacama Large Millimeter/submillimeter Array.
BWO	backward wave oscillator.
CPS	coplanar strip.
CW	continuous-wave.
DAQ	Data Aquisition.
DBR	Distributed Bragg Reflector.
DC	direct current.
EDFA	erbium doped fiber amplifier.
ErAs:GaAs	erbium arsenide: gallium arsenide.
ErAs:InGaAs	erbium arsenide: indium gallium arsenide.
ESD	electrostatic discharge.
FEL	free electron laser.
FIR	far-infrared.
FTS	Fourier transform spectrometer.
GPIB	General Purpose Interface Bus.
GUI	Graphical User Interface.
HEB	hot electron bolometer.
HEMT	high electron mobility transistor.
IF	intermediate frequency.
IMPACT	impact avalanche transit time.
InGaAs	indium gallium arsenide.
InP	indium phosphide.
IR	infrared.
ISM	interstellar medium.

LD	laser diode.
LDC	laser diode controller.
LO	local oscillator.
LTG-GaAs	low-temperature-grown gallium arsenide.
MBE	molecular beam epitaxy.
MLD	multimode laser diode.
MMIC	monolithic millimeter-wave integrated circuit.
MMT	Millimeter Wave Technology.
MSM	metal-semiconductor-metal.
NEP	noise equivalent power.
NI	National Instruments.
OPD	optical path distance.
OSA	optical spectrum analyzer.
PA	power amplifier.
PD	photodiode.
PMF	polarization maintaining fibre.
QCL	quantum cascade laser.
RAL	Rutherford Appleton Laboratory.
RF	radio frequency.
RTD	resonant tunneling diode.
SIS	semiconductor-insulator-semiconductor.
SSMA	Sub-SMA. A small version of the SMA connector, about 70 % size.
STFC	Science and Technology Facilities Council.
TED	tunneling electron device.
THz	terahertz.
TUNNETT	tunnel injection transit time.
UTC-PD	uni-traveling-carrier p-i-n photodiode.

List of Equations

Chapter 1

Introduction

The Terahertz (THz) region of the electromagnetic spectrum, sometimes called the THz gap, is one of the least exploited mostly because of the unavailability of sources operating in this region. Attempts to close the THz gap have resulted in a number of sources. In this Chapter, various narrow band THz sources are described together with their limitations. There are basically seven categories of narrow-band THz sources: electron beam sources, optically pumped far-infrared gas lasers, solid state sources, frequency multipliers, THz semiconductor lasers, THz parametric sources and THz photomixers [1]. Various challenges associated with the first five sources which limit their applications will be discussed. The last two sources employ optoelectronic techniques and are currently drawing a lot of interest because of their unique capabilities in the generation of THz signals. Sources based on optoelectronic techniques promise to overcome limitations suffered by other sources by providing broadband coverage and CW tunability.

1.1 Background

Despite its great interest to science since the 1920s [2], the terahertz (THz) frequency range has remained one of the least tapped regions of the electromagnetic spectrum [3]. The term THz was earlier applied to frequencies that fell below the far-infrared (FIR). Today, it is applied to submillimeter-wave radiation that fills the wavelength range between 1000 to 100 μm (300 GHz to 3 THz) [4–7]. This region of the electromagnetic spectrum is shown in Figure 1.1. Radiation at 1 THz has a period of 1 ps, a wavelength of 300 μm, a wave number of 33 cm^{-1}, a photon energy of 4.1 meV, and an equivalent temperature of 47.6 K. Tunable monochromatic sources operating in regions below 300 GHz and above 3

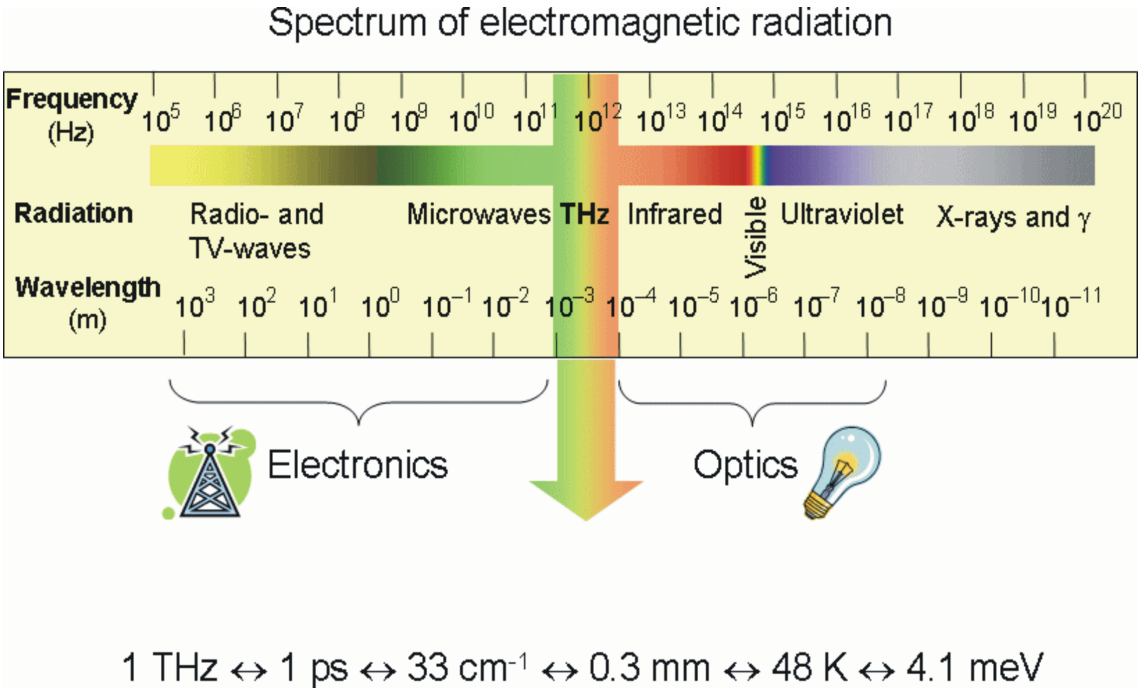

Figure 1.1: The location of the THz region on the electromagnetic spectrum. Radiation in the radio and microwave regions can be produced using electronic circuits while long-wavelength infrared radiation and beyond is produced through quantum transitions in photonic devices. Figure courtesy of [8].

THz are commercially available. In this work we will focus on the region between 300 GHz and 3 THz where there are few commercially available components. One of the principal reasons why there has been little work done in this region is the lack of powerful sources and sensitive detectors. THz technology has had great impact in high resolution laboratory spectroscopy and remote sensing where heterodyne and Fourier transform techniques have allowed chemists, astrophysicists, planetary, and space scientists to measure, catalog, and map emission lines for a variety of small and large molecules [9]. Molecular spectroscopy for planetary and space science has been one of the chief drivers for THz technology.

1.2 Continuous - Wave THz Sources and their limitations

Monochromatic THz sources can be divided into seven categories: electron beam sources; optically pumped far-infrared gas lasers; solid state sources; frequency multipliers; THz semiconductor lasers; THz parametric sources and THz photomixers. The goal of this section is to provide an overview of these sources, their current state-of-the-art performance and limitations. Figure 1.2 shows a comparison of some THz sources in terms of their output power and operation frequency. A brief description of some of the sources shown in the figure is presented in Sections that follow.

1.2.1 Electron Beam Sources

The use of the electron beam to generate THz radiation has existed for some time. Examples of electron beam sources that generate relatively high power continuous-wave (CW) THz radiation are the gyrotron [11], free electron laser (FEL) and the backward wave

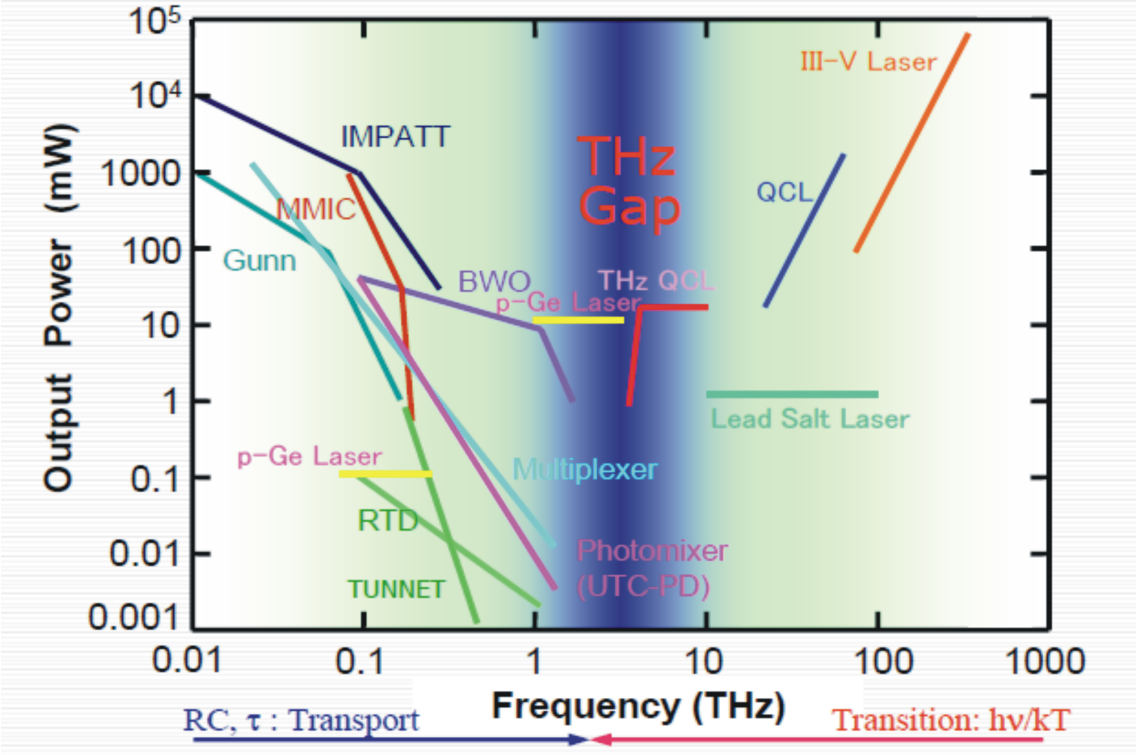

Figure 1.2: Comparison of some THz sources in terms of their output power and operation frequency. IMPATT: impact avalanche transit time; MMIC: monolithic millimeter-wave integrated circuit; BWO: backward wave oscillator; RTD: resonant tunneling diode; TUNNET: tunnel injection transit time; QCL: quantum cascade laser. Figure courtesy of Terrahertz Technology Trend Investigation Committee, MIC, Japan [10].

oscillator (BWO). These devices are based on the interaction of a high energy electron beam with a strong magnetic field inside a resonant cavity or waveguide. This interaction results in energy transfer from the electron beam to an electromagnetic wave [1]. Dammertz *et al.*. [12] have developed a 1 MW gyrotron that operates in CW mode at around 140 GHz. Powers greater than 2 MW have been achieved for short pulse operation but what makes this gyrotron special is its capability of continuous wave operation.

A FEL uses a relativistic beam of electrons passing through an undulating magnetic field to produce stimulated emission of electromagnetic radiation [13]. The periodically alternating magnetic field forces a sinusoidal oscillation of the electrons which generates coherent monochromatic radiation. An example is the 2.4 KW FIR-FEL developed at the University of California, Santa Barbara which operates from 0.89 to 4.76 THz [14].

BWO are vacuum tubes in which accelerated electrons interact with a traveling electromagnetic wave. The electrons are slowed down by a metal grating called a comb slow-wave structure which causes bunching of electrons [15]. The bunched distribution of electrons excites surface electromagnetic waves on the periodic structure. If the electron beam velocity matches the phase velocity of the surface wave, which is in the opposite direction, the kinetic energy of the electrons is transferred coherently to the electromagnetic wave. Currently, the output power of BWOs decreases from slightly above 50 mW at 300 GHz to a few mW at 1 THz [1].

Limiting factors in the THz application of electron beam sources are that they are large and heavy and require large bias voltages. The large magnets used also require water cooling systems.

1.2.2 Optically Pumped Far-IR Gas Lasers

An optically-pumped FIR gas laser [16,17] consists of a grating-tuned carbon dioxide pump laser which is used to pump a second laser whose gain medium is a molecular gas such as CH_3F, CH_3OH, NH_3 or CH_2F_2. The lasing frequency is determined by the filling gas. At room temperature, the molecules occupy the lowest vibrational mode ($\upsilon = 0$) with a thermal population:

$$N(J,K) \propto g(J,K)e^{-E_{rot}(J,K)/k_BT} \tag{1.1}$$

of rotational states, where E_{rot} are the rotational energy eigenvalues, J and K are the first and second rotational quantum numbers, g is the level degeneracy, k_B is the Boltzmann constant and T is the molecular gas temperature. Optical pumping excites some of the molecules from the lowest to the first excited vibrational mode. This induces a population inversion between J+1 and J levels for ($\upsilon = 0$) and between J and J-1 levels for ($\upsilon = 1$) giving rise to emissions at THz frequencies. More than 2000 far infrared laser lines have been obtained from various molecules [18,19]. A maximum THz power of 20 mW has been obtained for 100 W of laser pump power [1]. Optically pumped FIR gas lasers tend to be bulky and unstable.

1.2.3 Solid State Sources

Solid State devices for THz applications exhibit a negative differential resistance property for oscillation and amplification [1]. Negative differential resistance is a property exhibited by some semiconductor materials where the Voltage-current (VI) curve is negative for a particular voltage region. Examples of two-terminal solid state devices used in

the generation of THz radiation are the Gunn or tunneling electron devices (TEDs), resonant tunneling diodes (RTDs) and transit time devices such as impact avalanche transit time (IMPACT) diodes and tunnel injection transit time (TUNNETT) diodes. These are favorable over two junction devices because they generate more power.

Orihashi *et al.* [20] have reported on a sub-THz oscillating GaInAs/AlAs RTD having a maximum output power of 23 μW at its fundamental frequency of 342 GHz using a slot antenna which is described in Chapter 3. The power for the third harmonic of the same device at 1.02 THz was 2.6 % of the fundamental. This was an improvement from the device reported by Brown *et al.*. [21], which produced 0.3 μW at 712 GHz. InP Gunn devices yielding output power levels of 45 μW at 409 GHz have been reported [22]. The same authors also reported on a TUNNETT diode yielding more than 140 μW of output power at 355 GHz in the third harmonic mode [23].

Two junction solid state devices like field effect transistors have the advantage of low noise and wideband amplifier applications, but do not generate more power. Heat dissipation is a problem in these devices. A power amplifier (PA) module containing an InP high electron mobility transistor (HEMT), monolithic millimeter-wave integrated circuit (MMIC) has been reported to produce 20 mW of output power at 150 GHz [24]. Generally solid state sources are devices of choice for many applications because they can be made compact and are less costly.

1.2.4 Frequency Multipliers

Frequency multipliers [25] use a nonlinear device to produce photons at higher harmonic frequencies. The drive sources can be BWOs or solid state lasers [1] described in the preceding section. A chain of frequency doublers and triplers based on planar-Schottky varactor diodes can provide output powers of up to 20 mW [26] at frequencies around 300 GHz.

1.2.5 THz Semiconductor Lasers

The most promising THz semiconductor lasers are quantum cascade lasers (QCLs) [27, 28]. QCLs are comprised of a series of thin layers of semiconductor. The thickness of the layers is so small that this is referred to as one dimensional multiple quantum well confinement. Active wells are arranged in such a way that each layer is at a slightly lower energy than one before. A photon is emitted each time an electron cascades down a quantum well. The total number of photons emitted in this process is equal to the number of quantum wells. QCLs can operate between 1.9 and 4.8 THz [29]. The maximum power emitted by these devices is 50 mW [30]. Williams *et al.* [31] have reported on a THz QCL that operates at up to 164 K in pulsed mode and 117 K in CW mode. Two main problems yet to be solved regarding QCLs are reducing the minimum operational frequency and increasing the operational temperature [32]. Another THz semiconductor laser that deserves mention is the p-doped Ge laser. Its output power level and operation frequency range are shown in Figure 1.2. Recently, a resonance p-Ge laser tunable in the range from 1.2 to 2.8 THz and producing a maximum output power of 10 mW was reported [33].

1.2.6 THz Parametric Sources

THz Parametric Sources [34] generate THz radiation via the interaction of near-infrared (IR) photons and optical vibration modes inside nonlinear optical crystals such as $LiNbO_3$. During parametric interaction with the optical vibrational modes of the crystal, the energy of an input photon with frequency ν_p is partially depleted producing a Raman shifted Stokes photon with frequency ν_s. A THz signal of frequency $\nu_t = \nu_p - \nu_s$ is then produced by difference frequency generation between the pump and the Stokes photons. Recently, a CW optical parametric THz source that produces THz power levels exceeding 1 μW and tunable from 1.3 to 1.7 THz was demonstrated [35].

A similar method to THz parametric generation of THz radiation in which both input lasers are generated outside the non-linear crystal and coupled into the crystal for mixing is described by Saeedkia *et al.* [1] and Ding [36]. It is referred to as difference frequency mixing in nonlinear crystals.

1.2.7 THz Photomixers

Photomixing is based on optical heterodyne downconversion where a photoconductor or photodiode is illuminated by two laser beams with a difference frequency in the THz region [37]. The beat frequency of the two lasers will modulate the conductivity of the photomixer material. The variation of the conductivity is converted to electrical current and finally radiation by applying a bias voltage across the active region of the device. Figure 4.6 shows the basic photomixing arrangement. A 2x2 fiber coupler is used to combine two laser beams. One output of the 2x2 fiber coupler is connected to the photomixer while the

other can be used for power measurements. A detailed description of photomixing will be presented in chapters that follow.

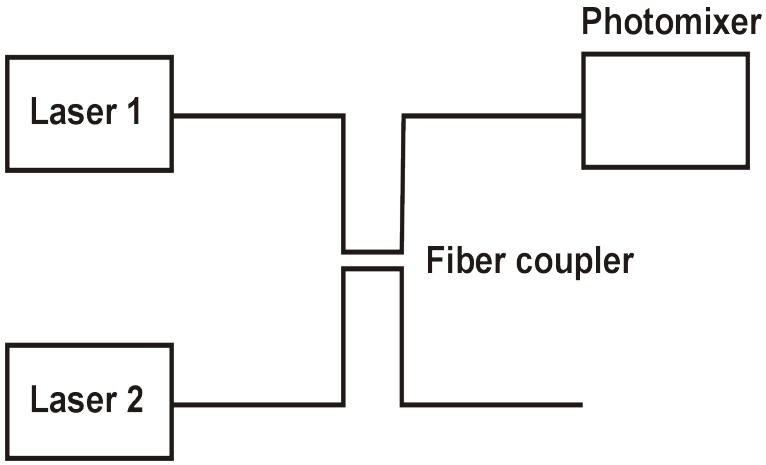

Figure 1.3: The conventional photomixing arrangement used for single frequency generation.

Major drawbacks with photomixers have been the low bandwidth, poor optical power coupling, impedance mismatch between the photomixer element and the load circuit, and degradation of the photomixer properties at high optical power. These have limited the output THz power to orders of a microwatt.

Despite the drawbacks mentioned above, the photomixer has attracted recent attention mainly because of its small volume, low power consumption, relatively low cost, ruggedness and room temperature operation. It has the potential to result in a compact and portable device. The original concept of photomixing exploits a short carrier lifetime (ultrafast) photoconductor (e.g. low-temperature-grown gallium arsenide (LTG-GaAs)) and uses laser wavelengths in the 800 nm range. The development of new semiconductor materials that operate at optical telecommunication wavelengths ($\sim$ 1550 nm) [38] has reduced the

cost of THz systems [1]. This is due to the fact that materials for optical telecommunication such as high speed photodiodes based on InGaAs, lasers, fibers, and couplers are readily available and are relatively cheap.

The most promising photomixer is the uni-traveling-carrier p-i-n photodiode (UTC-PD). A UTC-PD coupled to a log-periodic antenna (described in Section 3.2.2) has been reported to generate 2.3 μW at 1.02 THz with nearly 400 mW of input optical power. This is the highest THz power produced by a photomixer to date.

Table provides the state-of-the-art narrow band THz sources discussed in this Chapter in terms of their output power, operation frequency and cost.

Table 1.1: A comparison of the state-of-the-art narrow band THz sources in terms of their output power, operation frequency and cost.

hline Source	Size	Frequency (THz)	Output power (W)	Year reported
Gyrotron	bulky	0.14	1×10^{6}	2002 [12]
Free electron laser	bulky	0.89-4.76	2.4×10^{3}	- [14]
Quantum cascade laser	compact	1.38	0.2 (at 163 K)	2005 [31]
Tunnel injection transit time diode	compact	0.355	0.14	2005 [23]
Backward wave oscillator	bulky	0.3	0.05	2002 [39]
Optically pumped Far-IR Gas Lasers	bulky	2.5	0.03	1986 [19]
High-electron mobility transistor	compact	0.15	0.02	2004 [24]
Resonant tunneling diode	compact	0.342	23×10^{-6}	2005 [20]
Photomixer device	compact	1.04	2.3×10^{-6}	2005 [40]
Parametric interaction in nonlinear crystals	compact	1.3-1.7	1×10^{-6}	2009 [35]
Difference frequency mixing in nonlinear crystals	compact	0.09	0.106×10^{-6}	2004 [41]

1.3 Photomixers as local oscillators for heterodyne detection

Among the THz radiation sources described above, the photomixer has attracted the greatest interest in astronomy. This is mainly because of its application as a local oscillator source for heterodyne detection [42]. The photomixer satisfies most of the requirements for local oscillator (LO) systems, in that it is compact and so can be easily mounted on a telescope. It also has wide spectral coverage and high tunability, which is essential for the measurement of molecular lines and discovery of new species in the interstellar medium (ISM). It can also be used for synchronizing multiple instruments located at separated telescopes via the fibre optic link as in the Atacama Large Millimeter/submillimeter Array (ALMA) project. Figure 1.4 shows a schematic view of a heterodyne receiver system. The incoming THz signal from an astronomical source is combined with the LO signal. A mixer

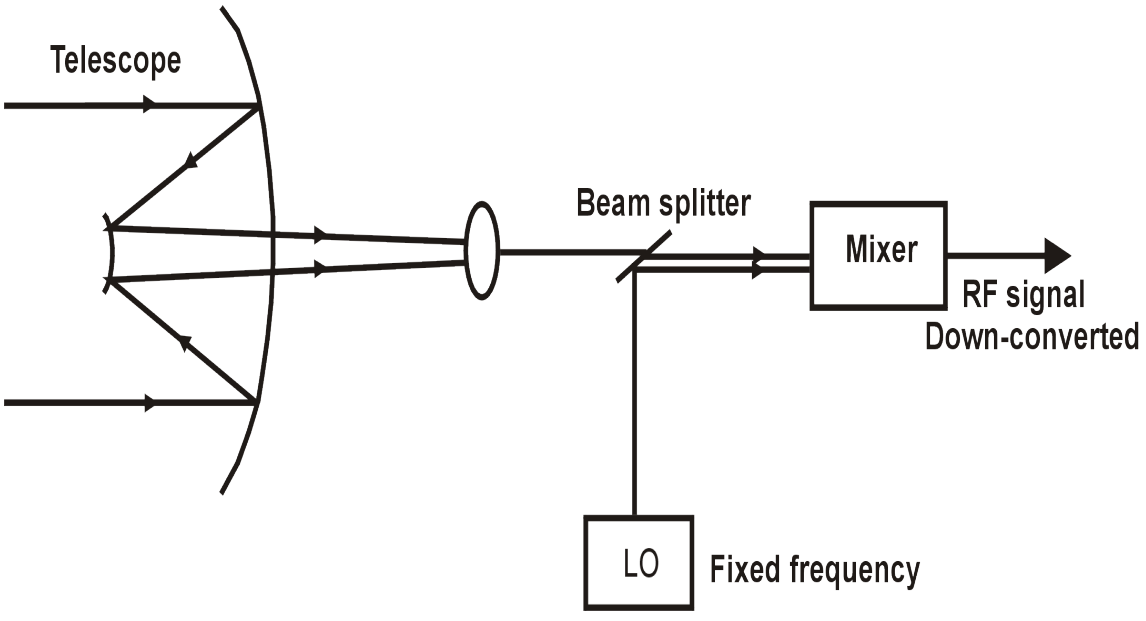

Figure 1.4: Schematic view of heterodyne receiver system.

is used to downconvert the beat frequency to an intermediate frequency (IF) signal. One of the requirements for mixers is that they should have a high bandwidth (several GHz) [43]. Examples of mixers currently being used in heterodyne systems are the semiconductor-insulator-semiconductor (SIS) [44] and the superconducting hot electron bolometer (HEB) mixers [45].

1.4 Thesis Summary

Chapter 2 reviews the principles and theory of photomixing. The current state of the art performance of different photomixers and antennae designs are discussed in Chapter 3. Chapter 4 describes the experimental configuration used to evaluate the THz photomixer our group purchased from the Millimeter Wave Technology (MMT) group at the Rutherford Appleton Laboratory (RAL), Oxford, UK. The University of Lethbridge Astronomical Instrumentation Group (AIG)'s Fourier transform spectrometer (FTS) and the very sensitive cryogenic detector used in this project are also described. The results from the characterization of the photomixer are presented in Chapter 5. Chapter 6 provides a summary of the thesis and outlines the directions of future work.

Chapter 2

The Photomixer: Principles of Generation of CW THz Radiation

2.1 Overview

In the previous Chapter, various sources of THz radiation were described. In this Chapter the principles of practice that underly the operation of the photomixer are presented together with its limitations. The properties of materials currently being used to perform fast operation in photomixers are also presented. The Chapter ends with results from a simulation of a LTG-GaAs photomixer using the derived equations and typical material parameters.

2.2 Principles of Operation of Photoconductors and Photodiodes

As is described in Chapter 1, photomixing describes the generation of THz radiation in a photoconductive device or photodiode when two spatially interfering laser beams of appropriate frequency are incident on the active region of the device. The following Section provides a description of the principle of operation of photoconductors and photodiodes.

2.2.1 Photoconductor

Photoconductors are devices that consist of a piece of semiconductor with two Ohmic contacts. When illuminated by electromagnetic radiation, the conductance of the semiconductor changes with the intensity of the incident optical power. Different photoconductors are sensitive to different wavelength ranges and have different time responses and optical sensitivities in those wavelength ranges. The sensitivity of these devices is high for photons with energies equal to or slightly greater than the band gap of the device. Some photoconductors are designed to respond to excitations of carriers from impurity levels within the band gap and so are sensitive to photons of energy less than the band gap.

When radiation is incident on the photoconductor, electron-hole pairs are generated. If we denote the steady state excess carrier generation rate by g_{op} (electron-hole pairs/cm$^3\cdot$ s), the mean time, in seconds, each carrier spends in its respective band before capture by τ (τ_e and τ_p for electrons and holes respectively), the change in photocarrier concentration is given by

$$\delta n_e = \tau_e g_{op} \text{ and } \delta n_p = \tau_p g_{op} \ [\text{cm}^{-3}] \tag{2.1}$$

where n_e and n_p are the excess electron and hole concentrations (in cm^{-3}) [46]. These result in a change in photoconductivity, $\delta\sigma$ given by

$$\delta\sigma = qg_{op}(\tau_e\mu_e + \tau_p\mu_p) = eg_{op}\tau(\mu_e + \mu_p) \ [\Omega^{-1}\ \mathrm{cm}^{-1}] \tag{2.2}$$

where q is the magnitude of the electronic charge, μ_e and μ_p are the electron and hole mobilities (in $\mathrm{cm}^2/\mathrm{V{\cdot}s}$). Equation 2.2 shows that in order to have maximum photoconductive response, the device must have high mobilities and long lifetimes. The last equality applies to simple recombination where $\tau_e = \tau_p = \tau$. If trapping is present, for example in LTG-GaAs, one of the carriers will spend little time in its band before being trapped. LTG-GaAs has high carrier mobility which leads to a short time response; an essential feature of a photomixer material (see Section 2.3). The photomixing technique using the photoconductive antenna was initiated by Brown *et al.*. in 1993 [37,47–49] and has since attracted increasing research interest [50–52].

2.2.2 Photodiode

In the previous Section, the use of a piece of semiconductor with two Ohmic contacts in devices called photoconductors was described. Photodiodes are essentially p-n diodes. When the diode is exposed to electromagnetic radiation, a photocurrent is produced. Photodiodes have a high speed of response and are more sensitive to high energy radiation than photoconductors.

Figure 2.1 shows a reverse biased p-n junction to which photons of energy $h\nu > E_g$ are incident. Here h is the Planck's constant, ν is the photon frequency and E_g is the band gap energy. When there is no incident radiation on the junction, carriers generated in the

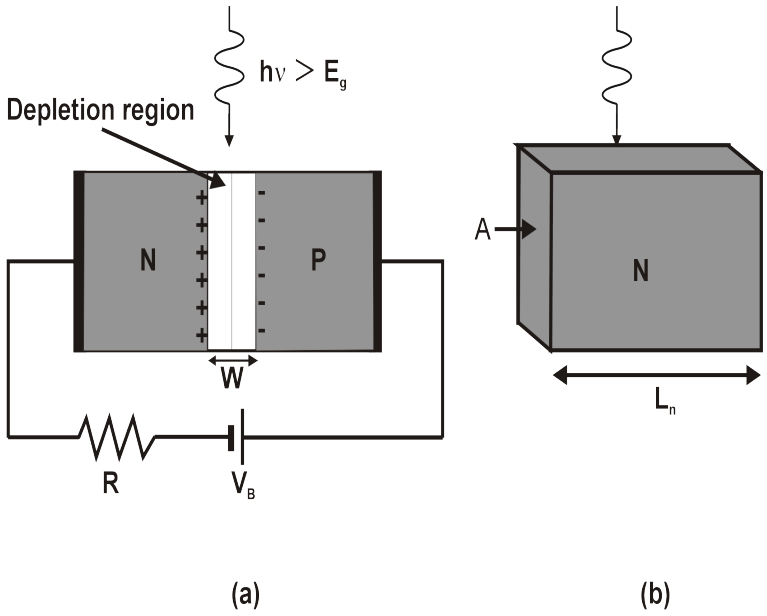

Figure 2.1: (a) A p-n junction under illumination by radiation of energy $h\nu > E_g$. Electrons generated within the depletion region W, are swept by the junction field and collected in the n region. Holes generated in the same region are collected in the p region. (b) A diffusion length of the junction on the N side. A is the cross-sectional area of the junction and L_n is called the electron diffusion length.

depletion region W are separated by the junction field with electrons being collected in the n-region and holes in the p-region. The distance at which the excess carrier distribution is reduced to $1/e$ of its value at the point of injection is called the diffusion length. Minority carriers generated thermally within a diffusion length of each side of the junction diffuse to the depletion region and are swept to the other side by the bias field. Illuminating the junction with photons of energy $h\nu > E_g$ results in an added generation rate, g_{op} (cm^3 s^{-1}). If the electron diffusion length is L_n then the number of electrons created per second within a diffusion length of the transition region on the p side is $AL_n g_{op}$. A is the cross-sectional area of the junction. Similarly if the hole diffusion length is L_p then the number of holes created per second within a diffusion length of the transition region on the n side is $AL_p g_{op}$.

AWg_{op} carriers are generated within the depletion region.

The collection of these optically generated carriers by the junction results in a current given by

$$I_{op} = eg_{op}A(L_n + L_p + W) \quad \text{[amperes]} \tag{2.3}$$

The diode equation can be written as

$$I = I_0(e^{\frac{qV}{kT}} - 1) = qA\left(\frac{L_p}{\tau_p}p_n + \frac{L_n}{\tau_n}n_p\right)(e^{\frac{qV}{kT}} - 1) \quad \text{[amperes]} \tag{2.4}$$

where I_0 is the reverse saturation current (sometimes called the thermally generated current), V is the bias voltage, k is the Boltzmann constant and T is the time. In order to find the total reverse current with illumination we add the optical generation of Equation (2.3) to the diode equation taking into account that this current is directed from n to p,

$$\begin{aligned} I &= I_0(e^{\frac{eV}{kT}} - 1) - I_{op} \\ I &= qA\left(\frac{L_p}{\tau_p}p_n + \frac{L_n}{\tau_n}n_p\right)(e^{\frac{qV}{kT}} - 1) - eg_{op}A(L_n + L_p + W) \quad \text{[amperes]} \end{aligned} \tag{2.5}$$

where p_n and n_p are the minority carrier concentrations on the n and p sides respectively. Equation (2.5) shows how the I-V curve of a p-n photodiode is lowered by an amount proportional to the generation rate (Figure 2.2), a result that will be shown for the photomixer in Chapter 5. To enhance the responsivity of a photodiode, an intrinsic region used as a major absorption layer is added to produce what are called p-i-n diodes [53]. It was Stöhr *et al.* who first demonstrated the use of photodiodes in photomixers [54–56]. Since then, photodiodes have attracted much interest. In particular, the development of an ultrafast photodiode called the uni-traveling-carrier p-i-n photodiode (UTC-PD) by Ishibashi *et al.* [57] has revolutionized the field of high speed photonics. UTC-PDs will be described in Section 3.3.2.

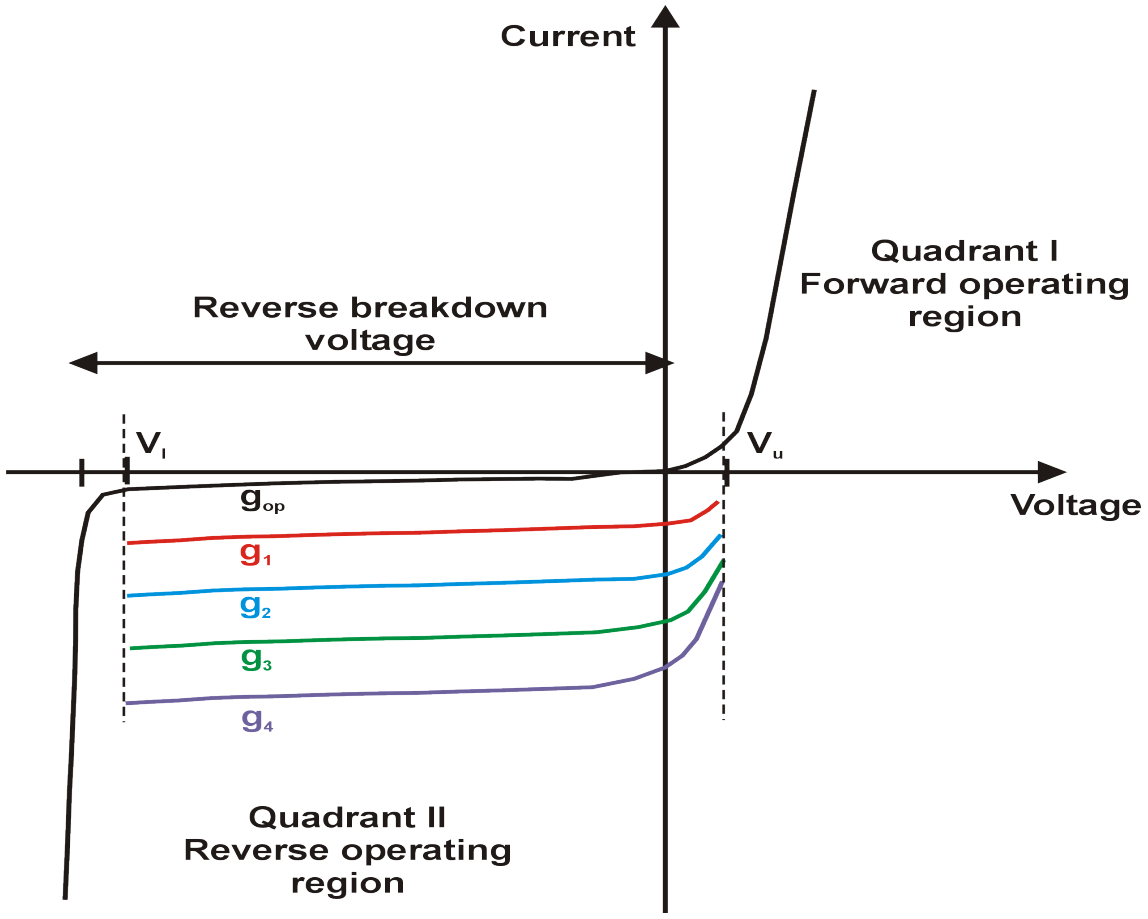

Figure 2.2: The V-I characteristic of a photodiode with no incident photons (g_{op}) and when illuminated by laser radiation of different powers (g_1, g_2, g_3 and g_4). Usually a photodiode is operated in the reverse bias region between a lower voltage limit of V_l and an upper voltage limit of V_u in order to avoid dielectric breakdown of the device.

2.3 Photomixer Materials

The physical basis of the photomixer is electron-hole generation by photon absorption in photoconductive materials like LTG-GaAs, erbium arsenide: gallium arsenide (ErAs:GaAs) and erbium arsenide: indium gallium arsenide (ErAs:InGaAs). These are

usually referred to as III-V semiconductor materials because of the positions of their constituent elements on the periodic table. LTG-GaAs was first used as a photomixer material at Lincoln Laboratory in 1992 [37, 58]. It is grown by an epitaxial growth technique called molecular beam epitaxy (MBE) at temperatures around 200 ^{0}C [52], while incorporating 1 % more arsenic than gallium. MBE is a high vacuum technique in which crucibles containing material components of the crystal to be grown are placed in the growth chamber. When the crucible is heated, evaporated atoms or molecules travel in straight lines and impinge on a heated substrate. Typically, the LTG-GaAs photomixer is fabricated on 1.5 μm thick LTG-GaAs layer grown on a semi-insulating GaAs wafer. The crystallinity of the material is maintained throughout the MBE growth process. The difficulty in controlling the growth temperature, incorporating the 1 % excess As and the photocarrier lifetime has been the major drawback in LTG-GaAs.

The material is then annealed at temperatures around 500 ^{0}C in order to increase the carrier mobility to useful levels (> 100 cm^2 V^{-1} s^{-1}). This also increases the resistivity and electrical breakdown field threshold of the material. The effect of the annealing is to re-arrange the As atoms on Ga sites causing anti-site defects (an As atom at a Ga site). Such anti-site defects are associated with well-defined defect states at the center of the GaAs bandgap so that they support very rapid electron-hole recombination via the Shockley-Read-Hall mechanism [59] and do not impact ionize under high internal fields. These small deviations from the stoichiometry of the material are important to ensure that the photocarrier lifetime is short (≈ 0.5 ps) [43, 60].

The properties of LTG-GaAs discussed so far are: subpicosecond electron-hole re-

combination time, τ, and a high electron mobility ($\mu_e \sim 200$ cm^2 V^{-1} s^{-1}) [37]. In addition to these properties, LTG-GaAs also has high direct current (DC) breakdown-field threshold ($E_B > 3 \times 10^5$ V cm^{-1}). The main property of LTG-GaAs that is important to photomixing is its bandgap wavelength which is approximately 850 nm. This means that it can be used with commercially available laser diodes operating between 800 nm and 850 nm.

To address the problems in fabricating LTG-GaAs and also to develop photomixers which use lower power, researchers are now exploiting technologies developed by the optical fiber telecommunications industry at 1550 nm. This has led to the use of ErAs:GaAs as a photomixer material. Unlike LTG-GaAs which has a single layer, ErAs:GaAs is a composite material with thin layers of ErAs embedded in GaAs during MBE growth which is done at 535 ^{0}C [58,61,62]. ErAs is a semi-metallic material and is similar in properties to As. During growth, the ErAs self-assembles into nm-scale islands embedded between high crystalline GaAs layers. These nanoparticles act as nonradiative recombination centers, similar to the As precipitates in LTG-GaAs. ErAs:GaAs has proven to have a significantly higher photocarrier mobility than LTG-GaAs, subpicosecond response time and a high breakdown field ($> 2 \times 10^5$ V cm^{-1}) [62].

In concluding this section, it is important to point out that the advances in III-V optoelectronic devices and solid state lasers over the past two decades has revived interest in THz power generation by photomixing. The applicability of III-V materials in photomixing is due to their bandgap energies which are lower than the photon energy of the communication band which enables them to be used with readily available and inexpensive tunable telecommunications laser diodes close to 1550 nm.

2.4 LTG-GaAs Photomixer

It is important to know the theory behind the generation of photocarrier pairs in the materials that have been discussed in the previous section. A LTG-GaAs photomixer is made up of two sets of interdigitated metal electrodes deposited on the top surface of the LTG material as shown in Figure 2.3(a) and (b). It is important that the band-bending at the metal-semiconductor junctions (Figure 2.4) be small to make sure that the photocarrier collection process is photoconductive and not photovoltaic. In this case, the photomixer can be represented electrically by a photoconductance $G(t)$ [in Ω^{-1}], that is dependent on the absorbed optical power [37]. Figure 2.3(c) shows the equivalent circuit diagram of the photomixer coupled to an antenna. Since the absorption strength, photocarrier mobility and recombination time of the photomixer are all independent of the electrode voltage V, $G(t)$ is approximated as an ohmic conductance. $G(t)$ is in parallel with a capacitance C, that is a function of the electrode geometry and the dielectric constant of the photoconductive material. The planar circuit or antenna to which the electrodes are connected is represented by a resistance R_L ($\sim$ 72 Ω). V_B is a voltage source representing the electrical bias.

The active area of the photomixer is of the order of a few microns which makes the photomixer very sensitive to high electric fields. In order to help distribute the electric field uniformly in the semiconductor, interdigitated electrodes shown in Figure 2.3(a) and (b) were implemented. It has been shown that the best configuration consists of photodetectors with finger-shaped anodes having a width of the order of 1 μm [52]. This configuration has to be optimized to improve the performance of the device [63, 64]. It has been shown that instead of having surface contacts, the use of recessed metal-semiconductor-metal (MSM)

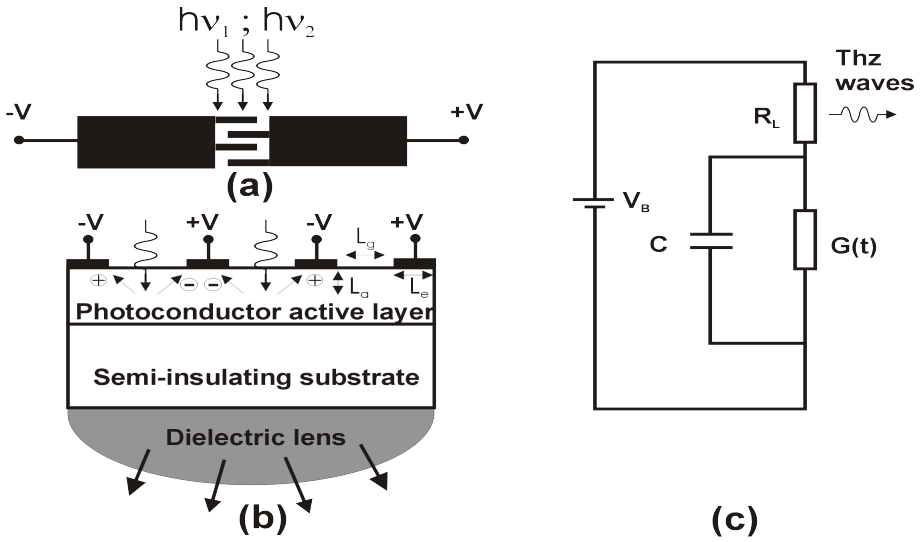

Figure 2.3: Arrangement of interdigitated electrodes in an antenna coupled photomixer, (a) top view, (b) cross-sectional view of photomixer showing the coupling of THz radiation by a dielectric lens and (c) the equivalent circuit diagram of the photomixer and external broadband load circuit

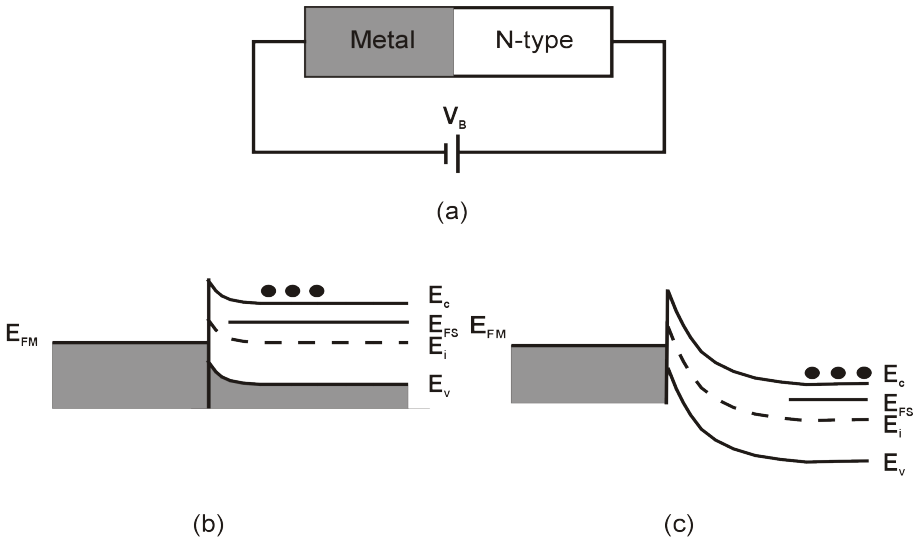

Figure 2.4: (a) A metal-semiconductor junction, (b) the band diagram for a metal-semiconductor junction at equilibrium (Fermi levels are equal) and (c) the band diagram when the metal is connected to the negative terminal of the battery which results in the widening of the depletion region.

interdigitated contacts results in an improvement in the output THz power. This is due to an increase in the electric-field strength in the central absorption region of the recessed devices. In order to derive an expression for $G(t)$ for the interdigitated photomixer, the following assumptions are made:

1. the electrodes are opaque to the incident radiation,

2. The bias electric field E_B between the electrodes is uniform in a volume defined laterally by the area of the gaps and vertically to a depth of L_a and

3. the instantaneous optical power absorbed per unit volume is uniform in the volume defined in item 2 above.

Thus $G(t)$ can be approximated as [37, 65]

$$G(t) = n(t)e(\mu_e + \mu_h)\frac{N_g L_a L_e}{\omega_g} \ \ [\Omega^{-1}] \tag{2.6}$$

where μ_e and μ_h are the electron and hole mobilities respectively, N_g is the number of gaps and L_e is the length of the electrodes, w_g is the width of the gaps between the electrodes and $n(t)$ is the instantaneous photocarrier pair density throughout the absorption volume. The photocarrier density $n(t)$, is a solution to

$$\frac{dn(t)}{dt} = \frac{\eta_e P(t)}{h\nu \cdot L_e \cdot L_a(N_g w_g + N_e w_e)} - \frac{n(t)}{\tau} \ \ [\mathrm{cm}^{-3}\ \mathrm{s}^{-1}] \tag{2.7}$$

where η_e is the external quantum efficiency of the photomixer, which takes into account the reflection due to metal electrodes, w_e is the width of the electrodes, N_e is the number of illuminated electrodes, $h\nu$ is the photon energy, $P(t)$ is the optical power incident on the active region of the photomixer and $P(t)/L_e(N_g w_g + N_e w_e)$ is the incident optical power

density on the top of the photomixer. According to the assumptions, η_e is given by

$$\eta_e = \eta \frac{N_g w_g}{N_g w_g + N_e w_e}(1 - r) \tag{2.8}$$

where r is the reflectance of the top of the photomixer and η is the internal quantum efficiency defined as the number of photocarrier pairs generated per photon entering the photomixer material.

2.5 Optical Heterodyne Conversion

In THz photomixers, two coherently interfering optical modes generated by two single-mode CW lasers or by a dual-mode laser are used to illuminate the interdigitated-electrode region of the ultrafast photoconductive material [1, 37, 66]. The total electric field of the interfering beams is simply the linear sum of the two individual fields which beat at the difference frequency. For two beams with powers, P_1 and P_2 and frequencies, ν_1 and ν_2, the combined instantaneous power incident on the active region of the photoconductor is [37, 65]

$$P(\omega, t) = P_1 + P_2 + 2\sqrt{mP_1P_2}\Big[\cos 2\pi(\nu_2 - \nu_1)t + \cos 2\pi(\nu_2 + \nu_1)t\Big] \quad [\mathrm{W}] \tag{2.9}$$

where m is the mixing efficiency that ranges in value between 0 (no overlap) and 1 (perfectly matched). From Equation (2.9) one can tell that when two laser beams impinge on a photoconductor or photodiode, they induce current components at the sum and difference frequency. However, two conditions have to be satisfied for generation of THz power; $h\nu_1$ and $h\nu_2$ must be greater than the bandgap of the photoconductive material used (this is 1.42 eV for room temperature GaAs) and $\nu_1 \approx \nu_2$ such that the difference frequency

$f =\mid \nu_2 - \nu_1 \mid$ falls in the microwave band. Under these conditions, the first cosine term in Equation (2.9) modulates the photoconductance at the difference frequency f but the second term, approximately twice the optical frequency varies on a time scale much shorter than the electron-hole recombination time τ, and so does not modulate the photoconductance significantly. Neglecting this term, we obtain [66],

$$P(\omega, t) = P_0 + 2\sqrt{mP_1P_2}\cos\omega t \quad [\mathrm{W}] \tag{2.10}$$

where, $P_0 = P_1 + P_2$ is the total incident power averaged over a long time period, $\omega = 2\pi f = 2\pi(\nu_2 - \nu_1)$.

A solution for $n(t)$ is obtained by substituting Equation (2.10) into Equation (2.7) to obtain

$$n(t) = \frac{\eta(1-r)\tau N_g w_g P_0}{h\nu(N_g w_g + N_e w_e)^2 L_e L_a}\left(1 + \frac{2\sqrt{mP_1P_2}\sin(\omega t + \phi)}{P_0\sqrt{1+\omega^2\tau^2}}\right) \quad [\mathrm{cm}^{-3}] \tag{2.11}$$

where $\phi = \arctan(1/\omega\tau)$. By substituting Equation (2.11) into Equation (2.6), we obtain

$$\begin{aligned} G(t) &= \frac{\eta\tau e(\mu_e + \mu_h)N_g^2 P_0(1-r)}{h\nu(N_g w_g + N_e w_e)^2}\left(1 + \frac{2\sqrt{mP_1P_2}\sin(\omega t + \phi)}{P_0\sqrt{1+\omega^2\tau^2}}\right) \\ &\equiv G_0[1 + \beta\sin(\omega t + \phi)] \quad [\Omega^{-1}] \end{aligned} \tag{2.12}$$

where,

$$G_0 = \frac{\eta\tau e(\mu_e + \mu_h)N_g^2 P_0(1-r)}{h\nu(N_g w_g + N_e w_e)^2} \quad [\Omega^{-1}] \tag{2.13}$$

and,

$$\beta = \frac{2\sqrt{mP_1P_2}}{P_0\sqrt{1+\omega^2\tau^2}} \tag{2.14}$$

where G_0 is the DC photoconductance for an average incident power P_0. When the optical

power is low, G_0 is related to the short-circuit external current responsivity S by

$$S \approx \frac{G_0 V_B}{P_0} = \frac{\eta\tau e(\mu_e + \mu_h)N_g^2 V_B(1-r)}{h\nu(N_g w_g + N_e w_e)^2} \text{ [A/W]} \tag{2.15}$$

This equation is important when comparing the intrinsic material properties to the measured responsivity. The time-dependent conductance in Equation (2.12) will modulate the bias current from V_B at a frequency f delivering power to the photoconductive antenna resistance R_L in the process. This power can be obtained by solving the dynamic current equation for the equivalent circuit of the photomixer in Figure 2.3(c). Using Kirchoff's current law, the dynamic current equation for Figure 2.3(c) is obtained as

$$C\frac{d\upsilon(t)}{dt} = \frac{V_B - \upsilon(t)}{R_L} - G(t)\upsilon(t) \tag{2.16}$$

In order to solve this equation, we need to make an assumption that the voltage across the photomixer active region υ(t) is harmonic, i.e. $\upsilon(t) = \text{D e}^{i(\omega t+\phi)}$ where D is a constant. We proceed by setting $\phi = 0$ in Equation (2.12). This can be done without loss of generality since the phase of the photocarrier density is arbitrary. Now, substituting Equation (2.16) into Equation (2.13) and neglecting terms that vary with time as $2\omega t$, we obtain the output radiation power as

$$P_{THz}(\omega) = \frac{\frac{1}{2}(V_B G_0 \beta)^2 R_L[(1+G_0R_L)^2 + (\omega R_L C)^2]}{(1+G_0R_L)^2[(1+G_0R_L)^2 + (\omega R_L C)^2 - \frac{1}{2}(G_0 R_L \beta)^2]} \tag{2.17}$$

Equation (2.17) is useful in the design of photomixers in that it points to three of their important properties:

1. For fixed ω, R_L and P_0, the value of $P_{THz}(\omega)$ is maximum when there is complete spatial overlap of the two laser beams (i.e. $m = 1$) and $P_1 = P_2 = P_0/2$.

2. In the small-signal approximation, where $G_0 R_L \ll 1$, and using the above property, Equation (2.17) reduces to

$$P_{THz}(\omega) = \frac{\frac{1}{2}(V_B G_0)^2 R_L}{[1 + (\omega\tau)^2][1 + (\omega R_L C)^2]} \tag{2.18}$$

where $V_B G_0$ is the DC photocurrent. Equation (2.18) shows that the THz output power is proportional to the radiation resistance of the antenna, the square of the bias voltage, V_B^2, and the square of the DC conductance, G_0^2. The effect of optical power on the THz output power is described by Equation (2.13) which shows that G_0 is proportional to P_0 and to the effective carrier mobility $\mu = \mu_e + \mu_h$ and lifetime, τ. Typically, the frequencies generated by the photomixer are in the range from a few tens of GHz to a few THz. The optical-to-THz conversion efficiency is about 10^{-5} and the typical power is in the microwatt range.

3. If R_L is not frequency dependent as is the case in self-complementary antennae, such as spiral and log-periodic antenna, the bandwidth of the photomixer is limited by the carrier lifetime and the RC time constant. A description of antennae currently in use with photomixers is provided in Chapter 3. At the high frequency limit, where $\omega\tau \gg 1$ and $\omega R_L C \gg 1$, the small-signal expression for P_{THz} in Equation (2.18) reduces to

$$P_{THz}(\omega) = \frac{\frac{1}{2}(V_B G_0)^2 R_L}{\omega^4 (\tau R_L C)^2} \tag{2.19}$$

Equation (2.19) shows that the THz power drops at 12 dB/octave in the high frequency limit. It is therefore important for the photomixer to have low τ and C. The inverse dependence on the fourth power of the frequency requires increasingly more sensitive and expensive detectors.

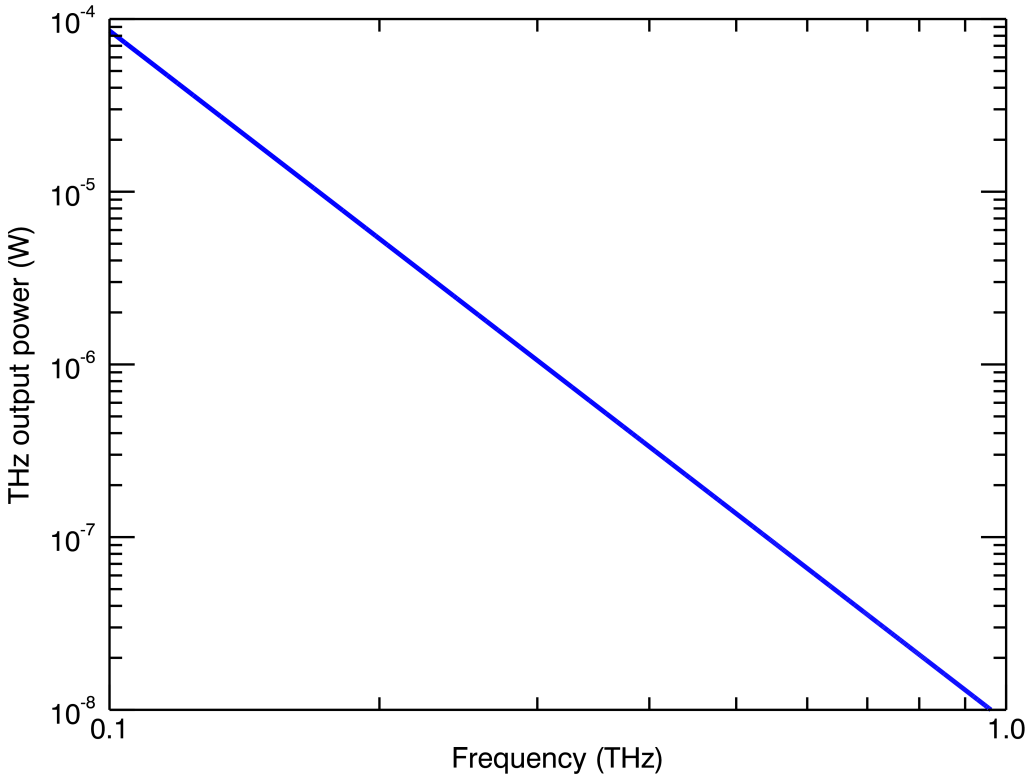

Figure 2.5: The variation of THz output power with frequency for a LT-GaAs photomixer. The THz output was calculated using Equation (2.18). The THz power drops at 12 dB/octave.

Figure 2.5 shows results from a simulation of a LTG-GaAs photomixer done using Equation (2.18). The device parameters were chosen to be as close as possible to those of the photomixer used in this thesis which will be discussed in Chapter 3. The parameters were set as: $w_g = 0.2$ μm, $w_e = 1.8$ μm, $N_g = 9$, $N_e = 10$, $\tau = 0.25$ ps, $\varepsilon = 12.8$, $\mu_e = 200$ cm^{2}V^{-1}s^{-1} $\mu_p = 150$ cm^{2}V^{-1}s^{-1}, $\eta = 0.9$, r = 0.3, $R_L = 72$ Ω, C = 6.5 fF and $V_B = 0.5$ V. The optical pump frequency and total optical input power were chosen to be 1550 nm and 10 mW respectively [65].

Before concluding this Section, it is important to look at the energy dissipated in the photoconductor resistance by analyzing Equation 2.7. Solving Equation 2.7 for the steady state solution, i.e using a constant, time averaged value of P, gives Equation 2.13. Thus the energy dissipated in the photomixer is

$$P_{Joule}(\omega) = G_0 V_B^2 = \frac{\eta\tau e(\mu_e + \mu_h) N_g^2 V_B^2 P_0 (1-r)}{h\nu(N_g w_g + N_e w_e)^2} \tag{2.20}$$

Equation 2.20 shows that the energy dissipated in the photomixer is directly proportional to the square of bias voltage. In practice, the bias voltage is governed by the current threshold at which the power dissipated as heat causes damage to the photomixer. The maximum THz power at the DC limit is obtained by back substitution of Equation 2.20 into Equation 2.19. The typical damage threshold for conventional LTG-GaAs photomixers with active areas of 50 μm^2 to 100 μm^2 ranges from 50 mW to 100 mW [43]. This corresponds to an incident laser power of approximately 10^5 W/cm^2. It has been demonstrated that LTG-GaAs photomixers installed in a cryostat have greater thermal conductivity and therefore can withstand high optical powers [7]. This was not attempted in this thesis since it is an expensive procedure which requires redesigning of our cryostats. The damage threshold for the photomixer can be increased by changing the substrate material [42].

2.6 Conclusions

In this Chapter, the principle of generation of THz radiation using photomixers based on photoconductors and photodiodes has been described. The properties of materials currently being used to make photomixers, were also described. It has been shown that the THz output is directly proportional to both the square of the bias voltage and the square

of the photoconductance and hence the total incident power. However, the bias voltage cannot be increased indefinitely. It is limited by the current threshold at which the power dissipated as heat causes damage to the device and also the ω^{-4} dependence. Chapter 3 will discuss available solutions to low THz power, the various designs of photomixers and their antennae.

Chapter 3

The Photomixer: State of the Art

3.1 Overview

The maximum THz power of the photomixer is currently limited by a thermal damage threshold due to joule heating to the level that is too low for some practical applications as stated in Section 2.5. There have been efforts to solve this problem by optimizing the antenna design and the substrate material. However, the THz output power remains relatively low. This Chapter will focus on the work that is being done to improve the performance of this device. The various antenna designs that have been investigated and reported are described in Section 3.2. Section 3.3 will describe the photomixer designs that are currently being implemented. The Chapter concludes by a description of the design of the Millimeter Wave Technology (MMT) photomixer, that I used in this thesis.

3.2 Photomixer Antenna Designs

The device that has been used to emit the generated THz radiation into free space in conventional LTG-GaAs photomixers is the silicon hyperhemispherical substrate having a typical diameter of 10 mm [43]. It was shown from Equation (2.17) that in the small signal approximation, the THz output power is proportional to the radiation resistance of the antenna. Typical values of the impedance of planar antennae on dielectric substrates are less than a few 100 Ω on LTG-GaAs (dielectric constant, $\varepsilon = 12.8$). This is very low as compared to the resistance of the LTG-GaAs photoconductor which is greater than 10 kΩ when illuminated with maximum possible power before thermal breakdown. Under these circumstances, the photomixer acts as a current source loaded with the antenna under highly mismatched conditions. The use of a monolithically integrated matching circuit has proven to solve this problem and increase the output THz radiation accordingly [67].

Conventional photomixers have often used broadband self-complementary antenna designs such as the log-spiral, log-periodic and bow-tie antenna that have relatively low resistance ($\sim$ 72 Ω) [7, 43, 49]. The use of antennae with high resistance has resulted in an increase in the output Thz power. This section describes the low impedance antenna designs (i.e log-spiral, log-periodic and bow-tie antennae) and high-impedance antenna designs (i.e dual dipole, dual slot, folded dipole, resonant and Yagi-Uda antennae). Most of the antennae that will be described in this Section are planar. These have the advantage that, they can be easily fabricated along with the mixing device on the same substrate. In Section 3.3.5 a photomixer coupled to a hollow waveguide is described. This is the type of photomixer used in this thesis. Its advantages are that it can provide optimized circuit impedance matching

by the use of stub tuners, and can be easily interfaced with standard waveguide components and high gain horn antennae [64]. It should be noted, however, that this list is not exhaustive of all THz antennae. There are other antennae like the carbon nanotube antenna [68, 69] and integrated horn antennae [70] which are not described here.

3.2.1 Logarithmic-spiral Antennae

Figure 3.1 shows an optical micrograph of a self complementary logarithmic spiral (often referred to as a log-spiral) antenna with interdigitated electrodes. This type of antenna, together with the logarithmic-periodic antenna is easy to design and fabricate. Submicron resolution is not required anywhere else except on the interdigitated electrodes.

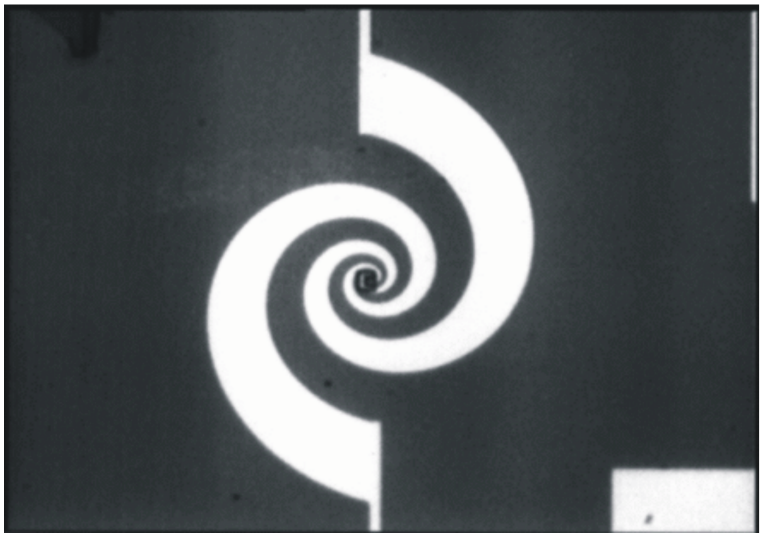

Figure 3.1: Optical micrograph of a log-spiral antenna with interdigitated electrodes. Micrograph courtesy of Frank Renner, Institut für Technische Physik I, Universität Erlangen-Nürnberg, German. [71]

The antenna pattern is symmetrical. The spiral has to be wrapped with sufficient turns so that the required lowest frequency radiates away before reaching the outer arms of the

spiral. The bias is supplied by bonding wires to the arms of the spiral. One advantage of the broadband self-complementary antennae is that they do not need chokes or other radio frequency (RF) passive components.

The driving impedance of a log-spiral antenna is real and independent of frequency [60]. The value of the driving-point impedance is given by

$$R_L = \frac{60\pi}{\sqrt{\varepsilon_{eff}}} \tag{3.1}$$

where ε_{eff} is the effective dielectric constant. For a planar antenna on a dielectric half-space, ε_{eff} can be approximated by $(1+\varepsilon)/2$, where ε is the dielectric constant. This gives $R_L = 72\ \Omega$ for GaAs which has a dielectric constant of 12.8. The radiation pattern of the log-spiral antenna is the desired quasi-Gaussian beam which is azimuthally symmetric but circularly polarized.

3.2.2 Logarithmic-periodic Antennae

Logarithmic-periodic antennae (Figure 3.2) fall in the same category as logarithmic-spiral antennae. They are not easy to design because of their complicated structure. Tonouchi *et al.* [72] demonstrated that logarithmic-periodic antennae perform better than other broadband self-complementary antennae. It has also been demonstrated that UTC-PDs integrating a planar log-periodic antenna exhibit a record power of 2.3 μW at 1.04 THz with good linearity [40].

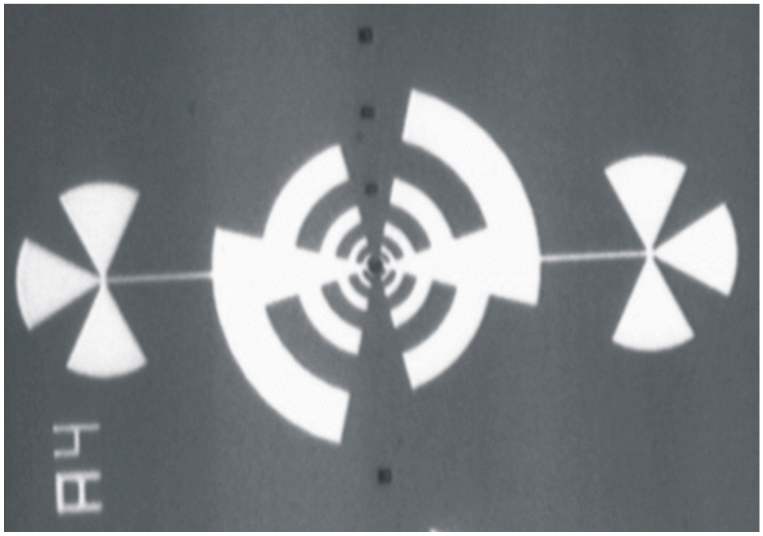

Figure 3.2: Optical micrograph of a log-periodic antenna. The power is emitted at the corresponding dipole branch. Micrograph courtesy of Frank Renner, Institut für Technische Physik I, Universität Erlangen-Nürnberg, German. [71]

3.2.3 Bow-Tie Antennae

Centrally fed bow-tie antenna have also been demonstrated for use as THz antenna [66]. These are a planar version of the bi-conical antenna. Like other planar antennae, bow-tie antennae are wide band in nature. Figure 3.3 shows a bow-tie antenna with interdigitated electrodes. The metal electrodes play a double role, as bias supply lines and as antennae.

3.2.4 Dipole Antenna

Dipole and slot antennae are examples of resonant antennae which have high impedance at the resonance frequencies. Tuning is required to make sure that the capacitive part of the impedance associated with the electrode with the inductive part of the antenna and DC line impedance [73, 74]. Thus at the resonance frequency, the antenna impedance is a real number (pure resistance) and the THz output power is not limited by the RC time

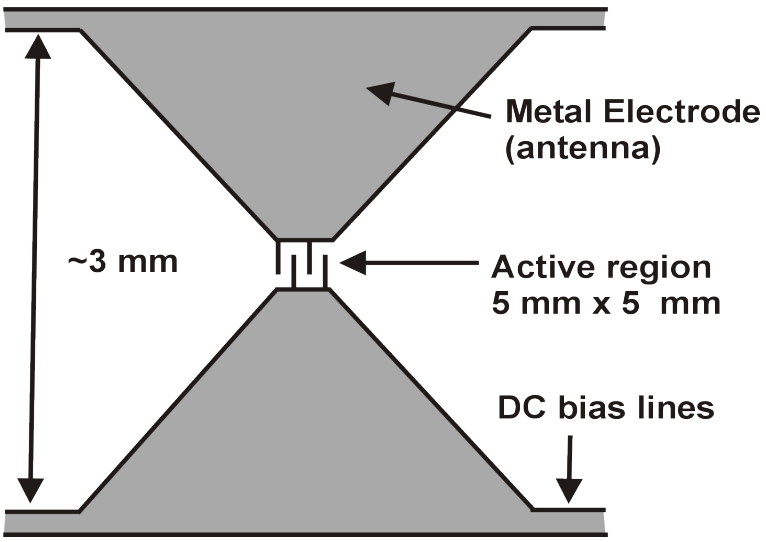

Figure 3.3: Schematic view of a bow-tie antenna with interdigitated electrodes

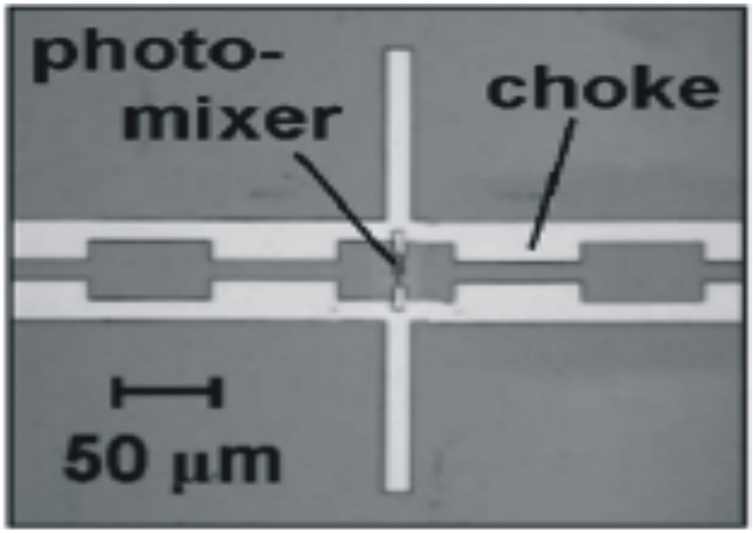

Figure 3.4: Optical micrograph of a choked dipole antenna. Courtesy of Gregory [66]

constant. Three types of dipole antenna have been used with photomixers; single-dipole, dual-dipole and dipole-slot antennae. Figure 3.4 shows a single dipole antenna design. It

can be used with interdigitated electrode and requires a choke.

Figure 3.5(a) shows a dual-dipole antenna design. Here the photoconductor is connected to twin-dipole antennae with a coplanar strip (CPS) transmission line whose length has been tuned to cancel out the electrode capacitance [43]. It has the advantage that its circuit design is flexible for tuning at high frequencies and has a symmetric, near Gaussian, beam pattern compared with the single dipole design which has relatively large side lobes. This is due to the fact that the required inductive tuning for the dual-dipole antenna is half that for the single dipole antenna. Another dipole antenna that has the potential to produce high frequency is the dual-slot antenna Figure 3.5(b) [43,74]. A folded dipole antenna has been demonstrated to have a high input impedance of approximately 3000 Ω. The beam pattern of slot and dipole antennae is asymmetric and quite broad in the H (dipole) and E (slot) plane, but has the preferred linear polarization.

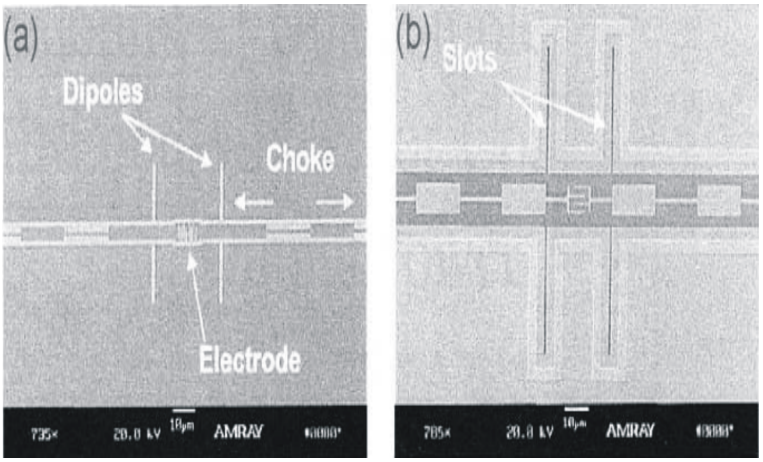

Figure 3.5: SEM photographs of (a) dual dipole and (b) dual slot antennae Courtesy of Duffy [74].

3.2.5 Yagi-Uda Antenna

The proposed Yagi-Uda Antenna has the potential of achieving better impedance matching with a photomixer by using a full-wavelength dipole as the driver element instead of a half-wavelength dipole [75]. Figure 3.6 shows a schematic of the Yagi-Uda antenna. It is designed on a GaAs substrate measuring about 1200 μm x 400 μm x 4 μm with a dielectric constant of 12.8. The antenna is made up of a driver, directors, reflectors, and the photomixer, which is located at the center of the drive. The DC bias is applied by the use of a CPS type of bias line. This technique promises to increase the input resistance of the

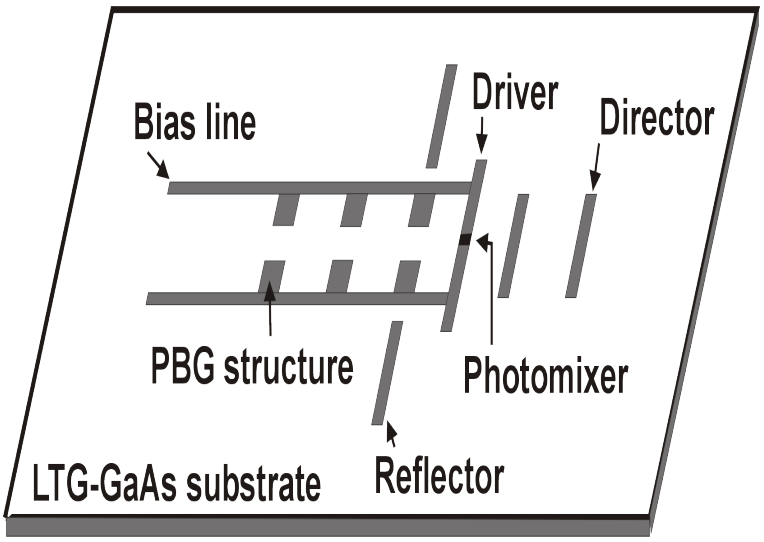

Figure 3.6: Schematic of the Yagi-Uda antenna

photomixer. This is because the technique uses a full-wave dipole antenna with an input resistance 10 times greater than that of a conventional half-wavelength dipole. Another factor is the low dielectric constant of the substrate on which the antenna is designed, allowing for a higher input resistance than would be possible for an antenna on a thick

substrate. When implemented, this design is expected to have an impedance of 2590 Ω at a typical resonance frequency of 590 GHz [75]. Most proposed applications of THz radiation will not benefit from this device because it cannot provide CW radiation.

3.3 Photomixer Designs

3.3.1 Large Active Area Designs

To avoid the problem of thermal failure due to increased optical power, the active area of the photomixer can be increased. However there are limitations in designing these devices. One of the limitations is the requirement to produce coherent (inphase) superposition of the generated THz waves. Devices with small areas comparable to the wavelength of the radiation automatically exhibit a high degree of coherence.

Single Large Active Area Design

An active area with a large aperture, biased with a high voltage can be illuminated with a high-power laser as shown in Figure 3.7. Coherent overlap of the generated THz waves is guaranteed as long as the incident optical wavefront is parallel to the surface of the active region. An antenna may not be necessary if the active region is greater than the wavelength of the THz wave. Darrow *et al.* [76] have successfully demonstrated this approach.

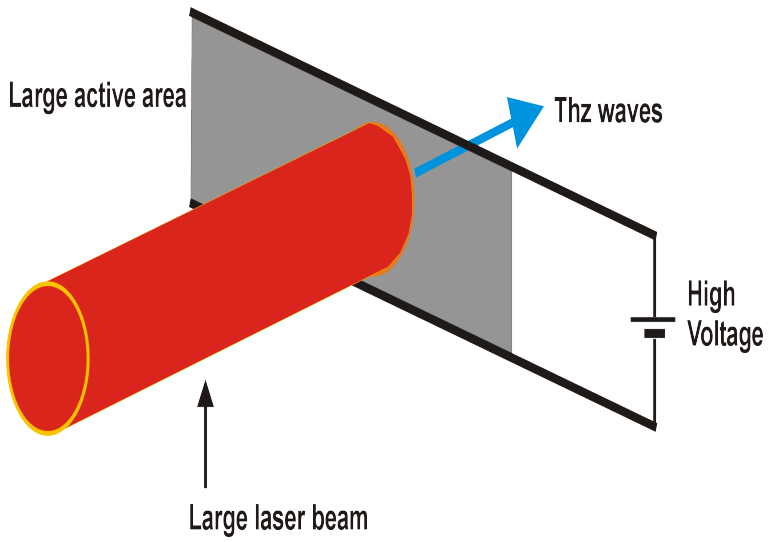

Figure 3.7: Single large active area photomixer

Array Antenna

It is possible to increase the output power of photomixers by combining the output of many single small-area photomixer elements configured as a two-dimensional array. This design is borrowed from RF phased-array antenna technology where it has been shown that the configuration works better with resonant antennae separated by approximately half the free-space wavelength. The generated THz radiation from the elements of the array will interfere constructively at a point equidistant from all elements provided that the THz waves all have the same amplitude and phase. To satisfy these requirements a single laser beam is divided into N laser beams by a 1:N tree coupler or a dielectric waveguide making sure that the optical path difference between the power splitter and each photomixer element is exactly equal. Figure 3.8 shows a configuration in which velocity-matched distributed photomixers are fed by dielectric waveguide feeds. After splitting a pair of single frequency

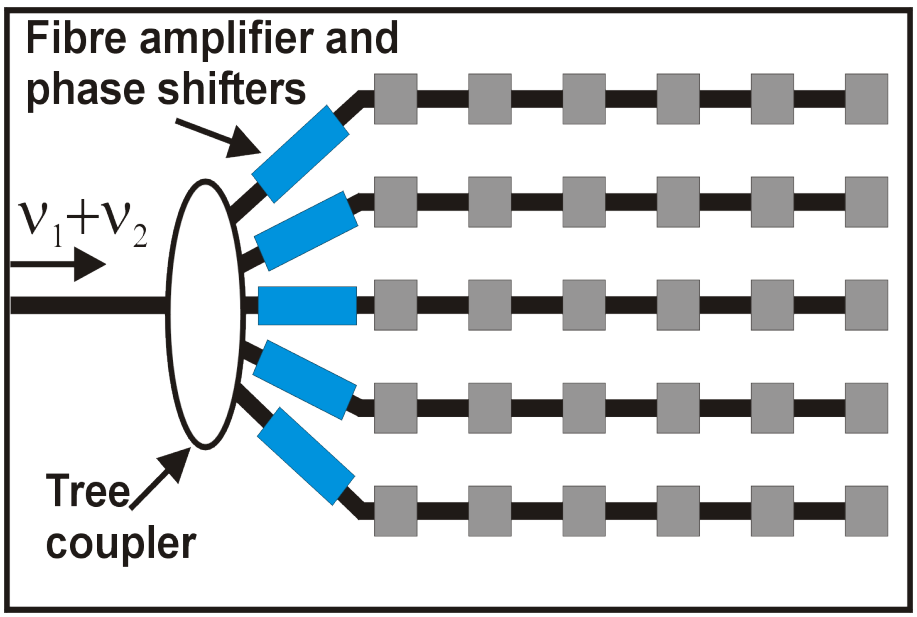

Figure 3.8: An array of velocity-matched photomixers fed by a dielectric waveguide through fibre amplifiers and phase shifters.

laser lines, the optical power may not be enough to drive photomixers. The use of erbium doped fiber amplifiers (EDFAs) helps to amplify the optical power to required levels.

Travelling-Wave Photomixers

Traveling-wave photomixers resulted from an effort to avoid the thermal failure of photomixers by reducing the optical and ohmic heat power density. Such efforts also gave rise to array antennae [43] and single large active area designs [76]. In a traveling-wave photomixer, an optical heterodyne signal is launched into an optical channel waveguide where it is gradually absorbed [77–80]. This results in a distributed current generation contributing to the overall current propagating along the electrical transmission line.

Figure 3.9 shows a traveling wave photomixer design. The THz waves are generated in a distributed active area. They then propagate along the microwave transmission

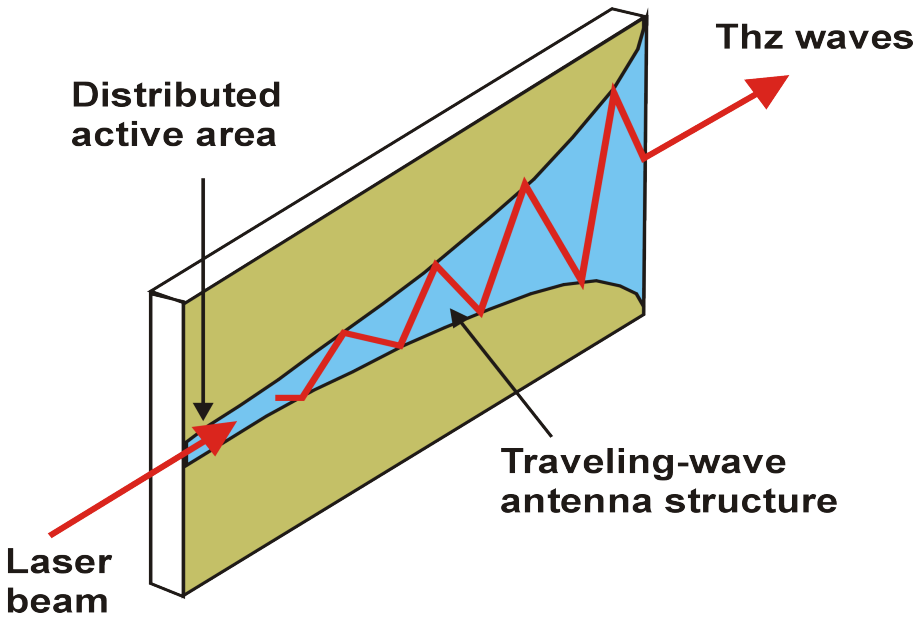

Figure 3.9: Traveling-wave photomixer design

line maintaining the coherent superposition condition. Terminating the transmission line is an antenna which then radiates the THz waves. The bandwidth of the traveling-wave photomixer is not RC time constant dependent but is limited by the carrier lifetime of the LTG-GaAs and the frequency dependent loss of the coplanar strip (CPS). The reported maximum THz output power of a free-space traveling-wave photomixer with a log-periodic antenna is slightly greater than 0.1 μW in a wide range extending to 3 THz.

3.3.2 Unitraveling-Carrier p-i-n Photodiode

The UTC-PDs developed at NTT Co. in Japan are quite promising. Basically, a UTC-PD is a conventional *pin* photodiode but with a p-doped narrow absorption layer (indium gallium arsenide (InGaAs)) and a separate undoped wide-band carrier collection

layer (indium phosphide (InP)) [57, 77, 81]. In these devices, only electron transport occurs since the majority carriers in the p-doped absorption layer are the photogenerated holes. This leads to higher device operation speed and higher output saturation current as compared with conventional pin-photodiodes (PDs) in which both electrons and holes are active carriers. UTC-PD have been demonstrated to achieve a wide bandwidth and a high output power. Figure 3.10 shows the band diagram for a UTC-PD. Ito and colleagues [67] have been able to maximize the output power of these devices by using impedance matching circuitry. They obtained output powers of 20 mW and 10 mW at 100 GHz and 1 THz respectively, using laser diodes operating at 1.55 μm [40, 82].

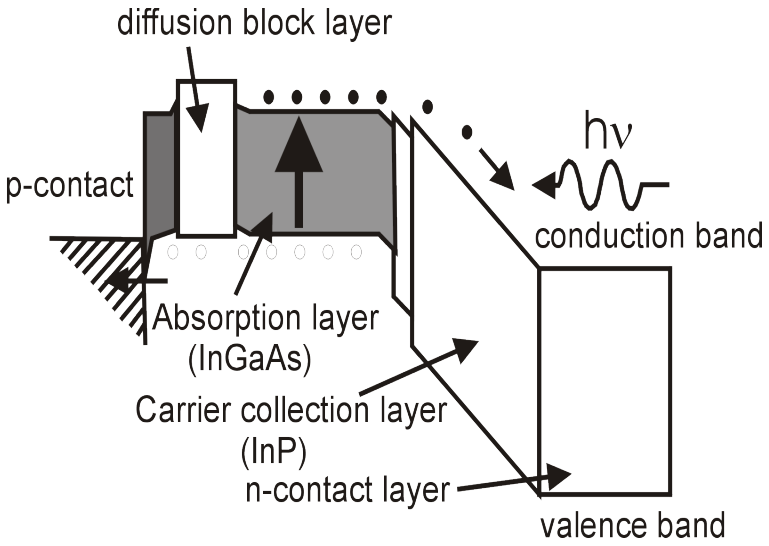

Figure 3.10: Band diagram of a UTC-PD developed by NTT Photonics Laboratories [82]

3.3.3 Photomixers developed by the Millimeter Wave Technology Group at Rutherford Appleton Laboratory

The photomixer design and development work done by the Millimeter Wave Technology (MMT) Group at the Science and Technology Facilities Council (STFC) RAL was begun partly due to the need to provide phase reference and LO sources for each of the 64 antennae of the ALMA telescope [83–85]. ALMA is an international millimeter-wavelength radio telescope under construction in the Atacama Desert of Northern Chile. ALMA will be comprised of a giant array of 12-m antennae, with baselines up to 16 km and state of-the-art receivers that cover all the atmospheric windows up to 1 THz. Construction of ALMA is scheduled for completion in 2013. The motivation behind using photonic LO generation in ALMA is to take advantage of low fibre loss and high performance telecommunication devices to create a remote local oscillator capability. A photonic reference approach has been adopted, in which two 1.55 μm lasers or a 1.55 μm dual laser diode in the frequency range of 27 GHz to 142 GHz is distributed from a central location to each of the 64 antennae that comprise the interferometer. At each receiver there will be a photomixer that will convert the two laser wavelengths to an RF signal, that is then used as a reference to phase-lock a conventional microwave oscillator/multiplier chain. Those interested in more information about this project are referred to the article by Payne *et al.*. [85]. The second driving factor for the photomixer work at RAL has been the general need to provide LO signals for mm-wave heterodyne receivers. It is this goal that has resulted in the development of the photomixer that was purchased by the AIG at the University of Lethbridge [86] hereafter referred to as the MMT photomixer.

The MMT photomixer incorporates a "u^{2}t Photonics" [87] 70 GHz bandwidth InGaAsP telecoms p-i-n photodiode which has a DC responsivity of about 0.5 A/W. Figure 3.11 shows the photodiode supported on a chip of dimensions 2 mm x 0.4 mm x 0.2 mm. A rib waveguide on the surface of the indium phosphide chip is used to couple 1.55 μm optical signals from the cleaved edge of the polarization maintaining fibre (PMF) to the photodiode. The THz output generated by the photodiode is transmitted via a planar gold transmission line, just visible on the left hand end of the InP chip. At the end of the transmission line is a gold on quartz probe that extends across the WR-10 output waveguide and is connected to the output conductor on the photodiode chip by low melting InSn solder or by silver loaded epoxy. A constant voltage bias is applied to the photodiode by means of alternating quarter wave high and low impedance filter sections and the foil probe. Another function for the

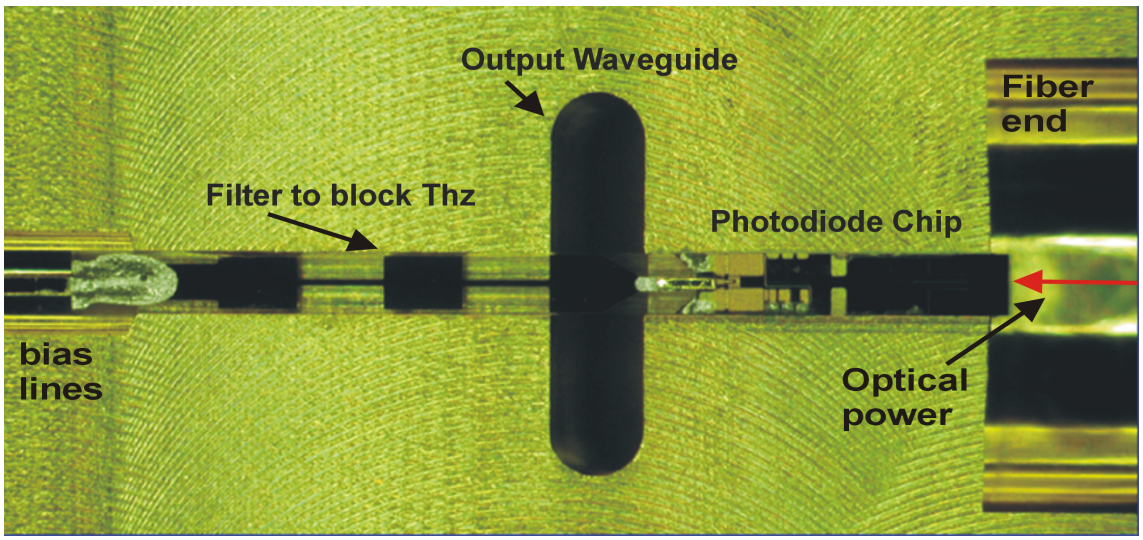

Figure 3.11: Internal view of the MMT Photomixer. The photodiode, center right, generates THz radiation which is coupled to the oval waveguide (with dimensions 2.54 mm x 0.6 mm) by means of a gold on quartz probe. The THz radiation is stopped from propagating along the bias line by the RF filter, left of center.

filter is to prevent the THz radiation from propagating along the bias line. This photomixer generates a power of 10 μW at 250 GHz [88].

3.4 Generation of coherent radiation by photomixing of dual-mode lasers

Up to now the focus has been on photomixing with two independently operated lasers. This requires that the two laser beams be collimated and aligned precisely to achieve good spatial mode matching. The two lasers should also be stabilized independently. This is not an easy task but helps to improve the spectral quality of the radiation generated. The use of the photomixer as a LO source in a heterodyne receiver system for astronomy, where the measured signals very low ($\leq$ pW), requires that the output THz signal be stabilized. It has been proposed and experimentally verified that this problem of optical alignment and stabilization of the beat frequency can be solved by the use of multimode lasers [89–92]. Using dual mode lasers reduces the fluctuation of the difference frequency by the common-mode noise rejection effect [90]. The common mode rejection effect arises due to the fact that the laser modes oscillate in the same cavity and so the direction and frequency shift is the same for all modes present. This means that the resultant difference frequency does not change with mechanical vibrations, temperature and power fluctuations as compared to the laser modes of two independent lasers. Furthermore, it has been shown that the use of pulse-modulated multimode laser diodes (MLDs) enhances the THz photomixing efficiency [91]. With two laser diodes we get a single beat frequency, but with a multimode laser diode, we get multiple beat frequencies due to the multiplicity of the laser modes. This results

in multiple modes of THz radiation. Tani *et al.*. [90] have demonstrated photomixing with a dual-mode microchip laser, a monolithic dual-mode Distributed Bragg Reflector (DBR) laser diode (LD) and a tunable dual-mode external cavity LD.

3.5 Prospects of increasing output power from a photomixer

The various photomixer and antenna designs discussed in this Chapter have led to an improvement of the THz output power. It is important to note, however, that the optical-THz conversion efficiency, (P_{THz}/P_{opt}), in the frequency range of 1 THz to 3 THz is quite low ($\sim 10^{-5}$ - 10^{-6}). There are two possible explanations to this; only a small fraction of the photocurrent contributes to the THz radiation and/or a lot of power is being lost in the THz optics. Equation (2.16) shows that the maximum output THz power is quadratically dependent on the quantum efficiency, η. Its clear that in order to increase the output THz power, new photomixer designs with high quantum efficiencies are required. Table 3.1 shows comparison of the state-of-the-art photomixer designs in terms of their output power and operation frequency.

Table 3.1: A comparison of the state-of-the-art photomixer designs.

Photomixer	Antenna	Frequency (THz)	Output power (μW)	Year reported
p-i-n photodiode	Bow-tie	0.25	10	2004 [88]
Travelling Wave Photomixer	Bow-tie	850	2.64	2006 [93]
Unitraveling Carrier p-i-n Photodiode	Log-periodic	1.04	2.6	2005 [40]
LTG-GaAs photoconductor	Log-periodic	1	1	2003 [58]
Superlattice staked p-i-n diodes	Log-periodic	0.4	1	2007 [94]
Travelling Wave Photomixer	Log-periodic	3	0.1	1999 [43]

3.6 Conclusions

In this Chapter various THz antennae and photomixer designs have been described. The UTC-PD has been described as the most promising photomixer design. The MMT photomixer has also been described. Despite much effort being put into increasing THz power output from parametric sources and photomixers, the output power from these sources still remains low and inadequate for most applications. Some researchers now believe that photomixers have reached their theoretical limit and so it is no longer possible to further increase the output THz power. The following Chapter will describe the equipment that I used and automated to evaluate the performance of the MMT photomixer.

Chapter 4

Experimental Configuration and Automation

4.1 Overview

In the previous Chapters, various photomixer designs and their limitations were discussed. The main points to note are that the output power and frequency of the photomixer are dependent on the bias voltage, and the laser power and beat frequency of the two lasers incident on the photoconductor or photodiode active region. Also, the power and individual frequencies of the two input tunable lasers and hence their difference frequencies are controlled by tuning the current flowing through each laser diode and the laser diode temperature. Care must be taken not to exceed the current damage threshold of the photomixer. The number of parameters required to be tuned to operate the photomixer coupled with the delicacy of the device create challenges for its manual operation. This Chapter de-

scribes the experimental configuration and software programs that were used to automate the photomixer.

4.2 Experimental configuration for photomixing

A block diagram of the experimental configuration used in the manual operation of the photomixer is shown in Figure 4.1. The laser diode controller is shown connected to the laser diodes. The output from the laser diodes is coupled into polarization maintaining fibre (PMF) and mixed by the 2x2 50:50 fiber coupler. One output from the fiber coupler goes to the photomixer while the other is connected to the optical spectrum analyzer. The bias box provides the reverse bias voltage required by the photomixer. The THz output radiation from the photomixer is focused to the input of the FTS which is controlled by Aerotech's Soloist single axis motion controller [95]. A cryogenic detector which is synchronized with the FTS is placed at one of the outputs of the FTS. A detailed description of the University of Lethbridge Astronomical Instrumentation Group (AIG)'s FTS used in this thesis will be presented in sections that follow.

Figure 4.2 shows a photograph of the complete set-up used in this thesis. The dual laser source is shown on top of the laser diode controller (LDC) which is also on top of the optical spectrum analyzer (OSA). The PMFs running from the dual laser source are shown in blue. Besides the OSA there is a bias box, placed on top of the National Instruments (NI) Data Aquisition (DAQ) device (NI USB-6255). The DAQ is not shown in Figure 4.1 because it was only used for the automatic configuration. The photomixer is also shown on the FTS optical bench. Figure 4.3 shows a close-up image of the MMT photomixer. The optical

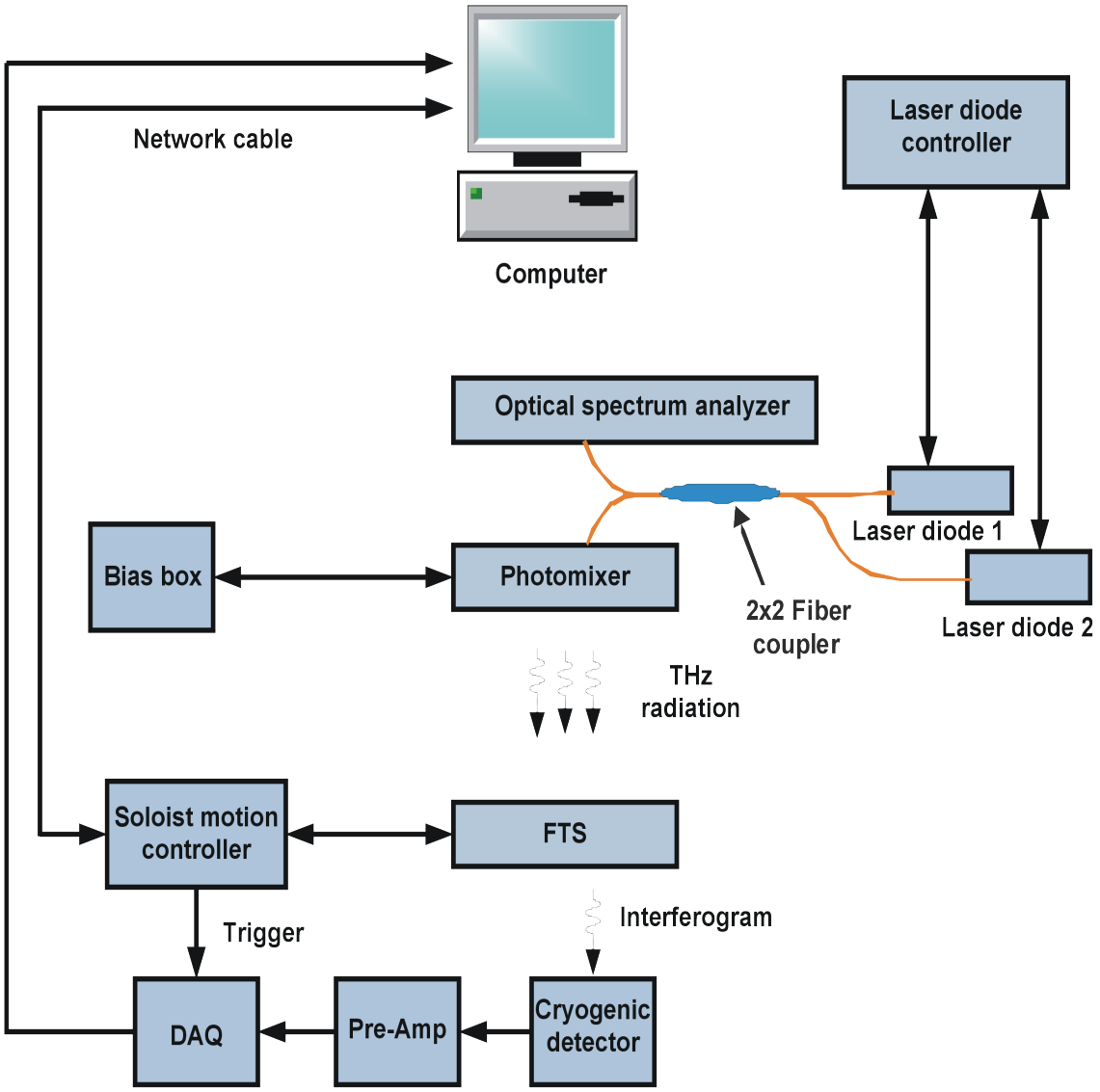

Figure 4.1: A block diagram of the experimental configuration used in the manual operation of the photomixer. A ILX Lightwave LDC-3900 Modular laser diode controller was used together with Fitel FOL 15CWD-19300-SNL DFB laser modules. An Advantest Q8384 optical spectrum analyzer was used in the measurement of optical signals.

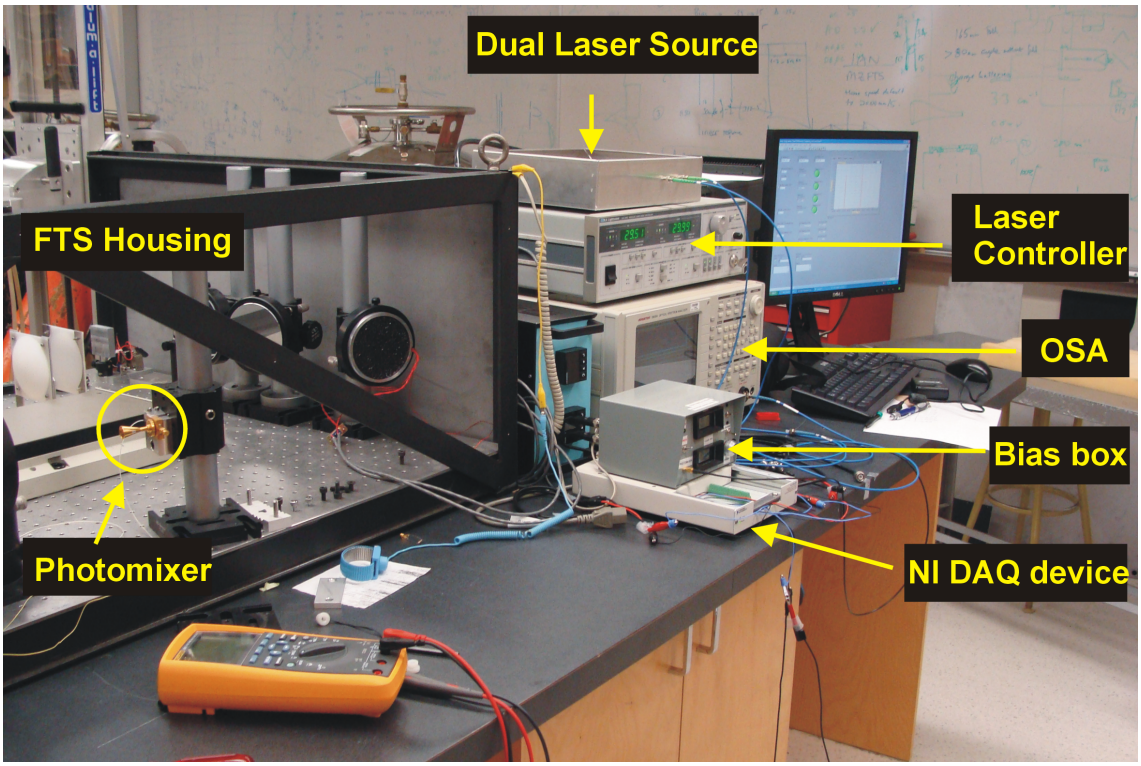

Figure 4.2: A photograph of the equipment used in characterizing the photomixer: solid state lasers driven by the laser controller, Optical Spectrum Analyzer (OSA), Bias voltage box, LabVIEW Data Aquisition Device (DAQ), Fourier Transform Spectrometer (FTS). All the instruments are interfaced to a computer that runs LabVIEW using the IEEE General Purpose Interface Bus (GPIB). The photomixer is also shown mounted to the FTS optical bench at one of the inputs.

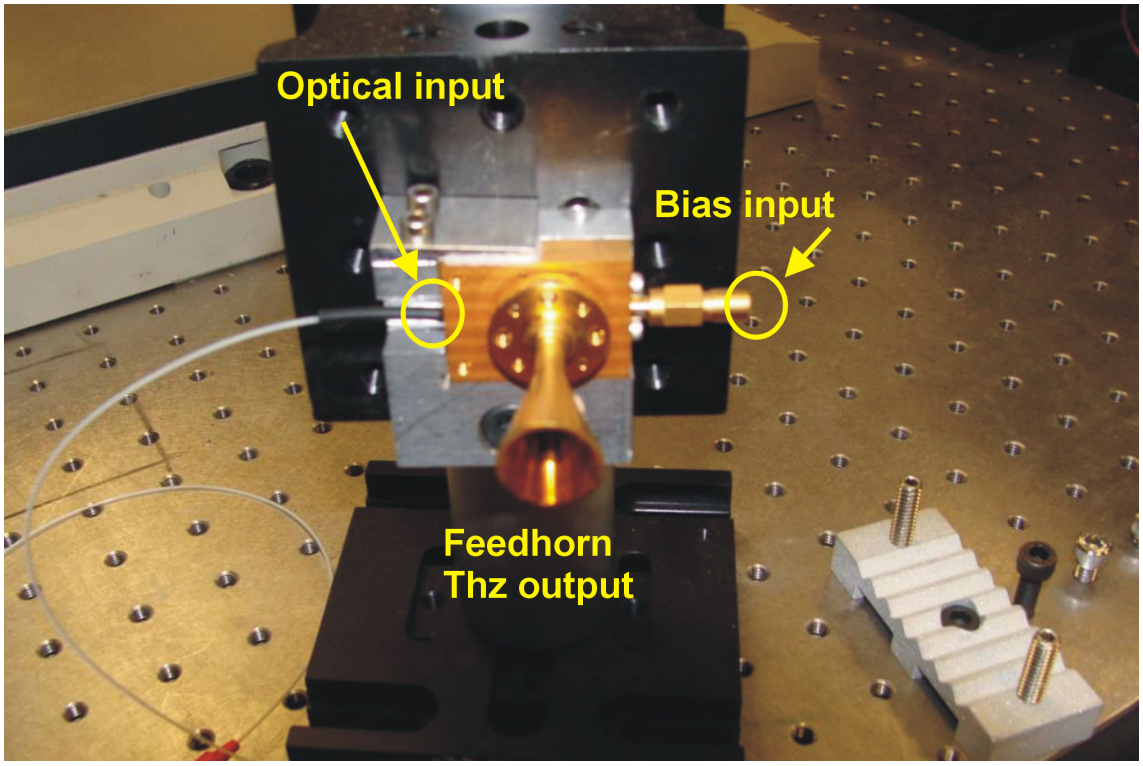

Figure 4.3: A close-up of the photomixer showing the fibre used for optical input, the bias input and the feedhorn.

power is applied to the active region of the photomixer through the PMF pigtail shown. The inlet for the bias voltage is also shown. The feedhorn shown couples the generated THz output out of the device to free space. The various sections of the measurement configuration will now be discussed in detail.

4.3 Generation of THz beat signals

It has been stated in the previous Chapters that photomixing requires the generation of a THz beat frequency from two laser diodes. It is therefore important to analyze how the beat frequency was generated. Figure 4.4 shows the configuration used to mix the two

laser frequencies from the laser diodes. The output of two 1.55 μm lasers having powers, P_1 and P_2 and wavelengths λ_1 and λ_1, respectively are fed into fibres and mixed with a 50:50 2x2 fibre coupler. One output of the coupler connects to the photomixer while the other connects to the optical spectrum analyzer (OSA) which measures the difference frequency and total laser power.

The efficiency of photomixing is maximized when there is good spatial mode matching of the laser beams and so it is necessary to collimate and align the two laser beams precisely. This is done in the fiber coupler.

Figure 4.5 shows a photograph of the experimental configuration just described. The laser diodes are driven by a laser diode controller LDC by varying the current and temperature. The 1550 nm laser signals are then coupled into polarization maintaining

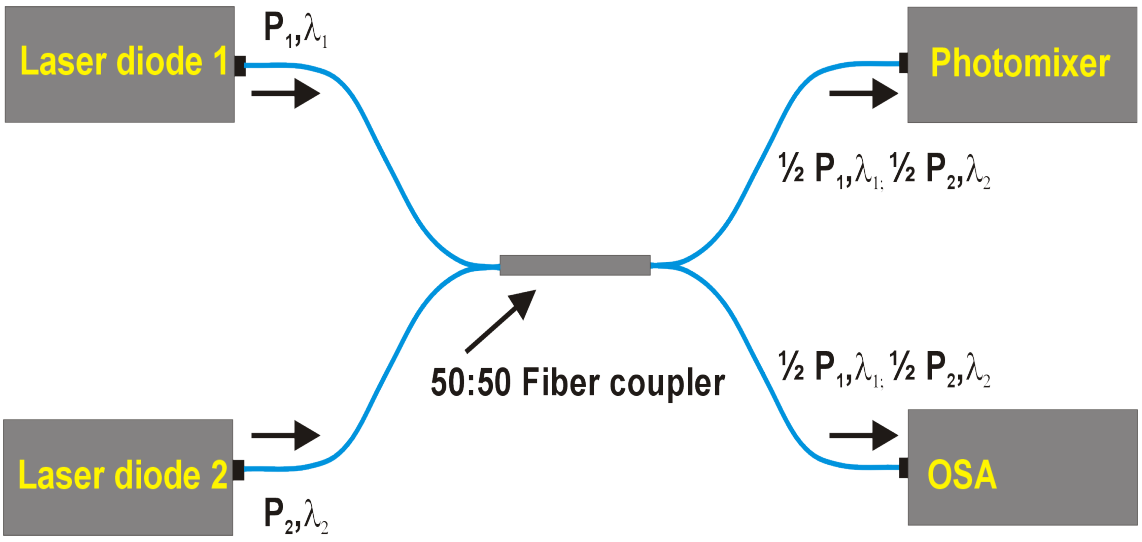

Figure 4.4: The photomixing arrangement used for THz generation. The two lasers are driven by a laser diode controller (LDC) and so the laser difference frequency and therefore the output frequency can be varied. A 50:50 fiber coupler, often referred to as a 3 dB coupler splits the input signal in half.

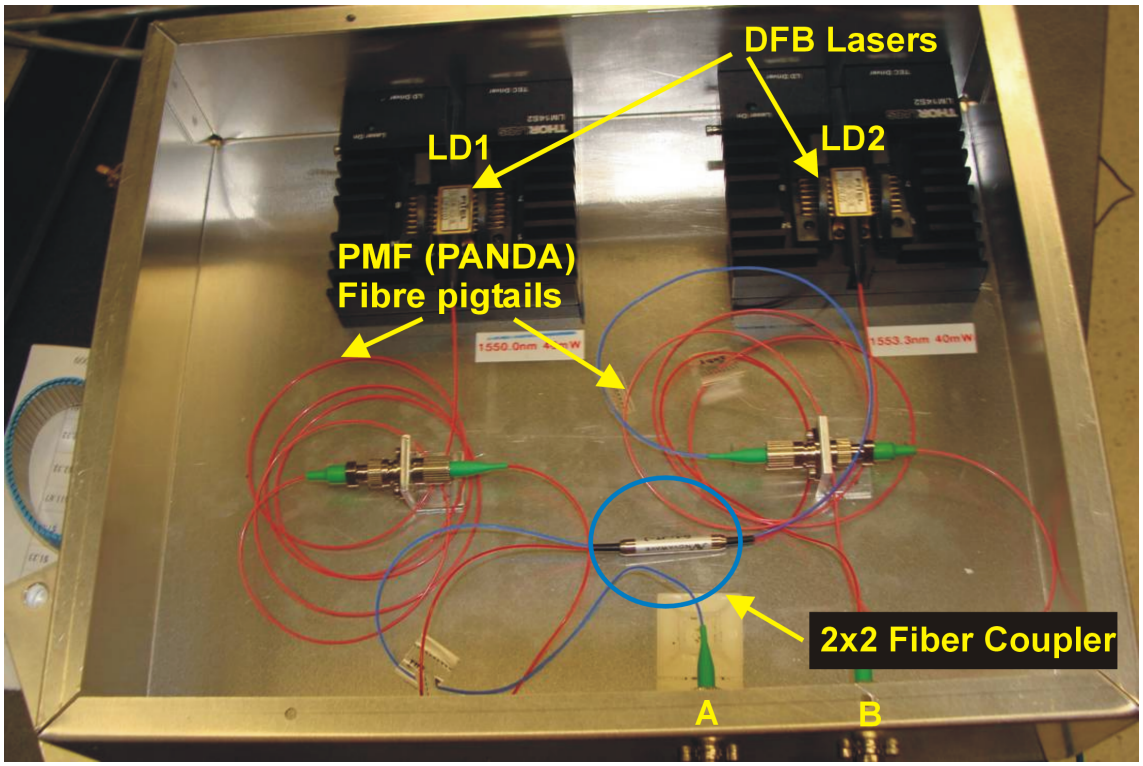

Figure 4.5: A photograph of the DFB lasers whose output is combined using a 50:50 2x2 fiber coupler. The diode lasers are mounted on the black heat sinks towards the top of the box. The two outputs are at the lower edge of the box and are labeled A and B. LD1 and LD2 have center wavelengths of 1550.0 nm and 1553.3 nm respectively and both produce maximum powers of 40 mW.

fibers PMFs and mixed in the 50:50 fiber coupler (circled in blue). One of the outputs from the coupler is connected to the photomixer and the other to the OSA. The use of PMFs ensures that the polarization state of the laser beams does not rotate as the beam propagates through the fibre. This reduces the variation of the optical power and hence the noise in the measured THz signal. The joining of the fibres is done using angle polished connectors (APC) which ensure that there is minimal back-reflection of the beam at the fibre/air interface.

4.4 The Bias Box

The control of the bias voltage to the photomixer is very critical. Certain current limits have to be adhered to in order to protect the photomixer from damage. The bias box used in this thesis was designed and built by Gregory Tompkins who is the AIG's electronics technician. Figure 4.6 shows the circuit diagram for the bias box. It is based on the Basic Howland Current Pump and can supply bi-directional current. The current limits are +1.0 mA at a maximum voltage of +0.6 V and -5.0 mA at a minimum voltage of -2.5 V. These limits are monitored by dual limit window comparators which trigger a latched solid state relay in the case of an overstress. This then shorts the photomixer bias voltage. When in manual operation the current is supplied to the photomixer from the bias box front panel mounted potentiometer which operates on two 6V/1A batteries. For remote operation the current is supplied from an external DAQ device through the bias box. A switch at the back of the bias box enables one to select the current source.

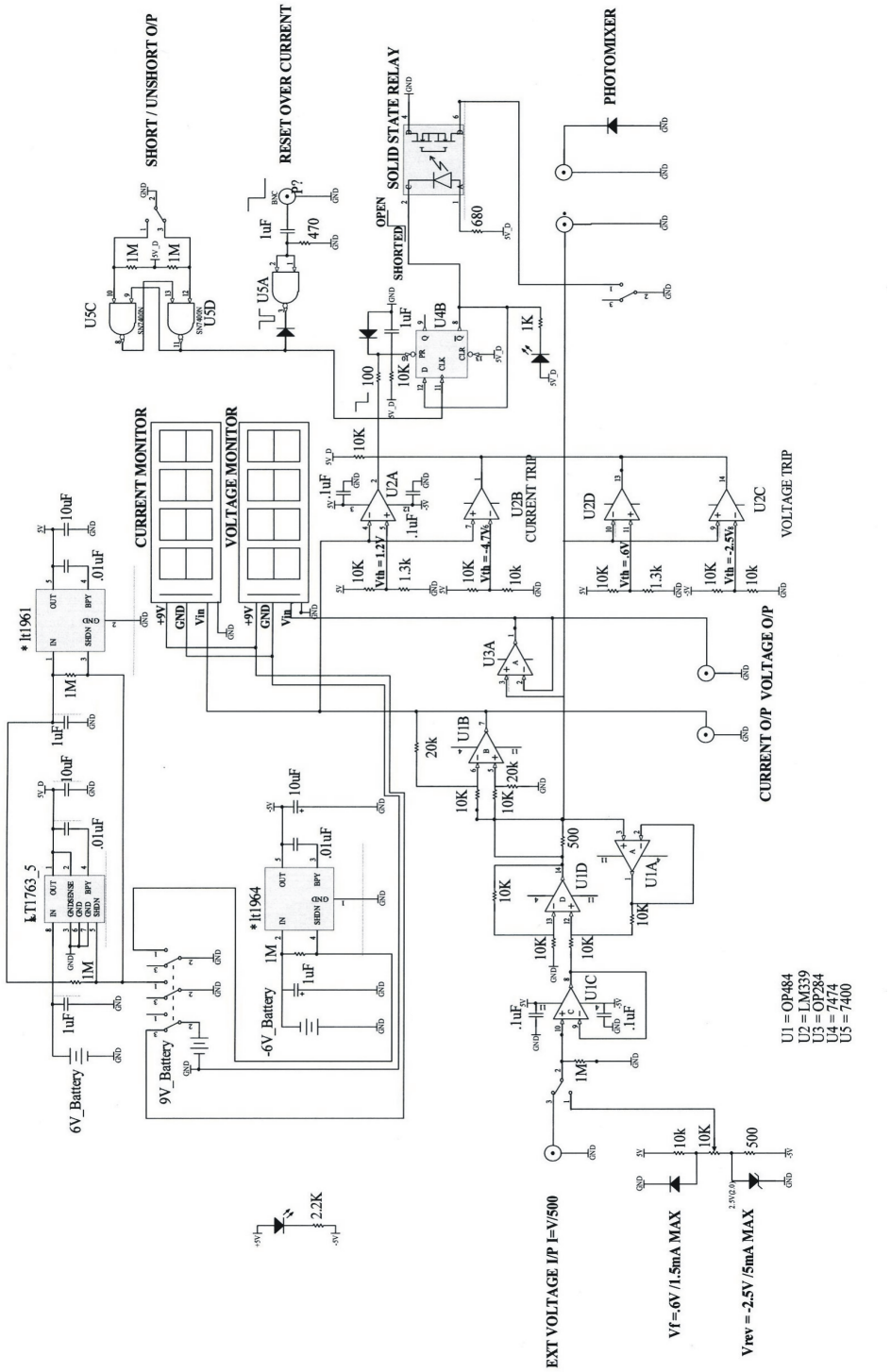

Figure 4.6: The electronic circuit diagram of the bias box.

Two liquid crystal displays (LCDs) with 4-1/2 digit analog-to-digital (A/D) read-outs are used to display the measured photocurrent and bias voltage. The photomixer current and voltage can also be remotely measured by use of 2 buffered BNC outputs on the bias box.

4.5 The Fourier Transform Spectrometer (FTS)

The radiation from the photomixer is measured using the FTS which is of the Mach-Zehnder type [96]. In principle, this configuration leads to an increase in efficiency from 50 % to 100% in comparison with a Michelson interferometer [97], however, in the experimental configuration used in this thesis, where only one detector is used, the efficiency is the same. The block diagram of the FTS is shown in Figure 4.7. As is shown in the diagram, the FTS has two input ports (labeled A and B) and two output ports (labeled 1 and 2), which can be accessed independently. Input port A is where a spectrometer calibration source is positioned and input port B is the port viewing the source of THz radiation to be measured. This FTS design uses two 50:50 beamsplitters labeled BS1 and BS2 respectively, and it makes use of the double reflecting corner cube mirrors. At the output of the FTS are two output ports where detectors are positioned. In front of the detectors are filters for the respective measurement wavelength bands.

4.6 Detectors

The THz power output from the MMT photomixer is estimated to be 10 μW at 300 GHz and as previously shown it falls as the fourth power of frequency. This is lower

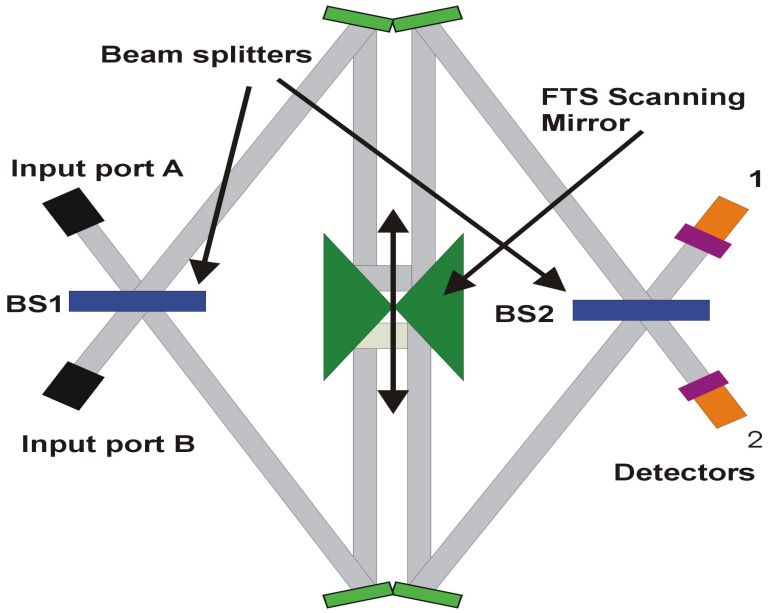

Figure 4.7: Block diagram of the Mach-Zehnder FTS.

than the limit of room temperature detectors and therefore we need a cryogenic system. The noise level in the measured signal must be very low, a condition that can only be met by the use of cryogenic detectors. The most common detectors in use for this purpose are Ge bolometers operating at 300 mK [52]. These Helium-3 cooled bolometers have a typical noise equivalent power (NEP) of about 1.5×10^{-15} W/Hz$^{1/2}$ [98]. During measurements, a 450 μm filter was put in front of the detector since the output THz frequency from the photomixer falls in the range of 150 to 610 GHz. This thesis will not provide a detailed description of the Ge bolometers. For a detailed description, readers are advised to read the work of the AIG's previous graduate students Brad Gom [98] and Locke Spencer [99].

4.7 FTS Data Analysis

The FTS described in Section 4.5 uses the principle of interferometry. Incident radiation enters the FTS through one of the input ports (A or B). The beam splitter BS1 separates the radiation into two beams that travel different optical paths before recombining at BS2. The optical path distance (OPD) which is the difference between the two beam path lengths in an interferometer can be changed by moving the FTS scanning mirror with a constant velocity. This creates an interferogram of signal versus OPD. The interferogram is a Fourier transform of the source spectrum. In order to obtain the spectrum as a function of frequency, the inverse Fourier transform of the interferogram is computed.

The THz radiation output from the photomixer can be considered a monochromatic beam of frequency σ_0. If this beam is incident on the beamsplitter, BS1, it is divided into two beams described by their electric fields as [99]

$$\begin{aligned} E_1(z_1,t) &= E_0 r' e^{i\rho} r_m e^{i2\pi(\sigma_0 z_1 - \nu t)} t' e^{i\tau} \quad [\mathrm{Vm}^{-1}] \\ E_1(z_1,t) &= E_0 t' e^{i\rho} r_m e^{i2\pi(\sigma_0 z_2 - \nu t)} r' e^{i\tau} \quad [\mathrm{Vm}^{-1}] \end{aligned} , \tag{4.1}$$

where: E_0 is the amplitude of the incident electromagnetic wave of angular frequency $\omega = 2\pi\sigma_0$, σ_0 is the wavenumber in cm^{-1}, $r'e^{i\rho}$ is the beamsplitter reflection, $t'e^{i\tau}$ is the beamsplitter transmission, r_m is the amplitude reflection coefficient of each mirror, z_1 and z_2 are the optical path lengths traveled by the two beams respectively. Adding the two individual electric fields from Equation (4.1) gives the total electric field. The total intensity known as the interferogram measured by a detector placed at the output of the FTS is obtained by squaring the total electric field [100]

$$I_0(z) = c\epsilon_0 E_0^2 R_m R_b T A\Omega[1+\cos(2\pi\sigma_0 z)] \quad [\mathrm{Wm}^{-2}\mathrm{sr}^{-1}\mathrm{cm}^{-1}] , \tag{4.2}$$

where $R_m = r_m^2$ is the intensity reflection coefficient of the mirrors, $R_b = r'^2$ and $T = t'^2$ are the intensity reflection and transmission coefficients of the beamsplitter, respectively, c is the speed of light, ϵ_0 is the permittivity of free space, $z = z_1 - z_2$ is the OPD. $A\Omega$ is the throughput. In an ideal interferometer, the beamsplitter reflects and transmits 50 % of the incident radiation, and the mirrors are perfect reflectors. Considering only the modulated term, the interferogram can be written as:

$$I_0(z) = R_m R_b T B(\sigma_0) \cos(2\pi\sigma_0 z) \quad [\mathrm{Wm}^{-2}] \,, \tag{4.3}$$

where $E_0^2 = B(\sigma_0)$ is the spectrum.

Figure 4.8 shows a portion of an interferogram obtained from the RAL photomixer using the University of Lethbridge FTS. The negative voltages are due to the fact that the measurements were done with an AC coupled detector without a dc component. A subsection of the Fourier transform of the interferogram is shown in Figure 4.9. This is the THz output spectrum of the photomixer. The peak of the signal is at 350 GHz (11.96 $\pm$ 0.06 cm^{-1}). The equally spaced harmonics shown are most likely due to the stage not being in uniform motion. They may also be due to nonlinearities in the detector.

4.8 Automation

The operation of the difference frequency THz system requires one to control the laser diode current and temperature, and the reverse bias voltage. Moreover, the photomixer is an extremely fragile device that can easily be destroyed. Initially, one would control everything manually (Figure 4.1) and often in the final stages of increasing the power, the bias box would trip. This was a tedious process. It was clear from the start that to do

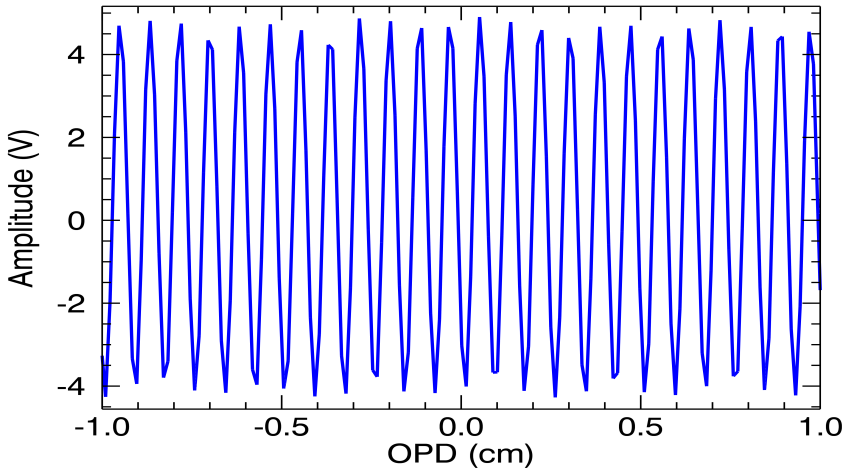

Figure 4.8: Part of the measured interferogram when the photomixer was illuminated with lasers having a difference frequency of 11.96 cm^{-1}. The photomixer active region was biased at -2.45 V and the gain of the detector amplifier was set at 10.

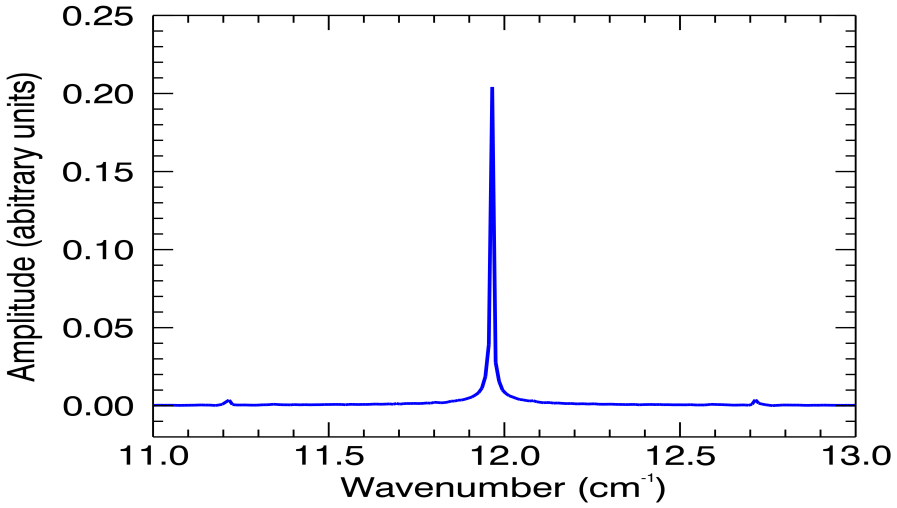

Figure 4.9: The spectrum of the photomixer when illuminated with lasers having a difference frequency of 11.96 cm^{-1}. The photomixer active region was biased at -2.45 V. The equally spaced harmonics shown are probably due to the stage being not in uniform motion or due to nonlinearities in the detector.

this in any thoughtful and comprehensive way, the process had to be computer controlled. In this thesis, the automation was done using the National Instruments NI Inc LabVIEW software. Figure 4.10 shows the block diagram of the experimental configuration used in the automatic operation of the photomixer. The laser diode controller and the optical spectrum analyzer can now be seen connected to the computer using the General Purpose Interface Bus (GPIB). The bias box is also connected to the computer through the NI DAQ.

Figure 4.11 shows a flowchart of the labVIEW program used to characterize the laser diodes. The flowchart was modified depending on what needed to be measured. The main objective of carrying out this project was to automate the measurement system. Figure 4.12 shows a flowchart of the main LabVIEW program used to drive the photomixer. A screen shot of the program Graphical User Interface (GUI) is shown in Figure 4.13. The program allows one to enter the required difference frequency and combined optical power. Calculation of the combined power of the laser diodes is direct and does not require the user to fix any of the parameters. Calculation of the difference frequency requires knowledge of the laser diode frequency ranges as will be discussed in Chapter 5.2 and so the user is required to enter one of the laser diode temperatures. As for the optical spectrum analyzer, values for the three parameters required, that is the resolution, the start and stop scan wavelengths, are always set at their default values which can easily be changed. The LabVIEW programs were successfully run several times to find out if they gave consistent values before connecting the optical power to the photomixer. Figure 4.13 shows that the measured values are very close to those requested.

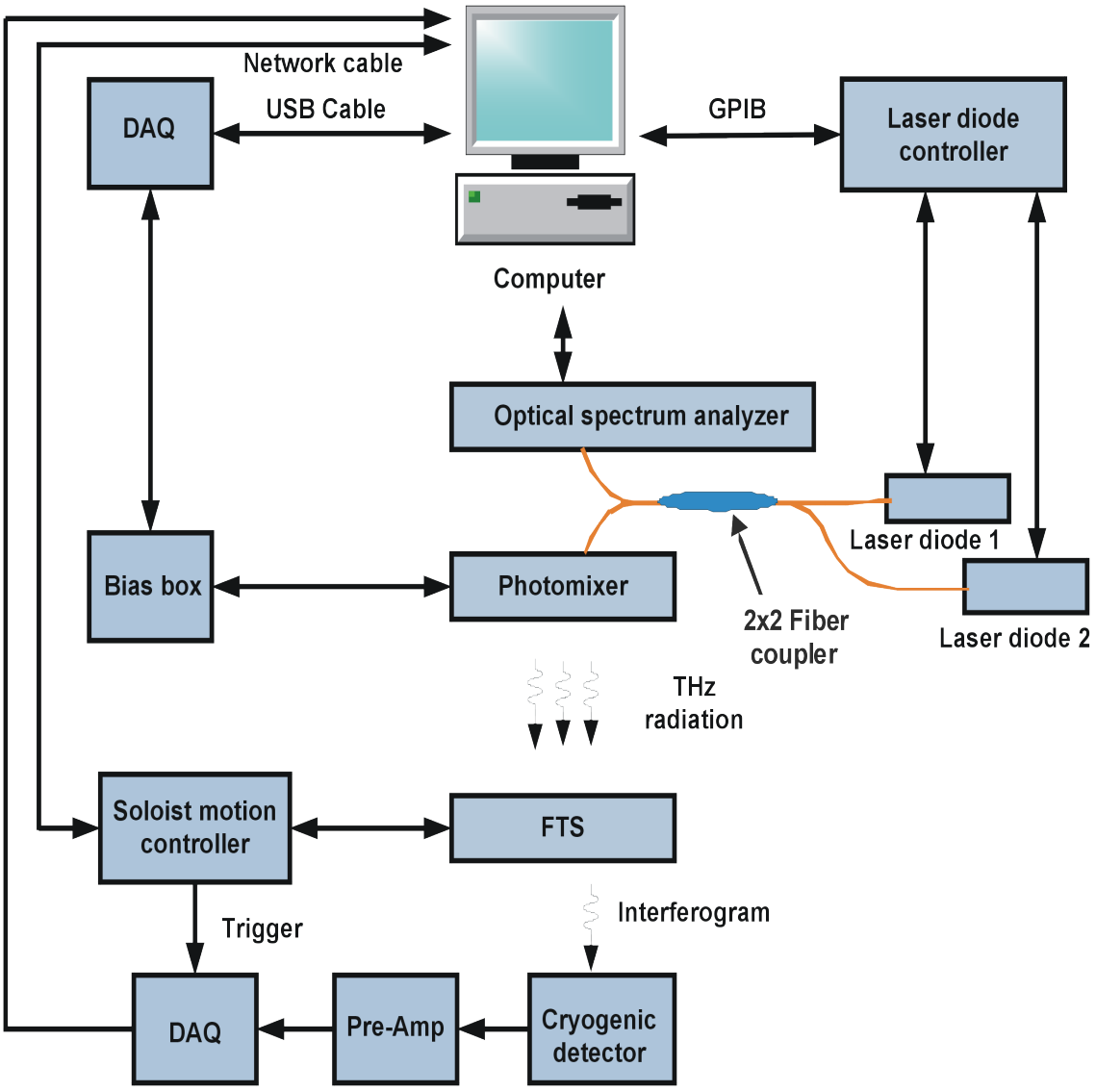

Figure 4.10: A block diagram of the experimental configuration used in the automatic operation of the photomixer.

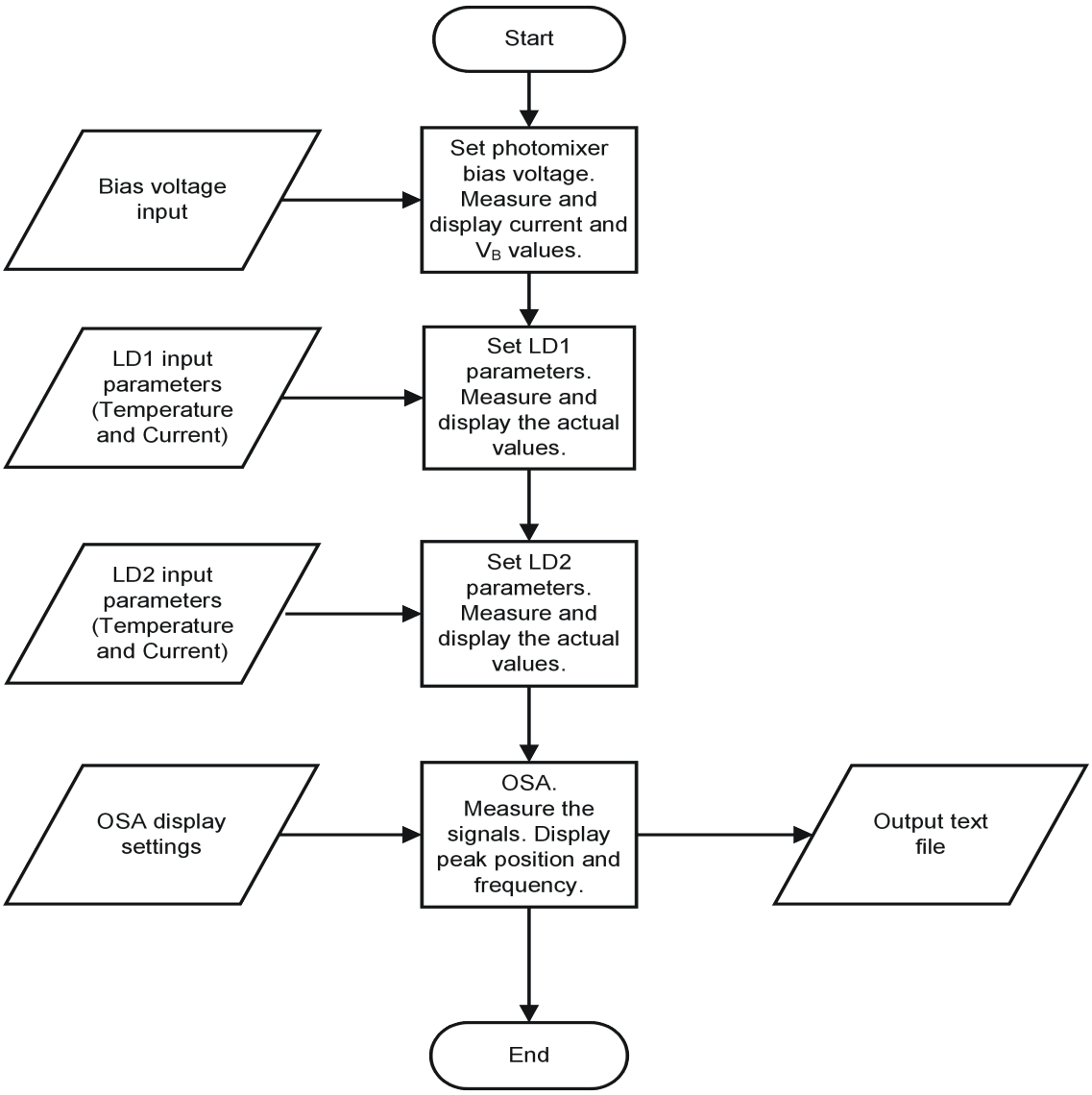

Figure 4.11: The flowchat for the LabVIEW program used to characterize the laser diodes and the photomixer.

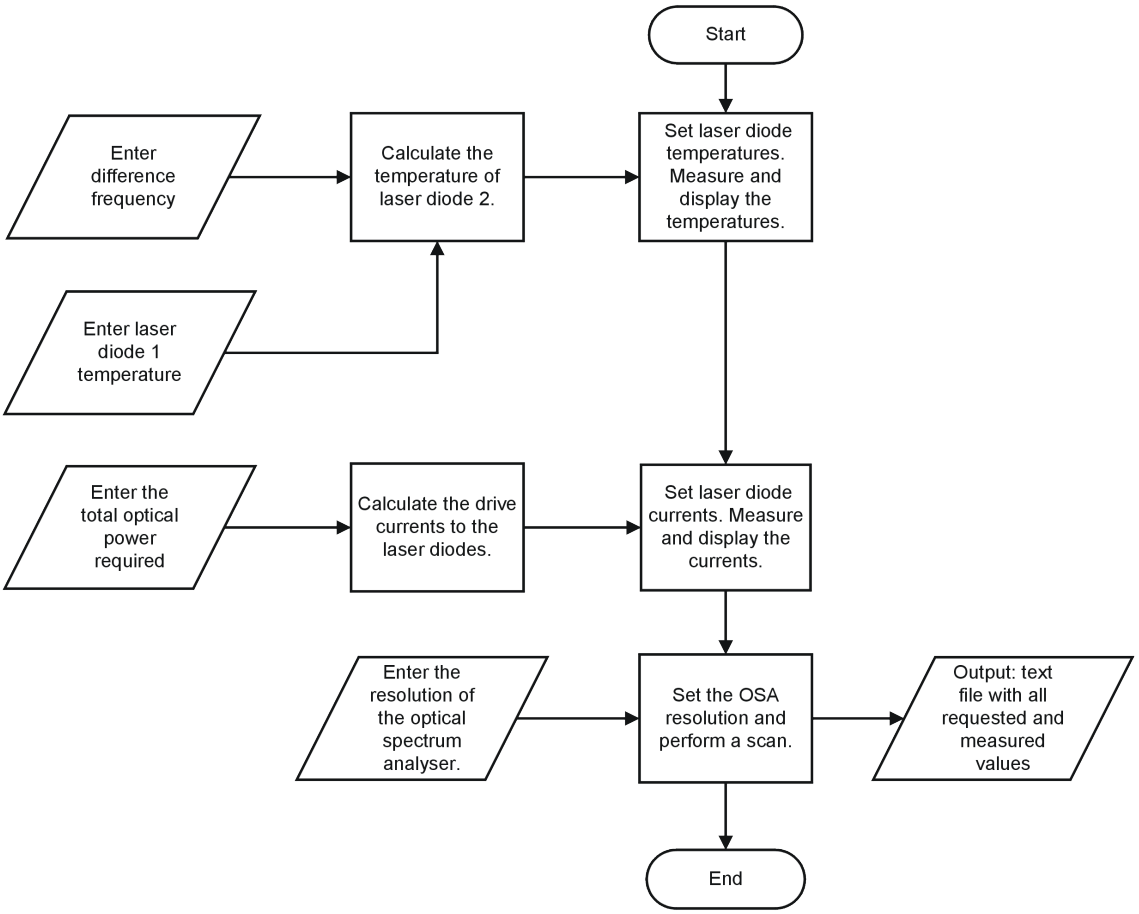

Figure 4.12: The flowchat for the main LabVIEW program used to control the experimental configuration. The user has to input the required difference frequency, total laser power and laser diode 1 temperature and the program will adjust the other parameters accordingly.

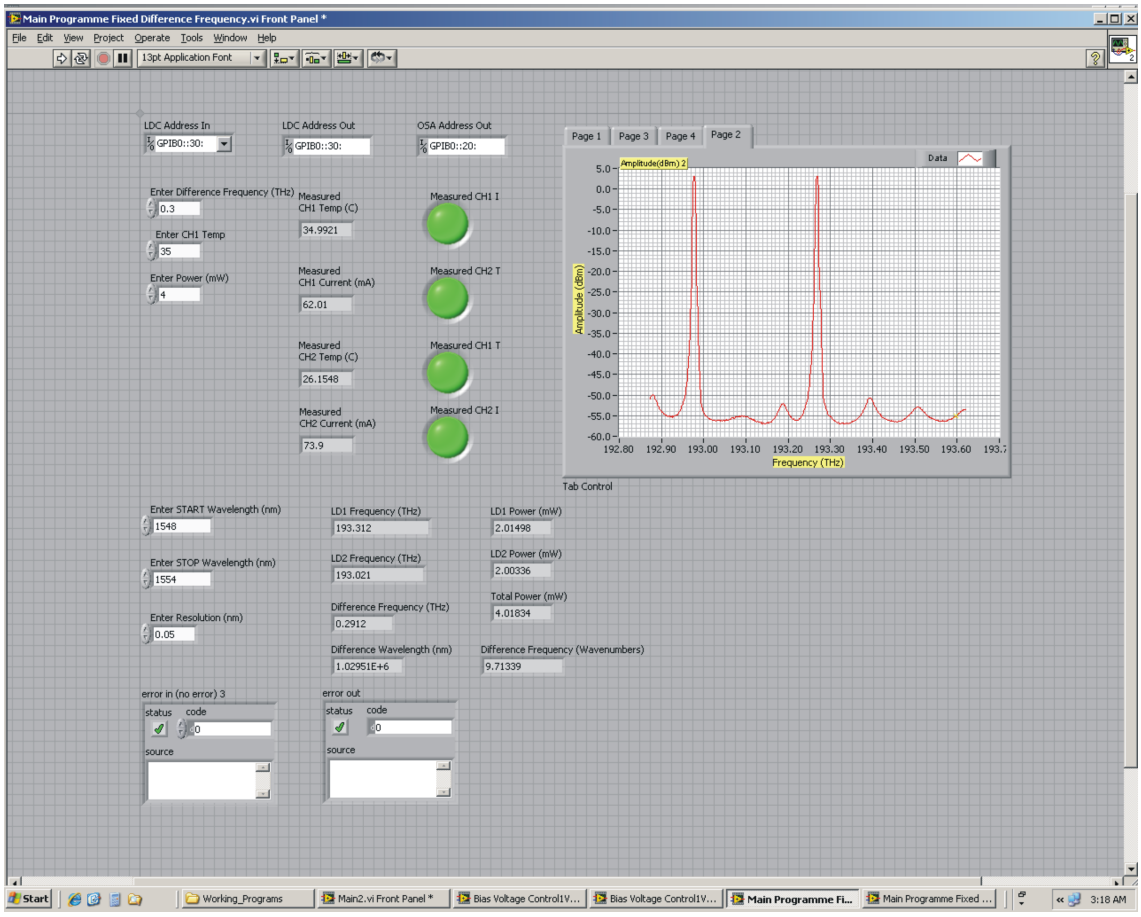

Figure 4.13: The front panel of the LabVIEW program that controls the laser diodes and the Optical Spectrum Analyzer.

4.9 Conclusions

In this Chapter, the experimental configurations and the LabVIEW programs used in this thesis were discussed. The photomixer was successfully automated taking into account the limits for the various parameters. The diode curves taken throughout the measurement process indicate that the photomixer has not been damaged. The results from the characterization of the laser diodes and the photomixer will be presented in Chapter 5.

Chapter 5

Characterization of the Photomixer

5.1 Overview

This Chapter presents the main results obtained using the experimental configurations described in Chapter 4. A discussion of the results obtained from the characterization of the laser diodes is presented in Section 5.2. The V-I characteristics of the photomixer are presented in Section 5.3. Section 5.4 presents the FTS and detector settings that were used in the measurement of the photomixer output THz signal. The rest of the Chapter discusses results from the measurements of the photomixer THz output. Because of the multi-dimensional nature of the tests, automation was essential and so most of the results were obtained using the LabVIEW programs discussed in Chapter 4 which controlled all the apparatus.

5.2 Laser Diode Characteristics

In this work, it is essential to understand the laser diode characteristics in order to determine the dependence of the laser frequency and power on the laser diode temperature and drive current. The automation of the control of the device is dependent on these parameters. Figure 5.1 shows the optical spectrum analyzer (OSA) display of the optical signals from the two laser diodes. The temperatures of the two LDs were all set at 35 ^{0}C. LD1 was driven by a current of 88 mA generating a maximum laser power of 2.907 $\pm$ 0.003

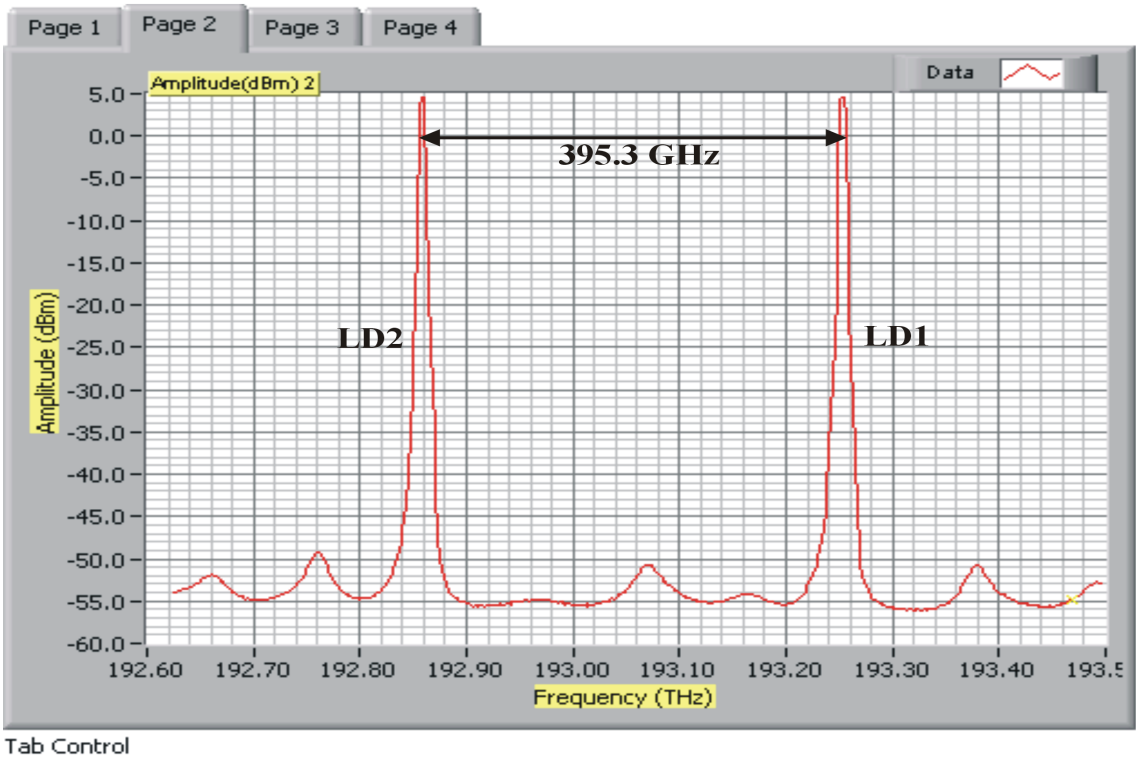

Figure 5.1: Optical signals from the two laser diodes having a difference frequency of 395.3 GHz. All LDs were operated at 35 ^{0}C. LD1 was driven with 88 mA generating a maximum power of 2.907 mW (4.63 dBm) at a wavelength of 1550.94 nm (193.296 THz). LD2 was driven with 100 mA generating a maximum power of 2.916 mW (4.65 dBm) at a wavelength of 1554.12 nm (192.901 THz). The total power as measured from output A was 5.82 mW.

mW (4.63 dBm) at a wavelength of 1550.94 nm (193.296 THz). LD2 was driven by a current of 100 mA generating a maximum power of 2.916 ± 0.003 mW (4.65 dBm) at a wavelength of 1554.12 nm (192.901 THz). The total power was 5.82 mW and the difference frequency was 395.3 GHz. The difference in drive currents is to ensure that the output powers from the two laser diodes are matched because that optimizes the efficiency of the photomixer. The reason why the two diodes gave different powers when driven by the same current could be that the laser diodes themselves have different efficiencies or that the fiber coupling ratio was not 50:50. The error in the measurement of frequency was insignificant as repeated scans obtained by fixing other parameters resulted in the same frequency values.

As is explained in Chapter 4, the tuning of the LDs is done by a combination of temperature (coarse) and drive current (fine). Figure 5.2 shows that the frequency of LD1 can be tuned from 193.327 THz (at 35 ^{0}C) to 193.559 THz (at 15 ^{0}C). The frequency of LD2 can be tuned continuously from 192.907 THz (at 35 ^{0}C) to 193.141 THz (at 35 ^{0}C). These graphs were obtained by tuning the temperature of each of the LDs when driven by the lower limit current of 20 mA (red lines) and the upper limit current of 90 mA (blue lines). This allows one to tune the difference frequency from 193.327-193.141 = 0.251 THz to 193.559 - 192.907 = 0.652 THz. It is noted that the slope for LD1 changes from -0.01160 to -0.01181 THz/^{0}C when the drive current is varied from 20 to 90 mA. That for LD2 changes from -0.01158 to -0.01172 THz/^{0}C when the drive current is varied in the same range. The error in all slopes was ± 0.00002 THz/^{0}C (i.e $<$ 0.2 %). In order to make sure that the laser diodes can be tuned to give the required difference frequencies, one has to put careful thought into deciding the frequency ranges of the laser diodes before purchasing them.

Figure 5.3 shows that the laser power also changes with LD temperature. The graphs are not linear, making it difficult to keep the laser power constant during these measurements. The change in power for both LDs is approximately 0.18 mW when driven by a current of 20 mA but increases to about 0.4 mW when driven by a current of 90 mA. These changes were considered second order effects and were not taken into account in the LabVIEW programs described in Section 4.6.

It is tempting to assume that the laser powers from the two outputs (Figure 4.2)

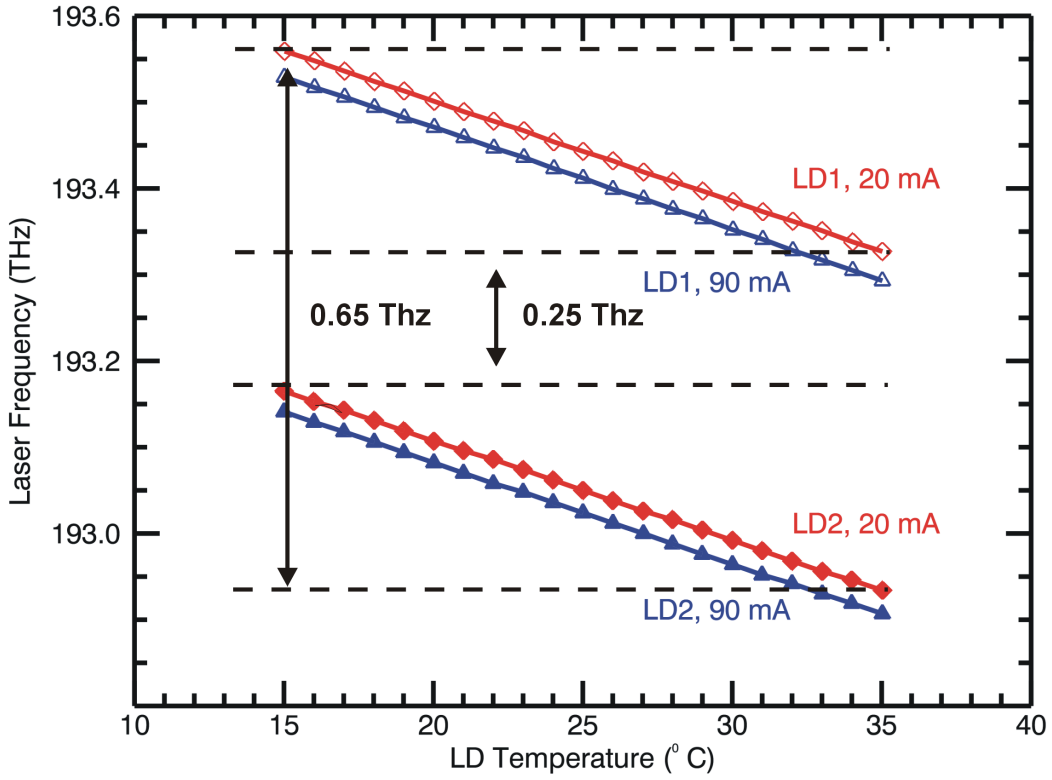

Figure 5.2: The variation of laser frequency with temperature for LD1 and LD2. The LDs were driven by currents of 20 mA (red) and 90 mA (blue). Error bars are insignificant.

of the PMF fiber coupler are the same since the coupler is labeled as having a splitting ratio of 50:50 by the manufacturer. Figure 5.4 shows that the laser signals from the two outputs of the coupler have different powers, i.e. the power measured by the OSA is significantly different to that which goes to the photomixer. This is of potential concern because of the damage threshold of the photomixer which must be taken into account. Care must be taken to make sure that the photomixer is connected to Output B of the fibre coupler which has the least power.

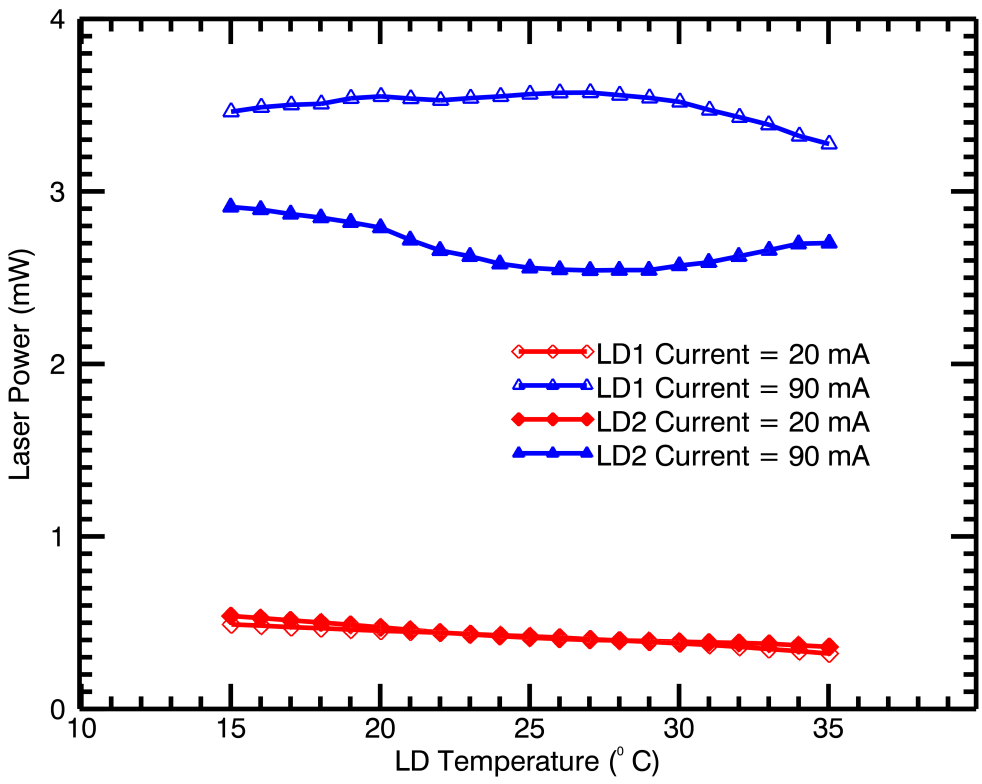

Figure 5.3: The variation of laser power with temperature. The reading were obtained when the drive current for the LDs was set to 20 mA (red) and 90 mA (blue). Error bars are insignificant.

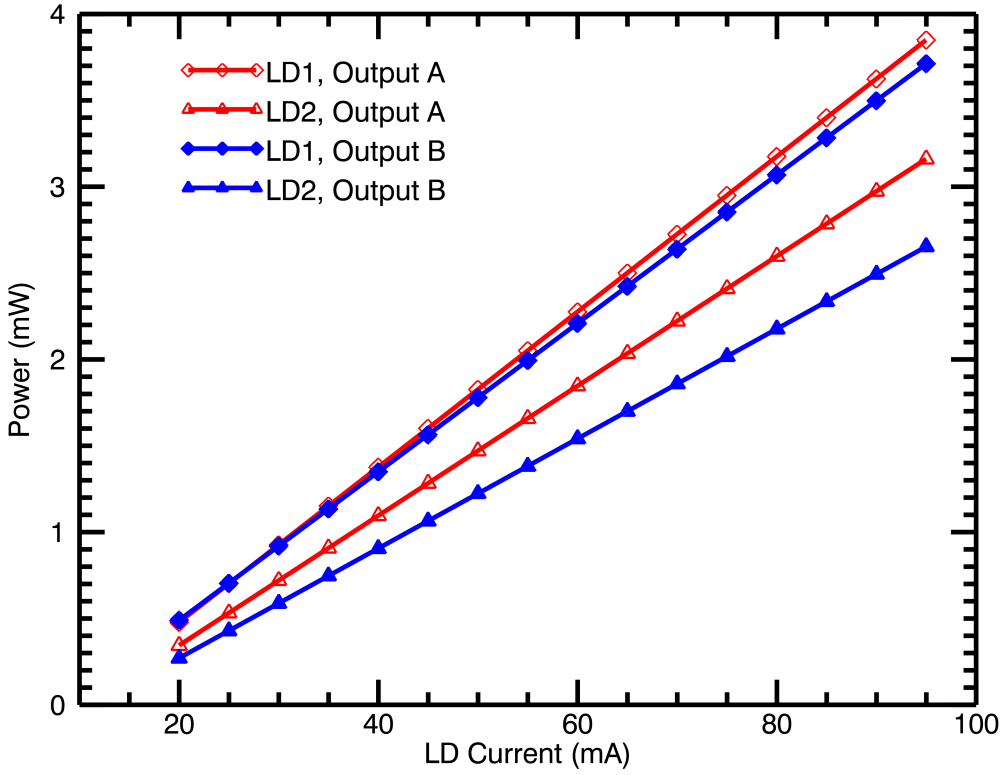

Figure 5.4: A comparison of the laser signals at the two outputs of the fibre coupler. One output is connected to the photomixer while the other is connected to the OSA. Error bars are insignificant.

It is clear that the PMF fiber coupler does not have a splitting ratio of 50:50 as stated in its data sheet. The observed differences in the powers from the two coupler outputs could be due to the fact that the fibre before and after the coupler is looped in circles of small diameters enough to introduce extra losses in the PMF fibre. It has been shown that reducing the loop radii of high birefringence fibre results in an increase in the polarization dependent loss [101]. A damaged fiber connector end can also give the same result. Table 5.1 helps in determining the power that goes to the photomixer based on the power measured by

Table 5.1: A comparison of the laser signals from the two ends of the fibre coupler. The first three columns shows the required total laser power and the contributions from the two laser diodes. The fourth and fifth columns show the drive currents that would yield the required laser powers. The last column shows the laser powers that would be measured from output B. The errors in the measured current were insignificant and that in the measured optical power was ± 0.003 mW

Output A					Output B		
Total Power (mW)	LD1 Power (mW)	LD2 Power (mW)	LD1 Current (mA)	LD2 Current (mA)	LD1 Power (mW)	LD2 Power (mW)	Total Power (mW)
1	0.5	0.5	21.03	24.92	0.243	0.183	0.426
2	1.0	1.0	32.95	39.10	0.473	0.398	0.871
3	1.5	1.5	44.86	53.28	0.704	0.613	1.317
4	2.0	2.0	56.78	67.47	0.934	0.828	1.762
5	2.5	2.5	68.70	81.65	1.164	1.043	2.207
6	3.0	3.0	80.62	95.83	1.395	1.258	2.652
7	3.5	3.5	92.54	110.02	1.625	1.473	3.098

the OSA. The laser power values recorded in this Chapter are those obtained by connecting output A to the OSA and output B to the photomixer. More optical power can be fed to the photomixer by interchanging the connections but great care must be taken not to exceed the power limits.

Figure 5.5 shows how the laser power varies with drive current. The maximum current was limited to slightly less than 100 mA as this was the maximum current limit of

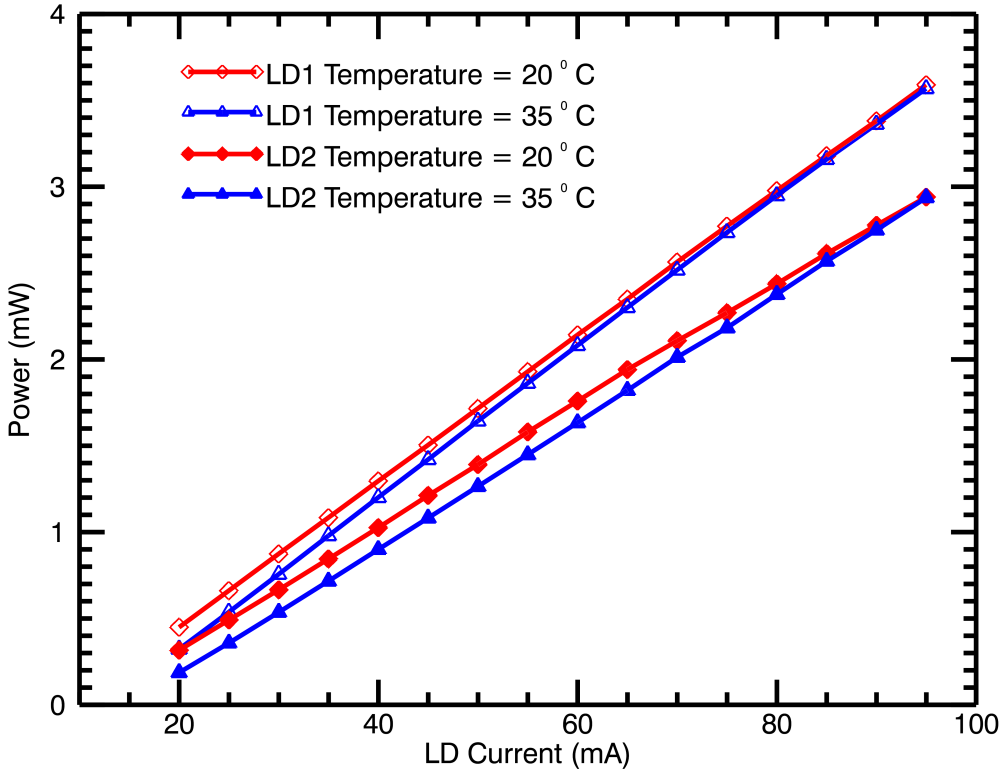

Figure 5.5: The variation of laser power with drive current when the LDs are operated at the minimum and maximum operating temperatures of 20 ^{0}C and 35 ^{0}C respectively. Error bars are insignificant.

the current modules used with the LDC. When operated at 20 ^{0}C, the slopes for the graphs are 0.04195 $\pm$ 0.00009 W/A and 0.03525 $\pm$ 0.00009 W/A for LD1 and LD2 respectively. When operated at 35 ^{0}C, the slopes were 0.04353 $\pm$ 0.00009 W/A and 0.03680 $\pm$ 0.00009 W/A respectively. Figure 5.6 shows how the frequency of the laser signals varies with drive current when the laser diodes are operated at their minimum (20 ^{0}C) and maximum (35 ^{0}C) operation temperatures. It can be seen that the frequency decreases slowly as the drive current is increased. These changes were considered second order effects and were not taken

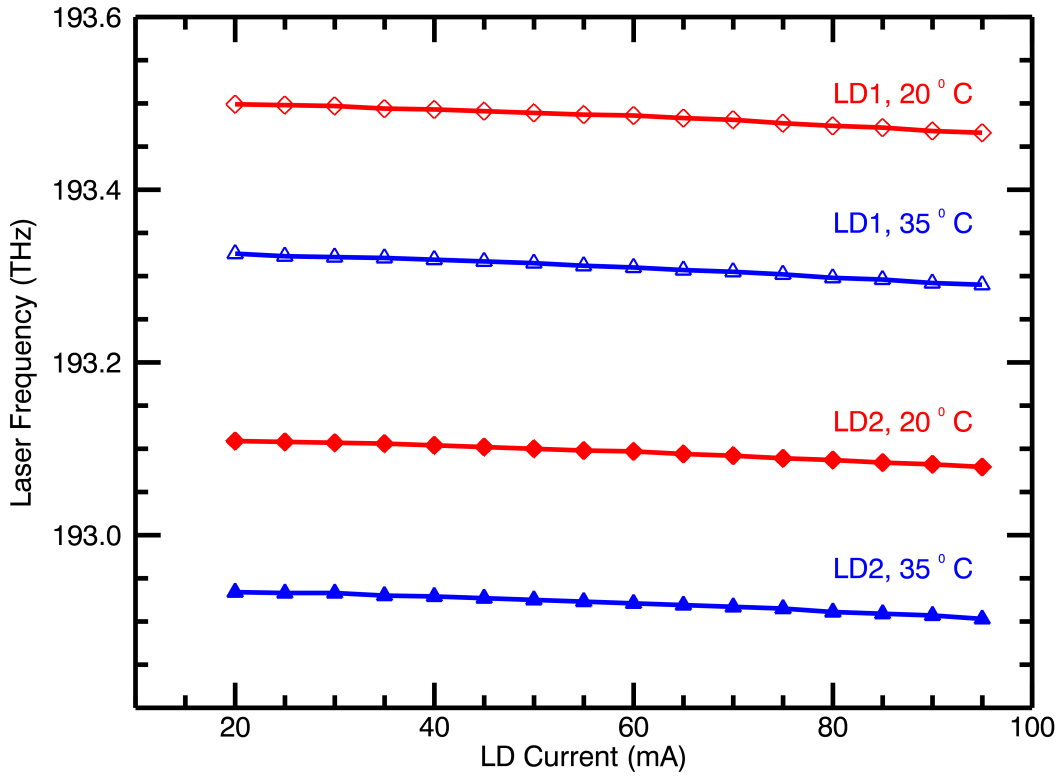

Figure 5.6: The variation of laser frequency with drive current. The LDs were operated at temperatures of 20 ^{0}C (red curves) and 35 ^{0}C (blue curves). Error bars are insignificant.

into account when automating the operation of the photomixer to simplify the LabVIEW programs.

5.3 The V-I characteristics of the photomixer

The DC voltage-current (V-I) curve of a THz photomixer is the best indicator of its quality. V-I characteristics of photodiodes have already been discussed in Section 2.2.2. Figure 5.7 shows the V-I characteristics of a reverse biased photomixer when illuminated

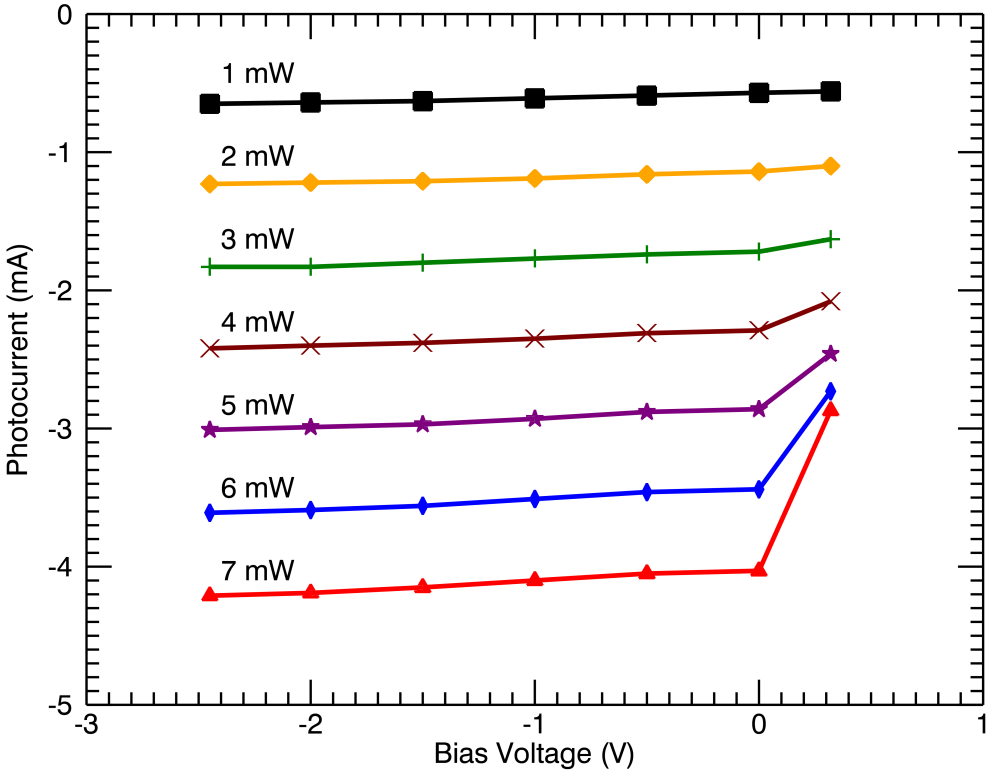

Figure 5.7: VI Characteristics of the MMT photomixer when illuminated with laser radiation with a difference frequency of 239 GHz. The V-I curves for incident optical power between 1 and 7 mW. The photomixer was operated between -2.5 V and 0.32 V.

with the combined laser powers from the two laser diodes as measured from output A of the fiber coupler. The bias voltage lower limit was V_l = -2.5 V and the upper limit was V_l + 0.32 V (refer to Figure 2.2). Following recommendation from the MMT group at RAL the bias voltage to the photomixer was turned on first before illuminating the photomixer to protect it from damage. The laser power was then increased gradually until the required power was reached. Detailed information on the operation of the photomixer is presented in Appendix B. As is expected, the photocurrent increases with incident optical power.

There is a linear relationship between photocurrent and bias voltage from 0 to -2.45 V. The differential resistance of the photomixer for this part of the V-I curves is approximately 30 kΩ. At around 0.5 V, there is a threshold where the current begins to increase rapidly resulting in a sharp drop of the differential resistance. In order to protect the device, the photocurrent was not allowed to exceed the upper limit of 1 mA which corresponds to a bias voltage of 1 V. For the same reason, the minimum current was set at -5 mA corresponding to a bias voltage of approximately -2.5 V. Figure 5.8 shows that the relationship between the photocurrent and optical power is linear for bias voltages between 0.00 V and -2.45 V. As is expected from the diode equation, the relationship deviates from linearity at positive bias voltages. Table 5.4 shows the different parameters used to obtain data for Figures 5.7 and 5.8.

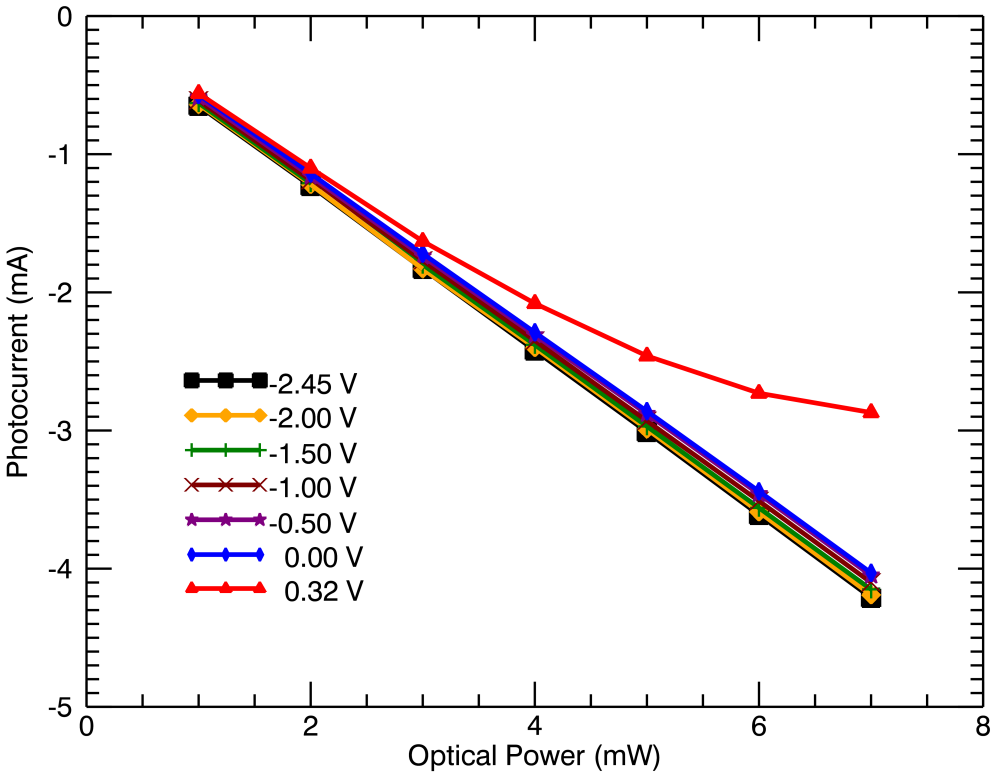

Figure 5.8: The variation of photocurrent with incident optical power. Positive bias shows a departure from linearity. This is to be expected since the diode is operating in the non-linear region.

Table 5.2: Combinations of LD temperatures and currents used to obtain Figures 5.7 and 5.8. In all cases the laser power from the two LDs was kept as close as possible. This is a requirement for maximum operation of the photomixer discussed in Section 2.6. The temperatures of both laser diodes was kept at 20 ^{0}C throughout the measurement process.

LD1 Temperature (^{0} C)	35.03	35.03	35.03	35.03	35.03	35.03	35.03	35.03
LD1 Current (mA)	18.75	24.79	30.99	37.10	43.08	49.13	55.18	61.37
LD1 Frequency (THz)	193.378	193.377	193.375	193.372	193.371	193.368	193.365	193.362
LD1 Power ($\pm$ 0.03 mW)	0.503	0.995	1.506	2.007	2.508	3.008	3.500	4.007
LD2 Temperature (^{0} C)	21.91	21.91	21.91	21.91	21.82	21.82	21.82	21.82
LD2 Current (mA)	18.65	26.19	33.49	40.76	48.14	55.55	63.29	70.99
LD2 Frequency (THz)	193.139	193.137	193.136	193.133	193.131	193.128	193.125	193.122
LD2 Power ($\pm$ 0.03 mW)	0.501	1.006	1.502	2.000	2.501	3.001	3.502	3.997
Total Laser Power (mW)	1.00	2.00	3.01	4.01	5.01	6.01	7.00	8.00
Difference Frequency (THz)	0.239	0.239	0.239	0.239	0.239	0.239	0.239	0.2392
Difference Frequency (cm^{-1})	7.98	7.98	7.98	7.98	7.98	7.98	7.98	7.98

5.4 FTS and detector Settings

As was described in Chapter 4, the frequency and power of the output THz radiation from the photomixer were measured using the University of Lethbridge FTS and a cryogenically cooled detector. An IDL program running on a GUI is used to control the FTS. Table 5.3 shows the settings used in the measurement of the output THz radiation from the photomixer. The speed of the FTS scanning mirror (see Figure 4.5) was set at

Table 5.3: FTS and detector settings used in the measurement of the output THz radiation from the photomixer.

Parameter	Value
Speed	3.0 cm s^{-1}
Number of Scans	5
Resolution	0.006 cm^{-1}
Nyquist	125 cm^{-1}
Detector Frequency Response	100 Hz
Filter band	450 μm

3.0 cm/s of the OPD. The detector frequency response was set at 1000 Hz. The value of the detector frequency response limits the maximum speed for a given Nyquist frequency. For most of the measurements that were done, the Nyquist frequency was set at 125 cm^{-1} and the resolution was at its maximum of 0.006 cm^{-1}. Whenever the signal was very low, measurements were repeated 5 times and a mean interferogram calculated. Throughout the measurement process, the detector response was checked to determine whether or not there

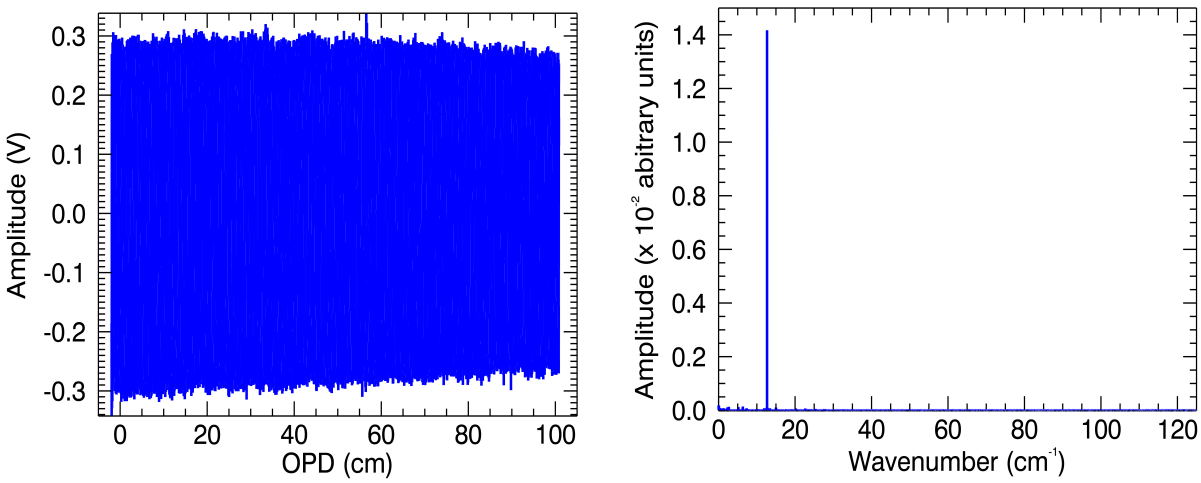

Figure 5.9: Example interferogram and its spectrum obtained with the above FTS settings, a bias voltage of -0.5 V and incident optical power on the photomixer of 5 mW. The difference frequency was 12.66 cm^{-1}.

was need to recycle the cryostat. Helium is required to cool the detector to about 300 mK at which point it becomes extremely sensitive. This makes the detectors sensitive to the low THz signal from the photomixer. The unavailability of a source of known power at THz frequencies meant that the power measurements could only be expressed as arbitrary values. An example interferogram and its spectrum obtained with these settings are shown in Figure 5.9

5.5 The dependence of THz power on reverse bias voltage and incident optical power

Figure 5.10 shows how the output THz power of the MMT photomixer generated with a difference frequency of 0.24 THz depends on the bias voltage. The parameters that were set to obtain these results are shown in Table 5.4. Example interferogram and

spectrum of the signal measured with the FTS when viewing the photomixer have been shown in Section 4.6. The THz power was obtained from the integrated line intensity. The spectrum obtained from a background scan was subtracted from all measured spectra before calculating the line area. It can be seen that the THz power is almost zero for positive bias voltages. It increases and peaks at a bias voltage of -0.5 V and then starts to decrease again. The hold time of the Helium-3 prevented us from taking finer measurements. All measurements had to be done before the detector started warming up. It is possible that we would have observed that the peak does not occur at a fixed bias voltage of -0.5 V.

Döhler [102] and colleagues observed that with increasing optical power the peak

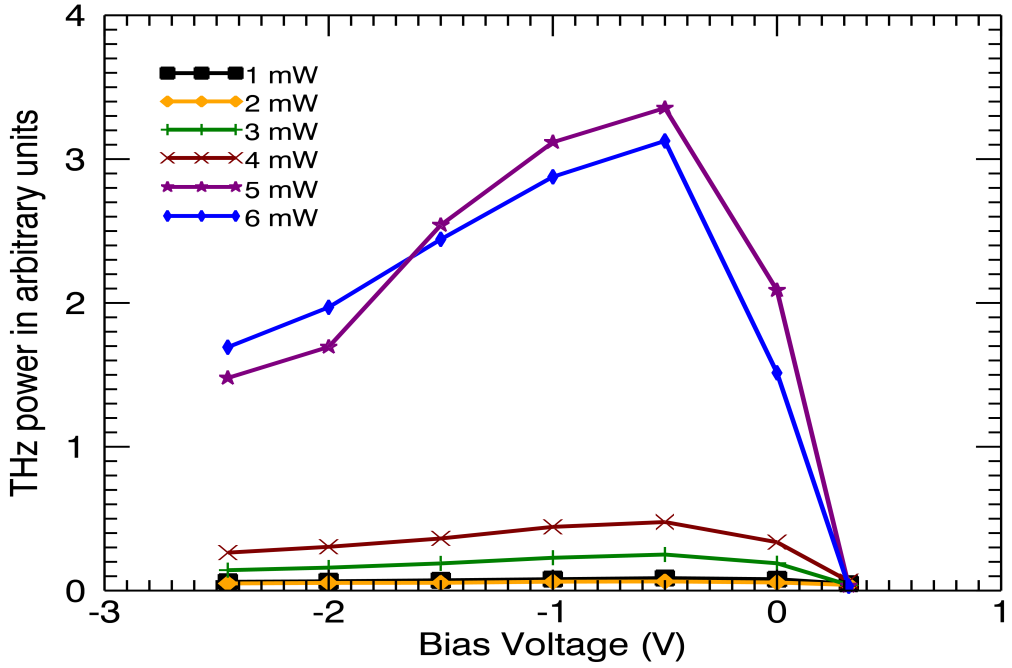

Figure 5.10: The variation of THz power from the photomixer with bias voltage for various incident total laser power. The difference frequency was 0.24 THz.

Table 5.4: Combinations of LD temperatures and currents used to obtain Fig 5.10. In all cases the laser power from the two LDs was kept as close as possible. This is a requirement for maximum operation of the photomixer discussed in Section 2.6. The temperatures of both laser diodes was kept at 20 ^{0}C throughout the measurement process. The difference frequency was 0.24 THz.

	Photocurrent (mA) for total incident power from 1 to 7 mW						
Laser Power, P_0 (mW)	1	2	3	4	5	6	7
Bias Voltage, V_B (V)							
-2.45	-0.65	-1.23	-1.83	-2.42	-3.01	-3.61	-4.21
-2.00	-0.64	-1.22	-1.83	-2.40	-2.99	-3.59	-4.19
-1.50	-0.63	-1.21	-1.80	-2.38	-2.97	-3.56	-4.15
-1.00	-0.61	-1.19	-1.77	-2.35	-2.93	-3.51	-4.10
-0.50	-0.59	-1.16	-1.74	-2.31	-2.88	-3.46	-4.05
0.00	-0.57	-1.14	-1.72	-2.29	-2.86	-3.44	-4.03
0.32	-0.56	-1.10	-1.63	-2.08	-2.46	-2.73	-2.87

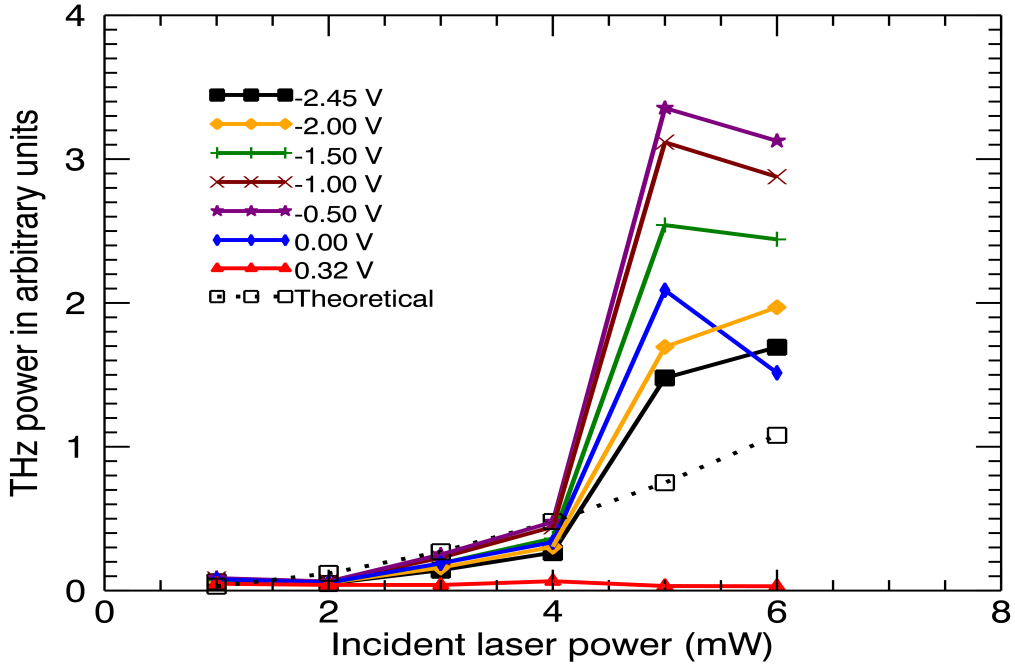

Figure 5.11: The variation of THz power from the photomixer with incident total laser power for various bias voltages. The difference frequency was 0.24 THz. A curve calculated from the theory presented in Chapter 2 is also shown.

of the THz power shifts towards increasing reverse bias. They attributed this to an increase of the screening of the built-in field in the photomixer. The reverse bias compensates for this reduction of the built-in field allowing for the establishment of the optimum field for ballistic transport. Ballistic transport is the transport of electrons in a medium with less scattering. High reverse bias voltages cause the fields to become too large for optimum ballistic transport resulting in a decrease of the THz power. Figure 5.11 shows the dependence of THz power on incident optical power. The measured data is shown in Table 5.5. Below 5 mW, the relation is observed to be quadratic as is expected from Equation (2.18). There is a sudden increase in THz power between optical powers of 4 and 5 mW. Above 5 mW, the THz power

drops for all bias voltages except for -2.0 V and -2.45 V. The drop in power is greater for zero bias voltage. A similar result was obtained by Döhler and colleagues [102]. Figure 5.8 shows that there is a linear relationship between incident optical power and photocurrent for all bias voltages considered in this thesis except for zero bias voltage. This may be the

Table 5.5: Combinations of LD temperatures and currents used to obtain Fig 5.11. In all cases the laser power from the two LDs was kept as close as possible. This is a requirement for maximum operation of the photomixer discussed in Section 2.6. The temperatures of both laser diodes was kept at 20 ^{0}C throughout the measurement process. The difference frequency was 0.24 THz. The error in the calculation of the integrated area was ± 0.0050.

	THz power (arbitrary units) for laser power from 1 to 7 mW						
Laser Power, P_0 (mW)	1	2	3	4	5	6	7
Bias Voltage, V_B (V)							
-2.45	0.0611	0.0496	0.1419	0.2639	1.4785	1.6926	0.4110
-2.00	0.0648	0.0535	0.1597	0.3044	1.6943	1.9699	0.4797
-1.50	0.0716	0.0540	0.1890	0.3623	2.5413	2.4420	0.5866
-1.00	0.0793	0.0619	0.2282	0.4431	3.1173	2.8769	0.7208
-0.50	0.0867	0.0636	0.2507	0.4767	3.3552	3.1267	0.7583
0.00	0.0792	0.0564	0.1899	0.3366	2.0884	1.5141	0.3316
0.32	0.0476	0.0394	0.0391	0.0654	0.0318	0.0302	0.0347

reason why for zero bias voltage, the drop in power is greater than for other bias voltages.

The above measurements were repeated for difference frequencies of 0.28 THz (Figures 5.12), 0.33 THz (Figures 5.13) and 0.38 THz (Figures 5.15). All results show that the optimum bias voltage for this particular MMT photomixer is -0.5 V but as discussed ear-

lier, finer measurements may show that the optimum value becomes more negative as the incident optical power increases.

Figure 5.12(b) shows that there is a quadratic relation between THz power and incident optical power for optical powers below 4 mW. Above 4 mW, the THz power seems to saturate for all bias voltages except for zero bias where there is a relatively large drop. This behavior has already been observed in the results for a difference frequency of 0.23 THz. Figure 5.13(b) shows a slightly different behavior for optical powers above 4 mW. In this case the THz power keeps increasing with optical power. The THz power is lower than that obtained for a difference frequency 0.28 THz and there are no signs of saturation. The fact that the peak THz power for each bias voltage, occurring at an optical power of 7 mW, is less than the power at which saturation occurs in Figure 5.15(b), could be the reason why there are no signs of saturation. Measurement results used to plot Figure 5.15 were obtained when the cryogenic cooler was about to run out of liquid Helium-3. The THz power had a sudden drop above an optical power of 3 mW. The detector started to warm-up and its responsivity dropped.

5.6 The dependence of THz power with difference frequency

The current research activities in THz photomixers is focused on increasing the output power. It has already been shown in Section 2 that the THz power decreases with frequency with a roll-off of 12 dB/octave. Four difference frequencies were investigated in this thesis. The output THz signals obtained with a bias voltage of 0.5 V and total incident optical power of 5 mW are shown in Figure 5.15. The results show that the THz power

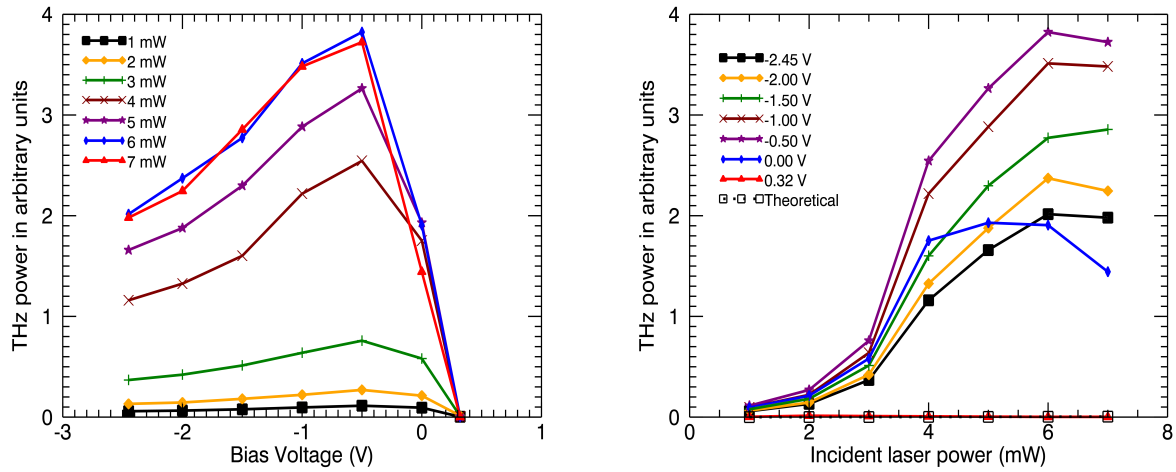

Figure 5.12: The variation of THz power from the photomixer with (a) bias voltage for various incident total laser powers, (b) incident total laser power for various bias voltages. The difference frequency was 0.28 THz.

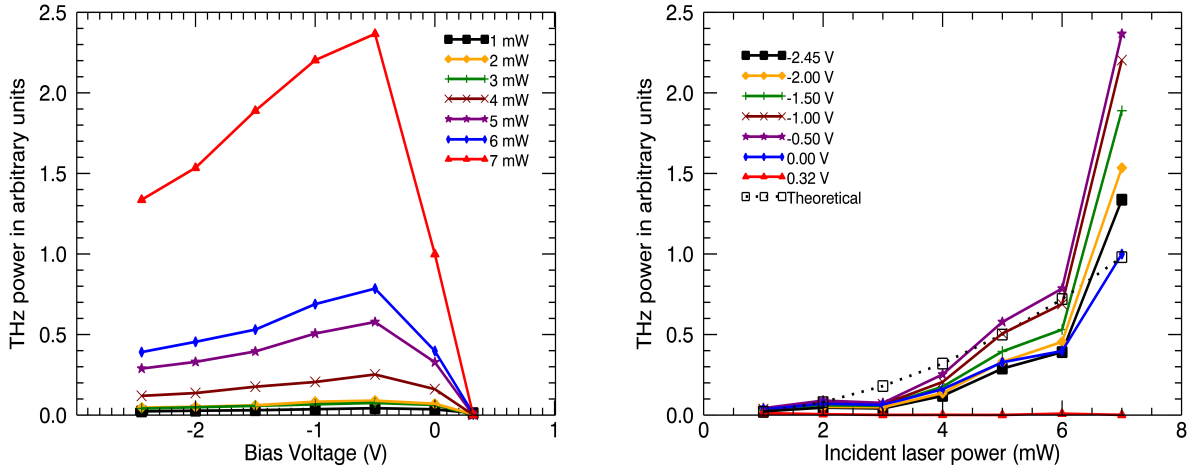

Figure 5.13: The variation of THz power from the photomixer with (a) bias voltage for various incident total laser powers, (b) incident total laser power for various bias voltages. The difference frequency was 0.33 THz.

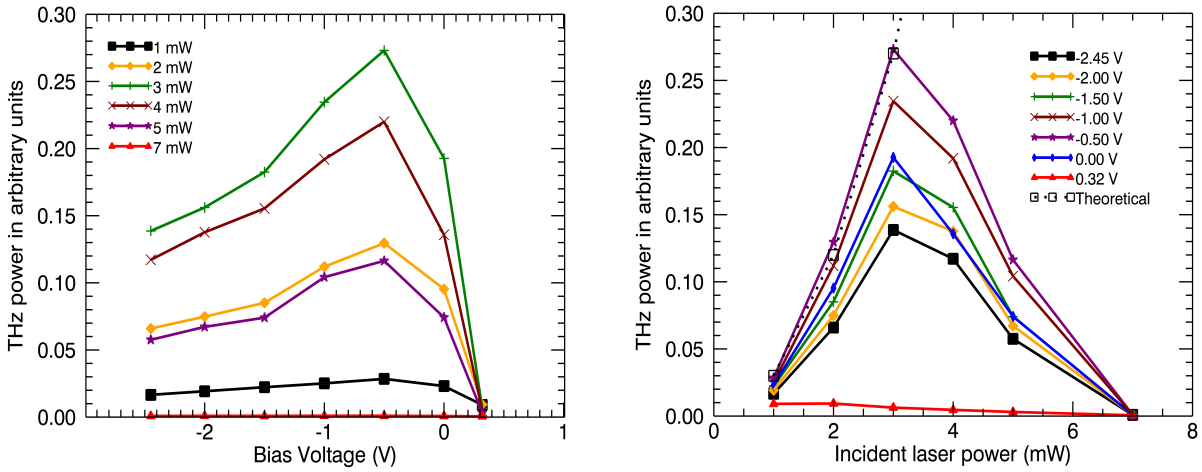

Figure 5.14: The variation of THz power from the photomixer with (a) bias voltage for various incident total laser powers, (b) incident total laser power for various bias voltages. The difference frequency was 0.38 THz.

obtained by integrating the area under each line decreases with frequency as expected.

This number was limited by the fact that we ran out of Helium-3. Currently our research group is investigating the possibility of using transition edge superconducting (TES) detectors which do not require the use of Helium-4. The hold time of Helium-3 precluded us from taking more measurements at different frequencies. Nonetheless, with the measurements that were obtained, we were able to show that we could control accurately the frequency of the THz source.

5.7 A comparison of measured and requested frequencies

Figure 5.16 shows a comparison between the measured and requested frequencies. The relationship is linear with a slope of 1.00075 and an intercept of 3.2×10^{-5}. This shows that the photomixer has been successfully automated.

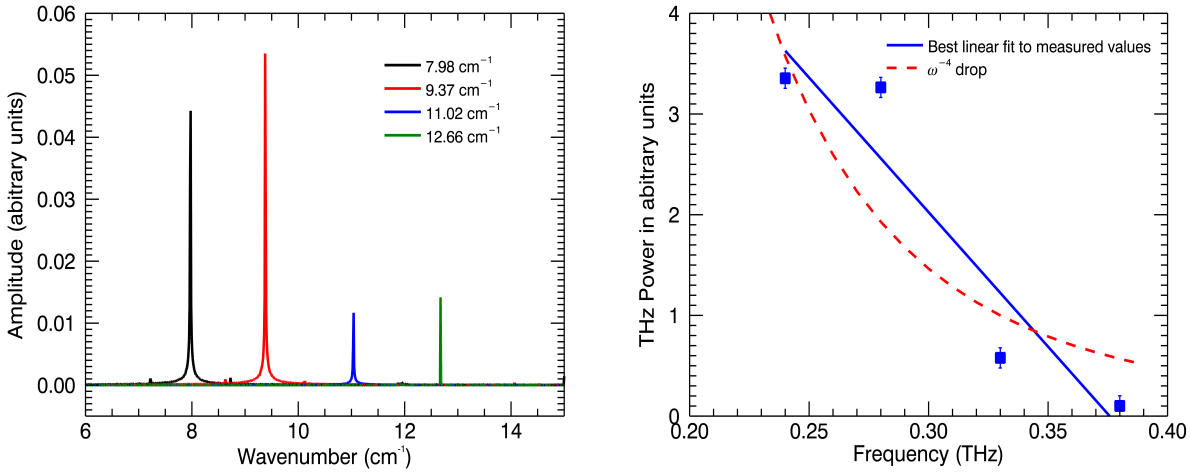

Figure 5.15: Measurements of four select THz signals at frequencies of 0.24 THz, 0.28 THz, 0.33 THz and 0.38 THz. The signals were obtained by tuning the reverse bias voltage and incident optical power to -0.5 V and 5 mW respectively; (a) The measured spectra and (b) the variation of the integrated area with frequency. The photomixer THz power decreases with frequency as is expected. The error bars are too small to be observed.

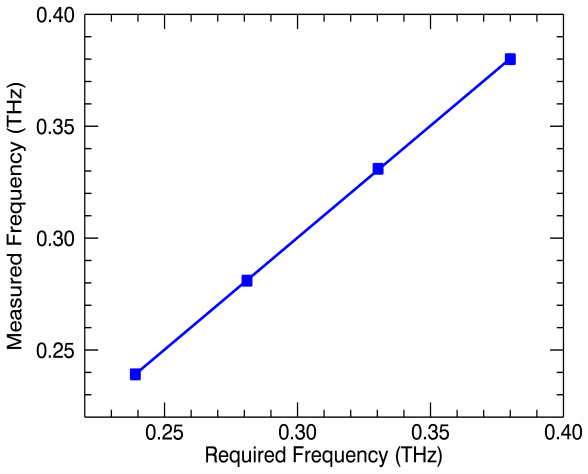

Figure 5.16: Relationship between measured and requested frequencies

5.8 Conclusions

In this Chapter, it was shown that the laser diodes and the photomixer were characterized to the level that we could for the time that we were able to cool the cryostat. The time to take measurements was limited by the cryogenic hold time. All the results presented in this chapter were obtained using LabVIEW programs that I developed. These programs allow us to predict reliably and generate THz radiation at any frequency between 0.25 THz and 0.65 THz. Slight residual differences between the measured and requested frequencies can be attributed to second-order effects discussed in section 5.2. However, the main goal of the thesis, to automate a tunable THz photomixer source has been achieved.

Chapter 6

Conclusions and Future Work

6.1 Summary

In this thesis I have discussed the exploratory and general investigation of the utility of photomixers as tunable THz sources. This work was motivated by the fact that operating a photomixer that our group had bought from the MMT group at the RAL was tedious and time consuming. Various parameters which include the bias voltage, the laser diode temperatures and currents had to be carefully tuned for optimum performance. The photomixer itself is both expensive and extremely sensitive. The bias voltage and the incident optical power must not exceed certain limits otherwise the device is damaged permanently. I set out on a journey to automate the control of the photomixer, which I accomplished successfully.

The project was tackled by first characterizing the laser diodes to obtain relationships between the laser diode temperatures and drive currents with the laser frequency and powers. The linear relationships obtained were then used in writing LabVIEW programs

to automatically control these parameters. It was observed that there is some non-linear behavior that result in the measured values being slightly different to the requested values. These non-linearities were not considered when writting the LabVIEW programs since their effect was considered small for our purposes. Nonetheless, in future, these nonlinearities need to be investigated. The VI characteristics for the photomixer was also studied separately with and without incident optical power. I now understand what parameters need to be set to obtain a desired difference frequency. It has been shown that we can reliably predict the THz frequency using the LabVIEW programs that I developed.

In this thesis I have shown that in general the photomixer characteristics follow the theory as described in Chapter 2. The trends shown in different figures for the difference frequencies studied indicate optimum values for reverse bias voltage and incident optical power. That was not the main driver for this thesis, but it is clear that the method described here will be able to give more accurate data. I also observed some deviations from theory that need further investigation. From Figure 5.3 we observed that for a constant drive current, the laser power is not constant with temperature and from Figure 5.6, the laser frequency is also not constant with drive current for a fixed laser diode temperature.

In order to calculate the actual output THz power, one needs to know the throughput of the feedhorns that radiates the THz power to free space. The throughput takes into account the receiving area and the solid angle of the incident beam. Such an analysis is out of the scope of this thesis and so all THz power measurements are arbitrary. A calibration source with a similar feedhorn will help calibrate the photomixer THz power.

Measurements of THz power at the μW level require a cryogenic detector. Our

group is now using a pulse-tube cooler which does not require the expensive liquid helium. Its is clear that there are second order effects that have to be investigated further. This was beyond the scope of the thesis.

Without the automation of the process, and taking into account the hold time of the cryostat, it is clear that this level of analysis would not have been possible. To put this into perspective, it takes about 10 minutes to set all parameters manually and take a single measurement. It takes about half a minute to set all parameters and take a measurement using the software programs that I developed. This is after taking into account the time required to allow the laser diodes to stabilize after setting each and every parameter.

In the process of carrying out the experiments described in this thesis, I gained experience in labVIEW programming and in operating laser diodes, spectrum analyzers, the FTS and cryogenic detectors. The goal we set up to achieve was to develop a tunable source of THz radiation which I accomplished.

6.2 Future Work

Even though the general photomixer characteristics do follow theory, there are some deviations that require further investigation. These include the fact that the THz power output from the photomixer tends to saturate with bias voltage and optical power and that the relationship between laser power and laser diode temperature is nonlinear. Also, the laser frequency varies nonlinearly with laser diode current. If the AIG group were to get into designing and building its own photomixers at the University of Alberta Micro and Nanofabrication facility we now have the methodologies. Future work will include

using the suite of LabVIEW programs that I developed to analyze other photomixers, either commercial ones or the ones that will be developed by the AIG. It has been shown elsewhere that cooling the photomixer helps in increasing its heat capability. It maybe worthwhile to consider redesigning our cryostats so that they can house both the photomixer and detector.

Appendix A

Usage of the photomixer

A.1 Necessary precautions for photomixer use

The photomixer is extremely fragile and can be destroyed by electrostatic discharge (ESD), incorrect or excessive bias, excessive optical power and mechanical shock. The following precautions should be observed at all times: otherwise irreversible damage or destruction of the photomixer is likely to occur. This information can also be obtained from the manual that came with the photomixer [86].

1. Observe strict ESD handling procedures when using the device: grounded wrist straps must be worn. The SSMA bias connector should be connected to a short circuit or a 50 Ω termination when the device is not in use. When connecting a shorting cap or a cable from a bias supply, ensure that the bias voltage is set to zero. Then momentarily short out the inner pin of the male connector onto the outer part of the photomixer's Sub-SMA. A small version of the SMA connector, about 70 % size (SSMA) connector.

This will discharge any accumulation of charge in the cable capacitance.

2. Only use low noise bias supply with this photomixer. Do not apply optical power without first applying a reverse bias.

3. Take care when connecting and disconnecting the fibre optic. the PM fiber facet needs to be kept scrupulously clean and all facets must be inspected before connection. The PM fiber facet cleaning should be done with care. Care must be taken to ensure that the patchcords used to connect to the output of the coupler have the right type of connectors. Connecting APC connectors to flat polished connectors (FC) will damage fibre ends and cause a reduction of the transmitted power. Bending the pigtails and patchcords to small angles should also be avoided as it also increases losses at these fibre bends.

4. Observe correct polarity when connecting the bias supply: the center SSMA connector is to be biased negative for normal operation. For clarity, a reverse (forward) bias of 1.0 V means that - 1.0 V (+1.0 v) is applied to the center contact of the SSMA connector.

5. Do not exceed a maximum reverse bias of 2.5 V.

6. The maximum safe input power is 12 mW corresponding to a maximum safe photocurrent of 6.0 mA.

7. Do not exceed a forward current of 3 mA. This will be reached at a forward bias well below 1.0 V

8. Do not exert any mechanical load to, or bend with a radius below 25 mm, the optical fiber and fiber/block interface.

9. Do not apply any mechanical shock to the block

10. Do not clamp the block, or otherwise apply force when tightening screws. Any distortion of the metal will adversely affect the fiber/photodiode alignment, resulting in reduced output power.

A.2 Connection Information

1. Turn on the mains power to all equipment. The OSA requires about 30 minutes to warm up before accurate measurements can be obtained.

2. Ensure that the optical source is delivering no power to the photomixer.

3. Ensure that the bias supply is set to zero and that the bias output is grounded. The batteries in the bias box must be fully charged before connecting to the photomixer.

4. Whilst wearing a grounding wrist strap, connect the coaxial bias cable to the source: leave the bias output grounded. Then connect the photomixer to the other end of the cable as described above.

5. Inspect the fibre facets with a suitable microscope and clean if necessary.

6. Connect the fibre ferrule to the optical source ferrule.

7. Disconnect the bias output from ground and apply a bias between +0.5 and 2.0 V. The photomixer is extremely sensitive to sudden changes in bias voltage or current. In order to avoid these glitches, which usually happen when switching the device on or off, the bias box has a toggle switch that must be in "shorted" position. After

power-up, the toggle switch can then be opened to allow current to flow through the photomixer. This is required for both manual and remote operation.

8. Slowly increase the source power whilst observing the photocurrent.

9. To turn off, gradually reduce the optical power to zero.

10. Then reduce the bias to zero and ground the bias supply output.

11. Turn off the optical source.

12. Disconnect the optical fibre and apply protective cap.

13. Whilst wearing a wrist strap, disconnect the bias cable from the photomixer and connect the SSMA shorting cap.

Appendix B

Experimental settings used to obtain Figure 2.2

Table B.1: The experimental settings used to obtain the VI characteristics of the MMT photomixer.

LD1 Temperature	LD2 Temperature	LD1 Power	LD2 Power	Total Optical Power
20.99	24.99	0.506	0.496	1.00
26.23	30.84	0.751	0.754	1.51
31.48	37.99	1.002	1.027	2.03
36.18	45.79	1.253	1.254	2.51
42.19	54.49	1.503	1.497	3.00
48.48	58.29	1.746	1.753	3.50
53.98	65.49	1.992	2.030	4.02
59.68	72.48	2.248	2.256	4.50
65.58	77.89	2.503	2.495	4.50
71.67	84.49	2.757	2.750	5.51
78.67	89.99	3.058	3.018	6.08
82.77	95.98	3.263	3.246	6.51

Bibliography

[1] D. Saeedkia and S. Safavi-Naeini. Terahertz Photonics: Optoelectronic Techniques for Generation and Detection of Terahertz Waves. *Journal of Lightwave Technology*, 26(15):2409–2423, 2008.

[2] E. J. Nichols and J. D. Tear. Joining the infrared and electric wave spectra. *Astrophysics Journal*, 61:17–37, 1925.

[3] P. H. Siegel. Terahertz Technology. *IEEE Transactions on Microwave Theory and Techniques*, 50(3):910–928, March 2002.

[4] E. R. Brown. A photoconductive model for superior GaAs THz photomixers. *Applied Physics Letters*, 75(6):769–771, August 1999.

[5] D. Saeedkia and S. Safavi-Naeini. Modeling and Analysis of a Multilayer Dielectric Slab Waveguide With Applications in Edge-Coupled Terahertz Photomixer Sources. *Journal Of Lightwave Technology*, 25(1):432–439, 2007.

[6] C. Baker, I. S. Gregory, W. R. Tribe, M. J. Evans, M. Missous and E. H. Linfield. Continuous-Wave Terahertz Photomixing in Low-Temperature InGaAs. In *IEEE,*

Joint 29th International Conference on Infrared and Millimeter Waves and 12th International Conference on Terahertz Electronics, pages 367–368, October 2004.

[7] S. Verghese, K. A. McIntosh and E. R. Brown. Highly Tunable Fiber-Coupled Photomixers with Coherent Terahertz Output Power. *IEEE Transactions on Microwave Theory and Techniques*, 45(8):1301–1309, August 1997.

[8] Laboratory of Terahertz Spectroscopy, Prague, Czech Republic. `http://department.fzu.cz/lts/`.

[9] E. Herbst and E. F. van Dishoeck. Complex Organic Interstellar Molecules. *Annual Review of Astronomy and Astrophysics*, 47:427–480, 2009.

[10] T. Otsuji, T. Suemitsu and Y. M. Meziani. Exploring novel millimeter-wave and Teraherts integrated electron devices and their applications to future systems. `http://www.otsuji.riec.tohoku.ac.jp/old/Research/2006_OtsujiLabo_latest.pdf`.

[11] M. V. Kartikeyan, E. Borie and M. k. A. Thumm. *Gyrotrons: High power microwave and millimeter wave technology.* Springer-Verlag Berlin Heidelberg, 2004.

[12] G. Dammertz, S. Albert, A. Arnold, E. Borie, V. Erckmann, G. Gantenbein, E. Giguet, R. Heidinger *et al.*. Development of a 140-GHz 1-MW continuous wave gyrotron for the W7-X stellarator. *IEEE Transactions on Plasma Science*, 30(3):808–818, 2002.

[13] F. J. Duarte. *Tunable Lasers Handbook.* Academic Press Limited, 1995.

[14] University of California Center for Terahertz Science and Technology. `http://sbfel3.ucsb.edu/ctst/Top.html/`.

[15] Yun-Shik Lee. *Principles of Terahertz Science and technology.* Springer Science+Business Media, LLC, 2009.

[16] L. F. Costa, R. C. Viscovini, J. C. Moraes, F. C. Cruz and D. Pereira. Terahertz Laser Generation by Optically Pumped Polar Molecules. In *Optical Terahertz Science and Technology, OSA Technical Digest Series (CD), paper MD3*, 2007.

[17] L. F. L. Costa, J. C. S. Moraes, F. C. Cruz, F. C. Cruz, R. C. Viscovini and D Pereira. CH_3OH optically pumped by a $^{13}CO_2$ laser: new laser lines and assignments. *Applied Physics B: Lasers and Optics*, 86(4):703–706, 2007.

[18] A. Bertolini, G. Carelli, N. Ioli, C. A. Massa, A. Moretti and F. Strumia. Optically pumped CW FIR laser: New submillimeter laser emissions from CH_2DOH, CH_3I, CD_3I, and trioxymethylene. *International Journal of Infrared and Millimeter Waves*, 18(6):1281–1284, 1997.

[19] M. Inguscio and G. Moruzzi. A review of frequency measurements of optically pumped lasers from 0.1 to 8 THz. *Journal of Applied Physics*, 60(12):R161–R192, December 1986.

[20] N. Orihashi, S. Suzuki and M. Asada. One THz harmonic oscillation of resonant tunneling diodes. *Applied Physics Letters*, 87:233501–3, 2005.

[21] E. Brown, J. Söderström, C. Parker, L. Mahoney, K. Molvar, T. McGill. Oscillations up to 712 GHz in InAs/AlSb resonant-tunneling diodes. *Applied Physics Letters*, 58:2291–2293, 1991.

[22] H. Eisele. InP Gunn devices for 400-425 GHz. *IEEE Electronics Letters*, 42(6):358–359, 2006.

[23] H. Eisele. 355 GHz Oscillator with GaAs TUNNETT diode. *IEEE Electronics Letters*, 41(6):329–331, 2005.

[24] L. Samoska, A. Peralta, M. Hu, M. Micovic and A. Schmitz. A 20 mW, 150 GHz InP HEMT MMIC power amplifier module. *IEEE Microwave and Wireless Components Letters*, 14(2):56–58, 2004.

[25] A. V. Raesanen. Frequency multipliers for millimeter and submillimeter wavelengths. In *Proceedings of the IEEE*, volume 80, pages 1842–1852, 1992.

[26] Virginia Diodes, Inc. Charlottesville, USA. `http://vadiodes.com`.

[27] V. Krozer, B. Leone, H. G. Roskos, T. Loffler, G. Loata,G. H. Dohler, F. Renner, S. Eckardt, S. Malzer, A. Schwanhausser, T. O. Klaassen, A. Adam, P. Lugli, A. Di Carlo, M. Manenti, G. Scamarcio, M. S. Vitiello and M. Feiginov. Optical far-IR wave generation-state-of-the-art and advanced device structures. In *Proceedings of SPIE: Microwave and Terahertz Photonics, Strsbourg, France*, volume 5466, pages 178–192, 2004.

[28] L. Mahler, R. Kohler, A. Tredicucci, F Beltram, H. E. Beere, E. H. Linfield, D. A. Ritchie and A. G. Davies. Single-mode operation of terahertz quantum cascade lasers with distributed feedback resonators. *Applied Physics Letters*, 84(26):5446–5448, 2004.

[29] P. Mukherjee and B. Gupta. Terahertz (THz) Frequency Sources and Antennas -

A Brief Review. *International Journal of Infrared and Miliimetre Waves, Springer*, 29(12):1091–1102, September 2008.

[30] A. Tredicucci, R. Kohler, L. Mahler, H. E. Beere, E. H. Linfield and D. A. Ritchie. Terahertz quantum cascade lasers-first demonstration and novel concepts. *Semiconductor Science and Technology*, 20(7):S222–S227, 2005.

[31] B. S. Williams, S. Kumar and Q. Hu. Operation of terahertz quantum-cascade lasers at 164 K in pulsed mode and at 117 K in continuous-wave mode. *Optics Express*, 13(9):3331–3339, 2005.

[32] C. Worrall, J. Alton, M. Houghton, S. Barbieri, H. E. Beere, D. Ritchie and C. Sirtori. Continuous wave operation of a superlattice quantum cacade laser emitting at 2 THz. *Opticsl Express*, 14(1):171–181, 2005.

[33] O. A. Klimenko, Y. A. Mityagin, S. A. Savanov, V. N. Murzin, N. V. Dyakonova, P. Solignac and W. Knap. Terahertz wide range tunable cyclotron resonance p-Ge laser. *Journal of Physics: Conference Series*, 193:1–5, 2009.

[34] K. Kawase, J. Shikata and H. Ito. Terahertz wave parametric source. *Journal of Physics D: Applied Physics*, 34:R1–R14, 2001.

[35] R. Sowade, I. Breung, I. C. Mayorga, J. Kiessling, C. Tulea, V. Dierolf and K. Buse. Continuous-wave optical parametric terahertz source. *Optics Express*, 17(25):171–181, 2009.

[36] Y. J. Ding. High-Power Tunable Terahertz Sources Based on Parametric Processes and

Applications. *IEEE Journal of Selected Topics in Quantum Electronics*, 13(3):705–720, 2007.

[37] E. R. Brown, F. W. Smith and K. A. McIntosh. Coherent millimeter-wave generation by heterodyne conversion in low-temperature-grown GaAs photoconductors. *Journal of Applied physics*, 73(3):1480–1484, February 1993.

[38] E. R. Brown, D. C. Driscoll and A. C. Gossard. State-of-the-art in 1.55 μm ultra-fast InGaAs photoconductors, and the use of signal-processing techniques to extract the photocarrier lifetime. *Semiconductor Science and Technology*, 20(7):S199–S204, August 2005.

[39] L. P. Schmdt, S. Biber, G. Rehm and K. Huber. THz measurement technologies and applications . In *IEEE International Conference on Microwaves, Radar and Wireless Communications*, volume 95, pages 581–587, 2002.

[40] H. Ito, T. Furuta, F. Nakajima, K. Yoshino and T. Ishibashi. Photonic Generation of Continuous THz Wave Using Uni-Traveling-Carrier Photodiode. *Journal Of Lightwave Technology*, 23(12):4016–4021, December 2005.

[41] T. Taniuchi and H. Nakanishi . Collinear phase-matched terahertz-wave generation in GaP crystal using a dual-wavelength optical parametric oscillator. *Journal of Applied Physics*, 95(12):7588–7591, 2004.

[42] S. Verghese, E. K. Duerr, K. A. McIntosh, S. M. Duffy, S. D. Calawa, C. Y. E. Tong, R. Kimberk and R. Blundell. A Photomixer Local Oscillator for a 630-GHz Heterodyne Receiver. *IEEE Microwave And Guided Wave Letters*, 9(6):245–247, June 1999.

[43] S. Matsuura and H. Ito. Generation of CW Terahertz Radiation with Photomixing. *Terahertz Optoelectronics, Topics in Applied Physics, Springer Berlin*, 97:157–204, January 2005.

[44] A. Kapov, J. Blondel, M. Voss and K. H. Gundlack. A three photon noise SIS heterodyne receiver at submillimeter wavelength. *IEEE Transactions on Applied Superconductivity*, 9(2):4456–4459, 1999.

[45] B. S. Karasik, M. C. Gaidis, W. R. McGrath, B. Bumble and H. G. LeDuc. A low-noise 2.5 THz superconductive Nb hot-electron mixer. *IEEE Transactions on Applied Superconductivity*, 7(2):3580–3583, 1997.

[46] B. G. Streetman and S. K. Banerjee. *Solid State Electronic Devices*. PHI Learning Private Limited, 6 edition, 2006.

[47] E. R. Brown, K. A. McIntosh, F. W. Smith, M. J. Manfra and C. L. Dennis. Measurements of optical-heterodyne conversion in low-temperature-grown GaAs. *Applied Physics Letters*, 62(11):1206–1208, March 1993.

[48] E. R. Brown, K. A. McIntosh, F. W. Smith, K. B. Nichols, M. J. Manfra, C. L. Dennis and J. P. Mailia. Millliwatt output levels and superquadratic bias dependence in a low-temperature-grown GaAs photomixer. *Applied Physics Letters*, 64(24):3311–3313, June 1994.

[49] E. R. Brown, K. A. McIntosh, K. B. Nichols and C. L. Dennis. Photomixing up to 3.8 THz in low-temperature-grown GaAs. *Applied Physics Letters*, 66(3):285–287, January 1995.

[50] S. Verghese, K. A. McIntosh and E. R. Brown. Optical and terahertz power limits in the low-temperature-grown GaAs Photomixers. *Applied Physics Letters*, 71(19):2743–2745, November 1997.

[51] S. Matsuura, M. Tani and K. Sakai. Generation of coherent terahertz radiation by photomixing in dipole photoconductive antennas. *Applied Physics Letters*, 70(5):559–561, February 1997.

[52] E. Peytavit, G. Mouret, J. F. Lampin, S. Arscott, P. Masselin, L. Desplanque, O. Vanbésien, R. Bocquet, F. Mollot and D. Lippens. Terahertz electromagnetic generation via optical frequency difference. In *Proceedings, IEE Optoelectronics*, volume 149, pages 82–87, 2002.

[53] Shun L. Chuang. *Physics of optoelectronic devices.* Wiley-Interscience publication, 1995.

[54] A. Stöhr, R. Heinzelmann, C. Kaczmarek and D. Jäger. Ultra-broadband Ka to W-band 1.55 μm travelling-wave photomixer. *IEEE Electronics Letters*, 36(11), 2000.

[55] A. Stöhr, R. Heinzelmann, A. Malcoci and D. Jäger. Optical heterodyne millimeter-wave generation using 1.55 μm traveling-wave photodetectors. *IEEE Transactions on Microwave Theory and Techniques*, 49(10):1926–1933, October 2001.

[56] A. Stöhr, R. Heinzelmann, R. Güsten, F. Schäfer, H. Stüer, F. Siebe, P. van der Wal, V. Krozer, M. Feiginov and D. Jäger. Integrated 460 GHz photonic transmitter module. *IEEE Electronics Letters*, 37(22):1347–1348, October 2001.

[57] T. Ishibashi, N. Shimizu, S. Kodama, H. Ito and T. Furuta. Uni-Traveling-Carrier Photodiodes. In *OSA, The Topical Meeting on Ultrafast Electronics and Optoelectronics*, volume 13, pages 83–87, March 1997.

[58] E. R. Brown. THz generation by photomixing in ultrafast photoconductors. *International Jornal of High Speed Electronics and Systems*, 13(2):497–545, August 2003.

[59] Sheng S. Li. *Semiconductor Physical Electronics.* Springer Science+Business Media, LLC, 2006.

[60] E. R. Brown, S. Verghese and K. A. McIntosh. Terahertz Photomixing in Low-Temperature-Grown GaAs. In *Proceedings of SPIE: Advanced Technology MMW, Radio, and Terahertz Telescopes, Kona, HI, USA*, volume 3357, pages 132–142, March 1998.

[61] C. Kadow, S. B. Fleischer, J. P. Ibbetson, J. E. Bowers, A. C. Gossard, J. W. Dong and C. J. Palmstrom. Self-assembled ErAs islands in GaAs: Growth and subpicosecond carrier dynamics. *Applied Physics Letters*, 75(22):3348–3350, 1999.

[62] C. Kadow, A. W. Jackson, A. C. Gossard, S. Matsuura and G. A. Blake. Self-assembled ErAs islands in GaAs for optical-heterodyne THz generation. *Applied Physics Letters*, 76(24):3510–3512, 2000.

[63] I. C. Mayorga, M. Mikulics, A Schmitz, P. van der Wal, R. Güsten, M. Marso, P. Kordos and H. Lüth. An optimization of terahertz local oscillators based on LT-GaAs technology. In *Proceeding of SPIE*, volume 5498, pages 537–547, 2004.

[64] A. Malcoci, R. E. Miles, J. Vukusic, J. Stake, B. M. Pascual, P. G. Huggard and D. N. Matheson. Design and fabrication of waveguide-coupled CW-photomixers for millimeter wave and THz applications using low temperature grown GaAs photoconductors. In *IEEE Joint 30th International Conference on Infrared and Millimeter Waves and 13th International Conference on Terahertz Electronics, IRMMW-THz*, volume 1, pages 130–131, September 2005.

[65] N. S. Daghestani, G. S. Sokolovskii, N. E. Bazieva, A. V. Tolmatchev and E. U. Rafailov. Efficient THz radiation from a nanocrystalline silicon-based multi-layer photomixer. *Semiconductor Science and Technology*, 24(9):095025(1–5), 2009.

[66] I. S. Gregory, C. Baker, W. R. Tribe, I. V. Bradley, M. J. Evans, E. H. Linfield, A. G. Davies and M. Missous. Optimization of Photomixers and Antennas for Continuous-Wave Terahertz Emission. *IEEE Journal of Quantum Electronics*, 41(5):717–728, 2005.

[67] H. Ito, T. Nagatsuma, A. Hirata, T. Minotani, A. Sasaki, Y. Hirota and T. Ishibashi. High-power photonic millimetre wave generation at 100GHz using matching-circuit-integrated uni-travelling-carrier photodiodes. In *IEE Proc.-Optoelectronics*, volume 150, pages 138–142, April 2003.

[68] Y. Lan, B. Zeng, H. Zhang, B. Chen and Z. Yang. Simulation of carbon nanotube THz antenna arrays. *International Journal of Infrared and Millimeter Waves*, 27(6):871–877, 2007.

[69] G. W. Hanson. Fundamental transmitting properties of carbon nanotube antennas. *IEEE Transactions on Antennas and Propagation*, 53(11):3426–3435, 2005.

[70] C. Fumeaux, G. D. Boreman, W. Herrmann, F. K. Kneubühl and H. Rothuizen. Spatial impulse response of lithographic infrared antennas. *Applied Optics*, 38(1):37–46, 1999.

[71] German Institut für Technische Physik I, Universität Erlangen-Nürnberg. `http://majestix.physik.uni-erlangen.de/`.

[72] M. Tonouchi, H. Saijo, M. Hangyo, O. Morikawa. P. Gu, M. Tani and K. Sakai. Highly efficient terahertz radiation from $YBa_2Cu_3O_{7-\delta}$ thin film log-periodic antennas. *Physica C: Superconductivity*, 357-360, Part 2:1600–1602, 2001.

[73] K. A. McIntosh, E. R. Brown, K. B. Nichols, O. B. McMahon, W. F. DiNatale and T. M. Lyszczarz. Terahertz photomixing with diode lasers in low-temperature-grown GaAs. *Applied Physics Letters*, 67(26):3844–3846, 1995.

[74] S. M. Duffy, S. Verghese, K. A. McIntosh, Andrew Jackson, A. C. Gossard and S. Matsuura. Accurate Modeling of Dual Dipole and Slot Elements Used with Photomixers for Coherent Terahertz Output Power. *IEEE Transactions On Microwave Theory And Techniques*, 49(6):1032–1038, 2001.

[75] K. Han, Y. Park, S. Kim, H. Han Park and H. Lim. A Terahertz Yagi-Uda Antenna for High Input Impedance. *IEEE, 33rd International Conference on Infrared, Millimeter and Terahertz Waves (IRMMW-THz), Pasadena, CA*, pages 1–2, September 2008.

[76] J. T. Darrow, X. C. Zhang and D. H. Auston. Power scaling of large-aperture photoconducting antennas. *Applied Physics Letters*, 58(1):25–27, 1991.

[77] A. Stöhr, A. Malcoci and D. Jäger. THz Photomixing Travelling-Wave Photodetectors.

In *IEEE International Microwave Symposium Digest, MTT−S*, volume 1, pages 275–278, June 2004.

[78] K. S. Giboney, R. L. Nagarajan, T. E. Reynolds, S T. Allen, R. P. Mirin, M. J. W. Rodwell and J. E. Bowers. Travelling-Wave Photodetectors with 172-GHz Bandwidth and 76-GHz Bandwidth-Efficiency Product. *IEEE Photonics Technology Letters*, 7(4):412–414, 1995.

[79] K. S. Giboney, M. J. W. Rodwell and J. E. Bowers. Traveling-wave photodetector theory. *IEEE Transactions on Microwave Theory and Technology*, 45(8):1310–1319, August 1997.

[80] A. Hirata, T. Nagatsuma, R. Yano, H. Ito, T. Furuta, Y. Hirota, T. Ishibashi, H. Matsuo, A. Ueda, T. Noguchi, Y. Sekimoto, M. Ishiguro and S. Matsuura. Output power measurement of photonic millimeter-wave and sub-millimeter-wave emitter at 100-800 GHz. *IEEE Electronics Letters*, 38(15):798–799, 2002.

[81] T. Ishibashi, T. Furuta, H. Fushimi, S. Kodama, H. Ito, T. Nagatsuma, N. Shimizu and Y. Miramoto. InP/InGaAs Uni-Traveling-Carrier Photodiodes. *IEICE Transactions in Electronics*, E83-C(6):938–949, June 2000.

[82] H. Ito, F. Nakajima, T. Furuta and T. Ishibashi. Continuous THz-wave generation using antenna-integrated uni-travelling-carrier photodiodes. *Semiconductor Science Technology*, 20(7):S191–S198, 2005.

[83] P. G. Huggard, L. Azcona, A. Laisne, B. N. Ellison, P. Shen, N. J. Gomes P. A. Davies. Integrated 1.55 μm photomixer local oscillators for heterodyne receivers at

mm-wavelengths. In *Microwave and Terahertz Photonics, Proceedings of SPIE*, volume 5466, pages 193–201, 2004.

[84] J. Payne, B. Shillue and A. Vaccari. Photonic techniques for use on the atacama large millimeter array. In *Proceedings of the International Topical Meeting on Microwave Photonics MWP, Melbourne, Australia*, pages 105–108, November 1999.

[85] J. M. Payne and W. P. Shillue. Photonic Techniques for Local Oscillator Generation and Distribution in Millimeter-Wave Radio Astronomy. Technical Report 440, ALMA MEMO, October 2002.

[86] Millimeter Wave Technology Group. *1.55 μm photomixer for University of Lethbridge: Handling Instructions.* STFC Rutherford Appleton Laboratory, UK, 2008.

[87] u^{2}t Photonics AG, Reuchlinstrasse 10/11, 10553 Berlin, German. `http://www.u2t.de/en/products/by-product/photodetectors/`.

[88] P. G. Huggard, L. Azcona, A. Laisné, B. N. Ellison, P. Shen, N. J. Gomes and P. A. Davies. Integrated 1.55 μm photomixer local oscillator sources for heterodyne receivers from 70 GHz to beyond 250 GHz. In *Millimeter and Submillimeter Detectors for Astronomy II, Proceedings of SPIE*, volume 5498, pages 596–604, 2004.

[89] O. Morikawa, M. Tonouchi, M. Tani, K. Sakai and M. Hangyo. Sub-THz emission properties of photoconductive antennas excited with multimode laser diode. *Japanese Journal of Physics, Part 1*, 38(3A):1388–1389, March 1999.

[90] M. Tani, P. Gu, M. Hyodo, K. Sakai and T. Hidaka. Generation of coherent terahertz

radiation by photomixing of dual-mode lasers. *Invited paper: Optical and Quantum Electronics, Kluwer Academic Publishers, Netherlands*, 32(4-5):503–520, 2000.

[91] K. Shibuya, M. Tani and M. Hangyo. Enhancement of THz Photomixing Efficiency by Using a Pulse-Modulated Multimode Laser Diode. In *IEEE Joint 32nd International Conference on Infrared and Millimeter Waves and the 15th International Conference on Terahertz Electronics, IRMMW-THz, Cardiff*, pages 732–733, 2007.

[92] M. Tani, O. Morikawa, S. Matsuura and M. Hangyo. Generation of terahertz radiation by photomixing with dual- and multiple-mode lasers. *Semiconductor Science and Technology*, 20(7):S151–S163, 2005.

[93] M. Mikulics, M. Marso, S. Stancek, E. A. Michael and P. Kordos. Terahertz-Radiation Photomixers on Nitrogen-Implanted GaAs. In *IEEE International Conference on Advanced Semiconductor Devices and Microsystems, ASDAM '06*, pages 117–120, October 2006.

[94] S. Preu, F. H. Renner, S. Malzer, G. H. Döhler, L. J. Wang, M. Hanson, A. C. Gossard, T. L. J. Wilkinson and E. R. Brown. Efficient terahertz emission from ballistic transport enhanced n-i-p-n-i-p superlattice photomixers. *Applied Physics Letters*, 90(21):2121151–3, 2007.

[95] Aerotech, Inc. Pittsburgh, PA, USA. `http://www.aerotech.com/products/controllers/Soloist/index.cfm`.

[96] David A. Naylor, Brad G. Gom, Ian S. Schofield, Greg J. Tompkins, and Gary R. Davis. Mach-Zehnder Fourier transform spectrometer for astronomical spectroscopy

at submillimeter wavelengths. In *Proceeding of SPIE*, volume 4855, page 540–551, 2003.

[97] The European Space Agency. SPIRE Observers' Manual. HERSCHEL-DOC-0798 version 2.0, The European Space Agency, May 2010.

[98] Brad Gom. A Cryogenic Detector for Submillimetre Astronomy. Master's thesis, University of Lethbridge, 1997.

[99] Locke Spencer. Imaging Fourier Transform Spectroscopy from a Space Based Platform - The Herschel/SPIRE Fourier Transform Spectrometre. Master's thesis, University of Lethbridge, 2009.

[100] S. P. Davis, M. C. Abrams and J. W. Brault. *Fourier Transform Spectrometry.* Academic Press, 1st edition, 2001.

[101] A. Bessa dos Santos and J. P. von der Weid. PDL effects in PMD emulators made out with HiBi fibers: Building PMD/PDL emulators. *IEEE Photonics Technology Letters*, 16(2):452–454, 2004.

[102] G.H. Döhler, F. Renner, O. Klar, M. Eckardt, A. SchwanhäuBer, S. Malzer, D. Driscoll, M. Hanson, A.C. Gossard, G. Loata, T. Löffler and H. Roskos. THz-photomixer based on quasi-ballistic transport. *Semiconductor Science and Technology*, 20(7):S178–S190, 2005.